

# **REFLECTANCE SPECTRA IN SYNTHETIC MINERAL MIXTURES: AN IMPLICATION FOR THE FEASIBILITY OF REMOTE DETECTION OF RARE EARTH ELEMENTS IN HEMATITE RICH CARBONATITES**

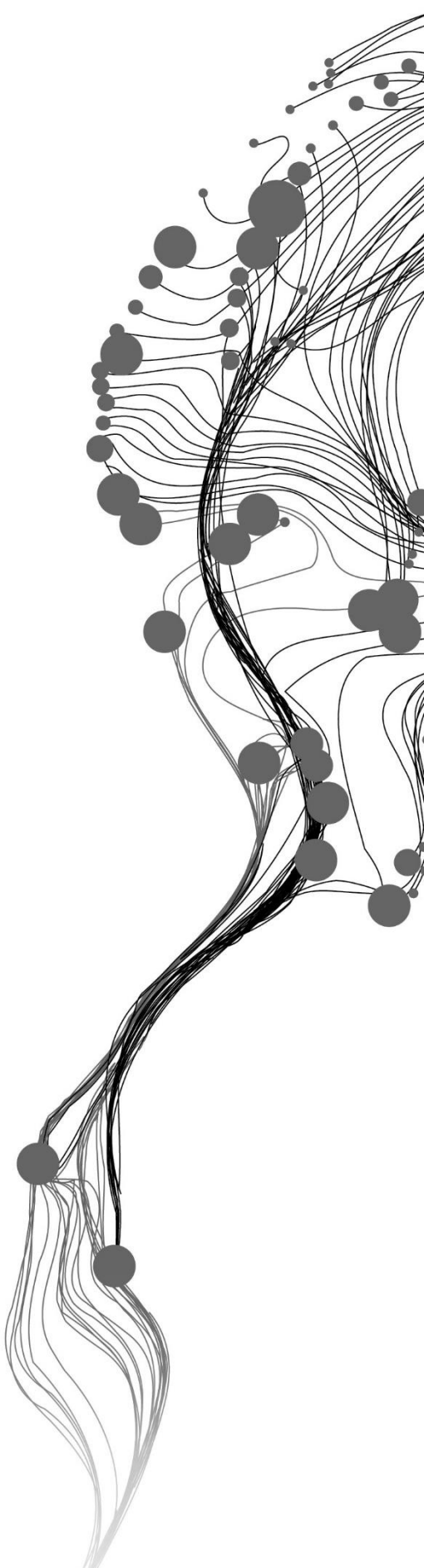
W.M.S.K. WEERANAYAKE

July 2024

SUPERVISORS:

Dr. H.M.A. van der Werff

Dr. A.H. Dijkstra



# REFLECTANCE SPECTRA IN SYNTHETIC MINERAL MIXTURES: AN IMPLICATION FOR THE FEASIBILITY OF REMOTE DETECTION OF RARE EARTH ELEMENTS IN HEMATITE RICH CARBONATITES

W.M.S.K. WEERANAYAKE

Enschede, The Netherlands, July 2024

Thesis submitted to the Faculty of Geo-Information Science and Earth Observation of the University of Twente in partial fulfilment of the requirements for the degree of Master of Science in Geo-information Science and Earth Observation.

Specialization: Applied Remote Sensing for Earth Sciences

## SUPERVISORS:

Dr. H.M.A. van der Werff

Dr. A.H. Dijkstra

## THESIS ASSESSMENT BOARD:

Dr. Juan Carlos Afonso (Chair)

Dr. David J. Turner (External Examiner)

#### DISCLAIMER

This document describes work undertaken as part of a programme of study at the Faculty of Geo-Information Science and Earth Observation of the University of Twente. All views and opinions expressed therein remain the sole responsibility of the author and do not necessarily represent those of the Faculty.



## ABSTRACT

Reflectance spectroscopy and remote sensing have become significant for identifying REE-minerals and analysing REEs in various mineral phases and geological settings. Carbonatites are one of the primary geological environments with the potential to contain rare earth element (REE) minerals such as monazite, bastnäsite, and parisite. Detecting REEs in carbonatite with proximal sensing and remote sensing is challenging due to the presence of iron oxide and iron-bearing minerals, as they mask spectral absorption features of REE ions in the Visible and Near Infrared region (VNIR). This study attempts to understand the influence of varying concentrations of hematite and carbonates on absorption feature parameters of the REEs-bearing minerals using laboratory-synthesised powdered mineral mixtures. Additionally, this study explores the possibility of using REE ion absorption features in VNIR and short-wave infrared (SWIR) regions to detect REEs in carbonatites using various operational airborne and spaceborne sensors. Laboratory-synthesised monazite and bastnäsite from a precipitation method were used as REE minerals. Powdered mineral mixtures with different mineral abundances were prepared in the laboratory, followed by an acquisition of reflectance spectra using an ASD Fieldspec 3 spectroradiometer. The AVIRIS and EnMap, representative of hyperspectral sensors, and Landsat Next and WorldView3, representative of multispectral sensors, were considered for resampling laboratory spectra to evaluate remote sensing capabilities. In this study, a linear relationship of depth of the REE-related absorption features with monazite abundance is found in the SWIR region in synthetic mineral mixtures, and these features are not masked by the presence of hematite. So, while most spectroscopic studies so far have focussed on the application of REE-related absorption features in the VNIR region, the current study highlights that REE-related absorption features in the SWIR range are particularly well suited for detecting monazite in mineral mixtures resembling natural REE ores. These findings are formalized in a novel Praseodymium band ratio (PrR) for mapping absorption features in the SWIR region caused by electronic transitions in the  $\text{Pr}^{3+}$  ion. Our analysis shows that this ratio effectively detects REE even in hematite-bearing carbonatites using hyperspectral data from laboratory spectrometers, but probably also from airborne or spaceborne hyperspectral sensors. Moreover, the findings of this study also reveal the capability of a multispectral satellite for detecting REEs in nature-like REE ore rocks: the SWIR 2 band of the WorldView 3 multispectral sensor detecting the Pr feature centred at 1580 nm. In contrast, even though the new Landsat Next platform has several bands in the SWIR range, this study indicates that the band centred at 1610 nm is too wide (90 nm, FWHM) to detect the Pr feature. Any future multispectral sensors with a bandwidth smaller than 20 nm and with bands centring around 1570 nm with adjacent bands around 1700 nm would have the capability of detecting REEs, so these results should perhaps be considered in future sensor designs.

**Keywords:** *carbonatites, synthetic monazite, hematite, remote sensing, WorldView 3, Landsat Next, resampling, mineral mixtures*

## ACKNOWLEDGEMENTS

Few! I don't know how to even start to thank all the people who have stood by me and supported me!

I would like to thank my mother, Lakshmi Bandaranayake, my father, Gamini Weeranayake, and my dearest little brother, Kavinda Weeranayake. Without you, I would not be where I am today. Thank you so much for bearing with me for all these 30 years and all the love, support, courage, and blessings you have given me. I don't have words to express my gratitude and love for you.

A special thanks to my cousin Anuradha Wijethunga (Chooty Aiya) and my aunt from Canada, Sujani Wijesundara, for being there for me when I needed help the most. I would not be here in the Netherlands without you! Not only them but my dearest friends, who are just like family, Shehan Nanayakkara (Jila Aiya), Nelini Jayatilake (Hichchi Akka) from Australia, Chamod (Bamuna Aiya) from the USA, Ayodhya (Benzin Akka) from Australia, for your support, without which I would not be standing in the Netherlands pursuing a master's degree. I love you guys! I would like to thank my aunt Kumudu (Chuuti Amma), uncle Shantha (Bappa), Nihal (Bappi), and all my relatives who have always wished me the best and believed in me.

I would like to express my sincere gratitude to my supervisors, Dr. Harald van der Werff and Dr. Arjan Dijkstra. Thank you so much for all the knowledge and guidance you have shared with me. I would not be here without your guidance and understanding. It was an incredible experience. I cannot express how lucky I am to have had you as my supervisors. It was one of the best things that happened to me!

I would like to thank the chair of my thesis assessment board, Dr. Juan Afonso, for all the feedback and comments. Special thanks to the procedural advisor of my research, Bruno Portela, for all the guidance and encouragement you have given me throughout the year. I would like to thank the staff in the ITC and AES department: Dr. Chris Hecker, Dr Mark van der Meijde, Wim Bakker, Dr. Frank Ruitenbeek, Dr. Islam Fadel, Jonathan Franco Hempenius. These two years have been wonderful, with all the experiences and knowledge I gained from you! Also, I would like to thank Katherine Zweers-Peter and Camilla Marcatelli for their guidance and belief in me and for letting me play with all the chemicals and instruments in the ITC Geoscience lab. I would like to thank Jorike Siemerink and Theresa van den Boogaard-Burke from Student Affairs for being such kind human beings during all the ups and downs in my ITC life. Thank you so much!

I would like to thank all my friends in the Netherlands: Mahasen, Chakshu, Alma, Nasir, Amy (Varavarai), Shanan, Serhat, Salsa, Faheed, Wibisana, Aparna, Snighdha, and many more. You are my family in the Netherlands. Thanks for all the good times we had together.

I would like to thank all my friends from school, university and my workplace NBRO in Sri Lanka: Isuri (Batti), Nishika (Goldmari), Maheshi, Samudrika, Kanchana akka and Dulanjali (Panchi) for being there for me. Also, I would like to thank Willem and Hermie Slot for taking care of me and checking on me when I felt like I needed my family. Thank you for all the love!

Last but not least, I want to thank everyone, whether mentioned here or not, for being with me and believing in me. Thank you!

“උගත මනා ශිල්පයමයි මතු රැකෙනා”

“*Knowledge is the key*”

## TABLE OF CONTENTS

Abstract.....	i
Acknowledgements .....	ii
List of figures .....	v
List of tables .....	viii
List of abbreviations.....	ix
List of appendices.....	x
1. INTRODUCTION.....	11
1.1. Rare Earth minerals importance and geology .....	11
1.2. Review of reflectance spectroscopy of REEs bearing minerals.....	11
1.3. Research gap.....	13
1.4. Objectives and research questions .....	13
1.4.1. Main objective .....	13
1.4.2. Sub objectives.....	13
2. METHODOLOGY.....	15
2.1. Phase one – Mineral synthesis.....	15
2.1.1. Monazite synthesis.....	16
2.1.2. Bastnäs site synthesis.....	17
2.1.3. Calcite and Hematite .....	18
2.1.4. XRD analyses.....	18
2.2. Phase two - Data acquisition.....	18
2.2.1. Sample preparation.....	18
2.2.2. Mineral mixtures .....	19
2.2.3. Spectral measurements.....	20
2.3. Phase three- Spectral data analyses.....	21
2.3.1. Spectral analysis of pure minerals.....	21
2.3.2. Mineral mixture spectral data analysis .....	22
2.3.3. Resampling laboratory spectra to hyperspectral and multispectral sensors .....	24
3. RESULTS .....	26
3.1. Mineral synthesis .....	26
3.2. Spectral data analysis of synthesised minerals .....	27
3.2.1. Comparison of synthesised minerals with published spectral libraries .....	27

3.2.2. Comparison of synthetic bastnäsite and monazite.....	28
3.3. Sub objective one- Understanding the behaviour of spectra of the mineral mixtures. ....	30
3.3.1. Simple mixtures.....	31
3.3.2. Complex mixtures.....	33
3.4. Sub objective two – Detecting REEs with hyperspectral sensors.....	37
3.5. Sub objective three – Detecting REEs with multispectral sensors .....	38
4. DISCUSSION .....	41
4.1. Mineral synthesis .....	41
4.2. Mineral mixture preparation and ASD measurements .....	41
4.3. Spectral data analyses.....	42
4.4. The spectra of synthetic monazite and bastnäsite .....	42
4.4.1. Origin of Pr <sup>3+</sup> feature .....	44
4.5. Sub objective one - Understanding the behaviour of spectra of the mineral mixtures .....	45
4.5.1. Understanding of reflectance spectra of simple mineral mixtures .....	45
4.5.2. Understanding the reflectance spectra of complex mixtures.....	45
4.5.3. Pr <sup>3+</sup> as a promising feature for detecting REEs in hematite mixed spectra. ....	46
4.6. Sub objective two: Resampling spectra for hyperspectral sensors .....	47
4.7. Sub objective three: Resampling spectra for multi-spectral sensors .....	47
4.8. Limitations of the study .....	48
5. CONCLUSIONS .....	50
5.1. Recommendations.....	51
List of Refereces .....	52
Appendix .....	56



## LIST OF FIGURES

### Chapter 2

- Figure 2.1:* Graph showing the standard deviation of six spectral measurements taken to find the optimal mineral mixing method for obtaining a homogenous mixture; blue: petri dish mix, orange: agate mix, green: tube mix, b) the same graph with stacked reflectance values for better visualisation, note the higher standard deviation of six measurements in petri dish mixing compared to the agate and tube mix..... 19
- Figure 2.2:* Ternary diagram showing the composition of each mineral mixture by weight percentages..... 20
- Figure 2.3:* Illustration of the set-up used for reflectance spectroscopy measurements on mixed-mineral powders in the laboratory dark room..... 21
- Figure 2.4:* A sketch showing the parabolic interpolation method to extract local minima from continuum removed absorption feature by fitting a parabola through three consecutive measurement points. (After Van Ruitenbeek et al., 2014)..... 23
- Figure 2.5:* The wavelength ranges considered for the diagnostic Praseodymium Ratio(PrR) put forward in this thesis; MHC-10-5-85 is the reflectance spectra of 10 wt% monazite, 5 wt% hematite and 85 wt% calcite powdered mineral mixture, note that mean reflectance value of the wavelength ranges between 1759:1787 and 1759:1787 taken as numerator 1555:1580 and 1456:1470 as denominator centring the Pr absorption feature. Note the absence of absorption features of hematite and calcite spectra for considered wavelength range..... 24

### Chapter 3

- Figure 3.1:* Diffraction patterns of the synthesised materials with comparison to stick diagrams of crystallographic reference data monazite (mnz-syn), synthesised rhabdophane(rhabdo-syn), natural monazite from ITC collection (mnz-ITC). Note the similarity of the peak positions of the synthetic monazite to those in the natural monazite but also the different relative peak intensities and the low-intensities of the peaks at 2 theta angles greater than 40° for the natural monazite. Diffraction pattern of synthetic bastnäsite with reference data. Note the peak positions are overlapping with reference data. .... 26
- Figure 3.2:* Comparison of reflectance spectra of the synthesised minerals with the spectra of natural minerals from published spectral libraries, USGS: published spectra from Kokaly et al. (2017) (USGS v7 spectral library, GCS: published spectral library from Percival et al. (2019) (The National Mineral Reference Collection (NMC) Digital Spectral (VIS-NIR-SWIR) Library, Part II: REE-Nb-U-Th-bearing minerals by Geological Survey of Canada) ITC: spectra of brown coloured natural monazite powder from ITC mineral collection; a) Comparison of monazite spectra, SM: off white coloured synthetic monazite; b) comparison of bastnäsite spectra, SB: synthetic bastnäsite-off white colour; Note that for both synthetic minerals albedos difference and the gradual drop of visible region in natural minerals and absence of well-defined multiplets in Nd absorption features of synthetic bastnäsite in near-infrared region. .... 28
- Figure 3.3:* Comparison of synthetic monazite and bastnäsite with each other. Dashed lines mark the centres of some prominent absorption features observed in synthetic monazite. a) reflectance spectra comparison of VNIR range. b) reflectance spectra comparison in SWIR region; note the absence of crystal field splitting effect of major Nd and Pr features in bastnäsite compared to monazite and some Nd<sup>3+</sup>, Sm<sup>3+</sup> corresponding absorptions in the synthetic monazite occur at ~5-10 nm shorter wavelengths..... 30
- Figure 3.4:* Reflectance spectra for monazite or bastnäsite with calcite and hematite, normalised to a maximum reflectance value of 1 with shaded area indicating the standard deviation of the replicates

measurements for each sample, in blue: Reflectance spectra of bastnäsite mineral mixtures, in grey: Reflectance spectra of monazite mineral mixtures. ....31

*Figure 3.5:* The behaviour of reflectance spectra of simple mineral mixtures, dashed lines corresponds to the wavelength positions of prominent REE absorption features, notation MH-50-50 represents 50 wt% of monazite 50 wt% hematite in the mineral mixture, M-monazite, B- bastnäsite C- calcite, H-hematite. Note the gradual change of depths in VNIR and SWIR for calcite-REE mineral mixtures and in SWIR hematite-REE mineral mixture a) calcite-monazite mixture in VNIR. b) calcite-monazite mixture in SWIR. c) hematite-monazite mixture in VNIR. d)hematite-monazite mixture in SWIR. e) bastnäsite-calcite simple mixtures in VNIR. f) bastnäsite-calcite simple mixtures in VNIR g) bastnäsite-hematite simple mixtures in VNIR, h) bastnäsite-hematite simple mixtures in SWIR. i) calcite-hematite mixtures in VNIR. j) calcite-hematite mixtures in SWIR.....33

*Figure 3.6:* comparison of the spectra of 10 wt% monazite complex mixture with its end members highlighting the REE features still preserved in the spectra, notation MHC-10-1-89 represents 10 wt% of monazite 1 wt% hematite 89 wt% of calcite indicating the modal abundance of the mineral mixture, M-monazite, C- calcite, H-hematite, SM-synthetic monazite; note the REE ion absorption features in VNIR are either diluted or disappeared while Sm, Pr features are still preserved in the spectra of complex mixtures, dashed lines mark the centre of the absorption features .....33

*Figure 3.7:* Comparison of monazite and bastnäsite complex mixtures, in grey: bastnäsite complex mixtures, in black: monazite complex mixtures, notation: MHC-10-1-89 representing 10 wt% monazites,1 wt% hematite and 89 wt% calcite, M-monazite, C- calcite, H-hematite, B-bastnäsite; note that with the similar weight percentages preserved REE absorption features are sharper in monazite mixtures than that of bastnäsite, dashed lines mark the centre of the absorption features.....34

*Figure 3.8:* Figures showing REE features in VNIR range; notation: MHC-10-1-89 representing 10 wt% monazite,1 wt% hematite and 89 wt% calcite, M-monazite, C- calcite, H-hematite; left: continuum removed spectra between 760-840 nm highlighting Nd<sup>3+</sup> feature depths in complex mixtures; right: continuum removed spectra between 730-760 nm highlighting Nd<sup>3+</sup> feature depths in complex mixtures, note that the depth changes are below 0.1% of reflectance values and the significant depth change and smoothing of features after 4% hematite .....35

*Figure 3.9:* Scatterplots showing the changes of absorption parameters centred between 700-1200 nm; a) feature position change with increasing hematite, dark blue-10 wt% monazite complex mixtures, grey-complex mixtures containing 10 wt% monazite, blue – complex mixtures containing 5 wt% monazite, note that the changes do not show a relationship with hematite. b) feature depth changes in mixtures, black: hematite-monazite-calcite complex mixtures with 15% monazite, dark grey: hematite-monazite-calcite complex mixtures with 10% monazite, light: hematite-monazite-calcite complex mixtures with 5% monazite, blue: monazite calcite simple mixtures, red: hematite calcite simple mixtures, yellow: hematite monazite simple mixtures, note that with high changes of hematite the feature depth does not change while hematite percentage below 15 depth is changing with increasing hematite. c) figure showing the wavelength position change in 10 wt% monazite complex mixtures.....36

*Figure 3.10:* a) Scatter plot showing the relationship of the Pr feature depth and hematite percentage in monazite 5 wt%, 10wt% 15wt% complex mixtures. Note that hematite calcite mixtures do not have a feature in considered wavelength position. b)Scatterplots showing the relationship of the newly defined PrR with hematite abundance in complex and simple mixtures. c) Scatter plot showing the relationship of the Pr feature depth and monazite percentage in hematite 5 wt%, 10wt% 15wt% complex mixtures. d) Scatter plot

showing the relationship of the PrR with increasing monazite percentage in different mixtures. e) Scatter plot showing the relationship of the Pr feature depth and calcite percentage in monazite 5 wt%, 10wt% 15wt% complex mixtures. f) Scatter plot showing the variation of the PrR with increasing calcite percentage in different mixtures. Labeling: 5%M-H-C- represent 5 wt% monazite mixture with varying calcite and hematite abundances, M-monazite, C-calcite, H- hematite ..... 36

*Figure 3.11:* Reflectance spectra of 10% monazite complex mixtures with varying hematite abundance. Light grey: 1wt% hematite in 10% wt monazite complex mixture, dark grey 15 wt% hematite in 10 wt% monazite complex mixture ..... 37

*Figure 3.12:* Laboratory resampled spectra for AVIRIS and EnMap hyperspectral sensors to assess the capability of discriminating Pr feature from 10 wt% monazite, varying calcite and hematite spectra. note that broad Pr feature centred at 1572 nm is well preserved in both the sensors. .... 38

*Figure 3.13:* Laboratory resampled spectra for multispectral sensors, WV3- Worldview 3 super spectral sensor, LSN-Landsat Next super spectral sensor spectra to assess the capability of discriminating Pr feature from 10 wt% monazite, varying calcite and hematite spectra. note that broad Pr feature centred at 1580 nm is preserved resampled spectra of WorldView 3 sensor..... 39

*Figure 3.14:* Laboratory resampled spectra for WorldView 3 and Landsat Next multispectral sensors to assess the capability of discriminating Pr feature from 10 wt% monazite, 5 wt% hematite 85 wt% calcite sample; note that broad Pr feature centred at 1580 is detectable in WorldView 3 sensor. WV3-WorldView 3, LSN-Landsat Next. Note that the band centred at 1600 nm in Landsat Next sensor has gradual drops from both adjacent bands for both monazite mixed spectra and hematite spectra. .... 39

*Figure 3.15:* Comparison of resampled spectra with atmospheric absorption bands of the VNIR and SWIR range. Note that Pr feature falls within the atmospheric window. WV3-WorldView 3, LSN-Landsat Next, AV- AVIRIS..... 40

## Chapter 4

*Figure 4.1:* Absorption feature of Pr<sup>3+</sup> in synthetic monazite, annotating the spin orbit coupling levels of 4f<sup>2</sup> electrons in the ion and further splitting of the absorption feature due to crystal field effect. Note that the absorption features at 1370 and 1420 nm are due to Sm<sup>3+</sup>, and the ones near 1700 nm result from Nd<sup>3+</sup>. 44

*Figure 4.2:* Figure showing the reflectance spectra of siderite and Fe bearing dolomite from (Kokaly et al., 2017) with comparison synthetic monazite, note that broad absorption features of Ferrous ion and the possibility of affecting the broad feature to the REE features in SWIR region..... 49

## LIST OF TABLES

---

*Table 2.1:* REE oxides molar and mass abundances used for the synthesis experiments.....16

*Table 3.1:* The comparison of absorption feature positions of synthetic monazite and bastnäsite of the current with recently published data for monazite and bastnäsite from Turner et al. 2014 and 2016.....28

## LIST OF ABBREVIATIONS

---

REEs	Rare Earth Elements
LREEs	Light Rare Earth Elements
HREEs	Heavy Rare Earth Elements
VNIR	Visible and Near-Infrared
SWIR	Short-Wave Infrared
La	Lanthanum
Ce	Cerium
Pr	Praseodymium
Tb	Terbium
Dy	Dysprosium
Ho	Holmium
Er	Erbium
Tm	Thulium
Yb	Ytterbium
Lu	Lutetium
Sc	Scandium
Y	Yttrium
nm	Nanometre
syn	synthetic
SB	Synthetic Bastnäsite
NM	Natural Monazite
SM	Synthetic Monazite
ASD	Analytical Spectral Devices
FWHM	Full Width Half Maximum
AVIRIS	Airborne Visible-Infrared Imaging Spectrometer
WV3	WorldView 3
LN	Landsat Next
EnMap	Environmental Monitoring and Analysis Program
SRF	Spectra Response Function
GSL	Geo Science Laboratory

## LIST OF APPENDICES

---

Appendix 1: Photograph of the measurement set-up and the samples.....	56
Appendix 2: Table showing the description of the spectra used to get the averaged natural monazite spectra from Kokaly et al. (2017) .....	57
Appendix 3: Table showing the description of the spectra used to get the averaged natural monazite spectra from Percival et al. (2019) .....	57
Appendix 4: Table showing the description of the spectra used to get the averaged natural bastnäsite spectra from Kokaly et al. (2017) .....	58
Appendix 5: Table showing the description of the spectra used to get the averaged natural bastnäsite spectra from Percival et al. (2019) .....	58
Appendix 6: Diffractogram of calcite powder. Note that peaks are overlapping with reference data.....	59
Appendix 7: Diffractogram of hematite powder that has been used in the study.....	59
Appendix 8: Comparison of the spectra of calcite that has been used in the current study with hematite spectra of Kokaly et al. (2017).....	60
Appendix 9: Comparison of the spectra of calcite that has been used in the current study with hematite spectra of Kokaly et al. (2017).....	60
Appendix 10: Nd <sup>3+</sup> multiplet behaviour of bastnäsite 10% complex mixtures; note that the multiplets are not sharp compared to monazite mixtures .....	61
Appendix 11: Behaviour of the spectra of 10% monazite complex mixtures in VNIR range .....	61
Appendix 12: Laboratory resampled spectra of 10% monazite mixtures for hyperspectral sensors.....	61
Appendix 13: Laboratory resampled spectra of 10% monazite mixtures for multispectral sensors .....	62
Appendix 14: Scatter plot showing the re-adjusted band ratio vs hematite percentage resampled spectra for WorldView 3 sensor.....	62
Appendix 15: Scatter plot showing the re-adjusted band ratio vs hematite percentage resampled spectra for AVIRIS sensor.....	63

# 1. INTRODUCTION

## 1.1. Rare Earth minerals importance and geology

Rare earth elements (REEs) have gained importance as strategic metals in recent years due to their crucial role in manufacturing environmentally friendly and sustainable products (Balaram, 2019; Verplanck, 2017). Their distinct physical, chemical, magnetic, and luminescent properties contribute to various technological advantages, such as improved energy efficiency, enhanced performance, size reduction, speed, durability, and heat resistance (Gadea & Khan, 2023; Jordens et al., 2013). As the global demand for REEs continues to surge, the British Geological Survey, The United States Department of Energy, and the European Union declare REEs as critical raw materials (Cen et al., 2021; Gislev & Grohol, 2018). Countries such as China, Brazil, Vietnam, Australia, the United States of America (USA), Russia, and India fulfil the world's REE requirement (Balaram, 2019). Nevertheless, the escalating demand for REEs needs the exploration of more REE-bearing deposits.

Rare earth elements encompass seventeen elements on the periodic table, comprising lanthanides (atomic number 57 to 71), scandium (Sc, atomic number 21), and yttrium (Y, atomic number 39). These elements are typically classified into two primary categories by the International Union of Pure and Applied Chemistry (IUPAC) termed light rare earth elements (LREE, lanthanum (La), cerium (Ce), praseodymium (Pr), neodymium (Nd), promethium (Pm), samarium (Sm), europium (Eu)) and heavy rare earth elements (HREE, gadolinium (Gd), terbium (Tb), dysprosium (Dy), holmium (Ho), erbium (Er), thulium (Tm), ytterbium (Yb), and lutetium (Lu)) (Binnemans et al., 2018; Jordens et al., 2013).

The geological environments where REEs-bearing minerals are found include primary deposits like magmatic REEs deposits, namely carbonatites, alkaline igneous systems, and secondary deposits such as ion adsorption clay deposits and placer deposits (Balaram, 2019; Oliveira & Inverno, 2014). In most instances, REEs occur in their trivalent state except for  $\text{Eu}^{2+}$  and  $\text{Ce}^{4+}$  in certain cases (Turner et al., 2014). However, the majority of global REE production originates from REE fluorocarbonate minerals and REE phosphates-bearing deposits (Turner et al., 2014). These magmatic REE deposits typically contain calcite, dolomite, Fe-bearing dolomite, olivine, pyroxene, and iron-bearing minerals like magnetite, hematite, goethite, ilmenite in varying proportions (Anenburg et al., 2021). Regarding REE-bearing minerals, most deposits comprise bastnäsite (fluorocarbonate), parasite, monazite, xenotime, and apatite (Abaka-Wood et al., 2019; Turner et al., 2014, 2016).

## 1.2. Review of reflectance spectroscopy of REEs bearing minerals

Most absorption characteristics in REE minerals are governed by intra-configurational 4f-4f electron transitions between energy levels influenced by electron spin-orbit coupling within trivalent lanthanide ions. (Dijkstra et al., 2024; Turner et al., 2016). Clark et al. (1990) proposed that the absorption features of REEs remain unchanged with varying ligands attached to REEs. However, studies by Turner et al. (2014, 2016) indicate that absorption feature characteristics are contingent on ion concentration, and the location of the absorption feature relies on the cation's specific coordination and the asymmetry of the coordination. These absorptions are predominantly detectable in the ultraviolet and Visible Near Infra-Red (VNIR) portion of the electro-magnetic spectrum (Booyesen et al., 2019; Gadea & Khan, 2023; Rowan et al., 1986a; White, 1967). According to Turner et al. (2014, 2016) and Dijkstra et al. (2024), numerous trivalent lanthanides,

including  $\text{Nd}^{3+}$ , exhibit absorption features in the Short-Wave Infra-Red (SWIR) region Turner et al. (2014, 2016) expanded the existing spectral database of REEs by studying the spectra of REE phosphates and fluorocarbonates in both VNIR and SWIR regions, suggesting the potential of using reflectance spectroscopy of REE minerals for exploring REE mineral deposits.

Remote sensing exploration of REEs has emerged as a novel method for investigating REEs-bearing carbonatite bodies. (Zimmermann et al. (2016) examined geomorphic indicators combined with spectral data for REE deposits, while Booysen et al. (2019) illustrated the feasibility of multi-source and multi-scale approaches for REE mapping. Booysen et al. (2019) used multi-spectral satellite imagery to delineate regional geology, whereas hyperspectral imagery was utilised to identify zones enriched with REEs. Detecting REEs within dykes using the HyMap airborne hyperspectral sensor has proven challenging in the latter suggesting the necessity for high concentrations of REEs in a pixel to detect their absorption features (Booyesen et al., 2019).

Iron oxide is commonly present as an accessory mineral in most carbonatite bodies worldwide. Consequently, Booysen et al. (2019) demonstrated high concentrations of HREE in iron-rich dykes, suggesting a correlation between the presence of iron oxides and REEs. Recent studies by Tan et al. (2021) and Neave et al. (2016)) on VNIR spectroscopy of REEs have prompted systematic investigations of various REEs-bearing deposits. Tan et al. (2021) demonstrate the spectral characteristics of ion-exchangeable REE hosted by clay minerals by examining spectral features of different concentrations of synthesised REE-adsorbed kaolinite, halloysite, illite, and montmorillonite. Conversely, these authors delineate the potential influence of supergene iron oxides in iron oxide-bearing Nd adsorbed kaolinite on VNIR spectra as the spectral features of REEs diminish with increasing iron oxide concentrations. Additionally, the authors observed that 10 wt% of iron oxide minerals mask the Nd absorption features, even with a concentration of Nd as low as 600 ppm (Tan et al., 2021).

Neave et al. (2016) analysed various high-grade REE carbonatite rock samples from different regions, including Mountain Pass in the USA, Bayan Obo in China, and Mount Weld in Australia. They concluded that hyperspectral sensors like AVIRIS and EnMAP have adequate resolution to detect REEs, whereas resampled spectra from ASTER and Landsat 8 OLI lack the necessary resolution. They determined that the airborne platform's detection limit for  $\text{Nd}^{3+}$  is 30,000 ppm, based on highly REE-concentrated rock samples from Mountain Pass and Bayan Obo, which contrasts with the average REE concentration in calcic carbonatites, typically below 5000 ppm (Woolley & Kempe, 1989). This suggests the exceptionally high concentration of REEs in rock samples studied by Neave et al. (2016) to evaluate the detection limit for airborne platforms. Overall, previous studies present diverse and exceptional detection limits for REE detection across different remote sensing platforms.

Similarly, geoscientists have conducted studies to map lithologies potentially containing REEs in well-known areas to evaluate the feasibility of exploring REE-bearing deposits using airborne and spaceborne platforms. Rowan and Mars (2003) discussed the utilisation of ASTER imagery to identify REEs in Mountain Pass, employing ASTER data for mapping carbonatite exposures and AVIRIS imagery for extracting REE spectra. Additionally, Boesche et al. (2015) observed that less than 10% iron affects REE absorption features in the VNIR range, measured by the HySpex hyperspectral imager in carbonatite rocks in the Fen Complex in Norway. Researchers utilised overlapping iron and carbonatite features to identify regions of interest for REE mapping (Booyesen et al., 2019; Harmer & Nex, 2016)). These studies support the statement of Rowan et al. (1986) on combining  $\text{Fe}^{3+}$ ,  $\text{Fe}^{2+}$ , and  $\text{CO}_3$  absorption bands as a general indicator for detecting carbonatites, with the  $\text{Fe}^{2+}$  doublet being characteristic of carbonatites compared to sedimentary units.



Moreover, Boesche et al. (2015) highlight the importance of investigating the potential of iron oxide spectroscopy as a secondary indicator of carbonatitic rocks.

### **1.3. Research gap**

Scientists have studied the applicability of available remote sensing sensors to detect REEs, but some sensors do not have the capability to detect them (Boesche et al., 2015). Further, numerous studies have reported the influence of other mineral assemblages, such as iron oxides, on the narrow absorption features of REEs (Boesche et al., 2015; Neave et al., 2016). Turner et al. (2014, 2016) state the possibility of shifting absorption features with different mineralogy and concentrations of REEs. Similarly, most of the studies focused on REE absorption features in the VNIR region and the defined detection limits are based on VNIR spectra. The SWIR and Thermal Infra-Red (TIR) (3 – 14  $\mu\text{m}$ ) part of the spectra have yet to be systematically investigated to find the possibility of using spectral features of REE, carbonates and phosphates to identify REEs bearing deposits.

Accordingly, the effect of the concentration of REEs and other minerals assemblages, including iron oxides and carbonates, in absorption feature parameters has not been fully addressed. Also, the detectability of REE absorption features in the SWIR region hematite mixed mixture of REE minerals for different sensor specifications has yet to be addressed. The fulfilment of this knowledge gap will lead to understanding the use of combined spectral features of minerals as a proxy for REEs, which has not been attended to yet. However, as discussed by Neave et al. (2016), the heterogeneity of hand specimens and intense petrologic variability of carbonatites in the outcrop scale could affect the quality of expansion of spectral properties from hand specimens to the regional scale.

Therefore, this study aims to answer the above-mentioned knowledge gap by systematically examining the spectroscopy of synthetic REE minerals and their proxies, targeting basic mineral mixtures that could represent carbonatites in VNI and SWIR regions. Synthetic minerals are used to get a fundamental understanding of the behaviour of spectra. This study attempts to understand the influence of the concentration of different mineral assemblages on the absorption feature parameters of the REEs-bearing minerals and their proxies, such as carbonates and phosphates. Finally, this research will evaluate the applicability of current and future hyperspectral and multi-spectral sensors in detecting REEs, considering the characteristics of absorption features.

### **1.4. Objectives and research questions**

#### **1.4.1. Main objective**

To evaluate the applicability of current and future hyperspectral and multi-spectral sensors for mapping rare earth minerals in carbonatite by understanding the spectral characteristics of mineral mixtures of synthesised rare earth-bearing minerals and their proxies.

#### **1.4.2. Sub objectives**

SO 1: To examine the changes in spectral features of synthetic mineral mixtures with rare earth minerals, iron oxides and carbonates with changing mineral concentrations.

RQ1.1 Which REE absorption features can be observed in the VNIR and SWIR reflectance spectra of synthetic mineral mixtures with different mineral concentrations?

RQ1.2 How do the absorption feature parameters of REEs and their proxies ( $\text{CO}_3^{2-}$ ,  $\text{Fe}^{3+}$ ) change with the different proportions of synthetic minerals percentages?

RQ1.3 What changes in spectral features of REEs or their proxies ( $\text{CO}_3^{2-}$ ,  $\text{Fe}^{3+}$ ) can be used to identify REEs bearing deposits?

SO 2: To examine the spectral features of the synthetic mineral mixtures with changing mineral concentration after resampling laboratory spectra to hyperspectral airborne and spaceborne sensor specifications.

RQ2.1 What are the changes and the reasons for the changes in absorption feature parameters in resampled spectra?

RQ2.2 What is the possibility of identifying and distinguishing diagnostic spectral features of rare earth-bearing minerals in the mineral mixtures after resampling?

SO 3: To examine spectral features of the synthetic mineral mixtures with the change of mineral percentage after resampling the spectra to present and future multi-spectral sensor specifications.

RQ3.1 What are the changes and the reasons for the changes in absorption feature parameters in resampled spectra?

RQ3.2 What is the possibility of identifying and distinguishing diagnostic spectral features of rare earth-bearing minerals in the mineral mixtures after resampling?

RQ3.4 What are the possible spectral specifications for future sensors to detect rare earth element-bearing deposits?

## 2. METHODOLOGY

The research methodology consisted of three phases. Phases one and two were carried out in the Geo-Science Laboratory (GSL) of the ITC faculty at the University of Twente. REE mineral synthesis, making mineral mixtures and measuring reflectance spectra were achieved in these two phases. Phase three consisted of visual and quantitative analysis of the reflectance spectra and absorption feature parameters of the mineral mixtures and then resampling spectra for selected sensors.

### 2.1. Phase one – Mineral synthesis

REE phosphate-monazite and REE carbonate-bastnäsite were chosen as REE-bearing minerals for synthesis. According to the summary made with published mineralogical data of natural carbonatites by Castor (2008a, 2008b), Chen et al. (2017) and Simandl & Paradis (2018), monazite and bastnäsite are the most abundant REE-bearing minerals in carbonatites.

The synthesis was aimed to make close compositional representatives of naturally occurring monazite and bastnäsite ('natural like'). The composition of each REE in natural monazite and bastnäsite was reviewed and summarised using published concentrations by Chen et al. (2017) and Yang et al. (2014) to achieve this goal. According to this summary, La, Ce, Pr, Nd, and Sm are the most abundant REEs in monazites and bastnäsites in carbonatites. For this spectroscopic study, the concentrations of other LREE and HREE were deemed negligible as only Pr, Nd, and Sm are the REEs detectable in natural monazites using reflectance spectroscopy in VNIR and SWIR range (Dijkstra et al., 2024).

Our synthesis method uses REE oxides as the starting material. For synthesis, all oxides need to be dissolved. Most REE oxides are available as REE<sub>2</sub>O<sub>3</sub>, except for Pr<sub>6</sub>O<sub>11</sub> and CeO<sub>2</sub>. In the first attempt of dissolving REE oxides, the dissolution of Ce (IV) oxide (CeO<sub>2</sub>) was unsuccessful. Therefore, the reasons of practicality, La, Pr, Nd and Sm were selected as the REEs to include in synthesis, replacing the Ce content by La. Ultimately, relative REE molar proportions to synthesise 'natural like' monazite and bastnäsite were decided as (La<sub>0.78</sub>, Pr<sub>0.05</sub>, Nd<sub>0.15</sub>, Sm<sub>0.02</sub>)PO<sub>4</sub> and (La<sub>0.84</sub>, Pr<sub>0.04</sub>, Nd<sub>0.10</sub>, Sm<sub>0.02</sub>)(CO<sub>3</sub>)(F, OH), respectively based on summarised concentrations of each REEs inside REE minerals. The main assumption for the synthesis of monazite and bastnäsite was that no fractionation occurred during synthesis, i.e. if no fractionation occurs, dissolution of the desired mixture of oxides with the desired REE molar proportions would lead to precipitation of a solid-solution product with the desired bulk composition.

Analytical-grade chemicals were used for the synthesis. REE oxides were used as the source of REE: praseodymium oxide (Pr<sub>6</sub>O<sub>11</sub>) with 99.5% purity, neodymium oxide (Nd<sub>2</sub>O<sub>3</sub>) with 99.9% purity and samarium oxide (Sm<sub>2</sub>O<sub>3</sub>) with 99.9% purity were purchased from Strategic Elements, Deggendorf, Germany. Lanthanum oxide (La<sub>2</sub>O<sub>3</sub>) was purchased from Merck Life Science, Amsterdam, Netherlands, with a reported >99.5% purity. REE oxides were subjected to calcining in the furnace at 900°C for 12 hours to ensure that the REE oxides were fully dehydrated (no REE hydroxides present).

Other chemicals needed for monazite synthesis include concentrated orthophosphoric acid (conc. H<sub>3</sub>PO<sub>4</sub>) (85%) purchased from Merck Life Science, Amsterdam, Netherlands, and ultra-pure water (Millipore, resistivity >18.2 MΩ·cm at 25°C). The chemicals needed for bastnäsite synthesis include concentrated hydrochloric acid (conc. HCl) (36%), Na<sub>2</sub>CO<sub>3</sub> and NaF powders purchased from Merck, Darmstadt, Germany. The glassware used for synthesis was washed with 10% diluted HNO<sub>3</sub> and rinsed three times with ultrapure water to remove potential contamination.

Both monazite and bastnäsïte were synthesised using a precipitation method followed by high-temperature heating for monazite, following Dijkstra et al. (2024). Aiming for 11 g of synthesised powders, which would be sufficient for the subsequent mixing experiments, the corresponding masses for a total of 0.05 mol of lanthanides for both monazite and bastnäsïte were calculated using equation 2.1 and weighted out using a high-precision six-digit balance. The detailed masses measured for the synthesis are mentioned in Table 2.1. The weights of the intermediate and final synthesised products were measured to calculate the yield of the reaction (% yield = 100 x (actual yield of product in gram / theoretical yield of product in gram)) and to calculate the loss of ignition during high-temperature heating of rhabdophane.

$$\text{Required lanthanides (mol), } (b) = 0.05 \times \text{Relative molar proportions, } (a)$$

$$\text{Mass measured(g), } (m) = \frac{\text{Requires lanthanides (mol), } (b)}{\text{no. of lanthanide atoms in oxide}} \times \text{Oxide mass (g/mol)}$$

2.1

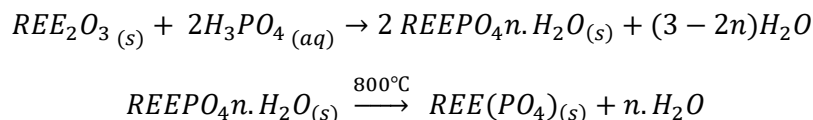
Table 2.1: REE oxides molar and mass abundances used for the synthesis experiments.

REE Oxides	Monazite			Bastnäsïte		
	(a) Relative molar proportions	(b) Required lanthanides (mol)	(m) measured mass (g)	(a) Relative molar proportions	(b) Required lanthanides (mol)	(m) measured mass (g)
La <sub>2</sub> O <sub>3</sub>	0.78	0.0390	6.3533	0.84	0.042	6.842
Pr <sub>6</sub> O <sub>11</sub>	0.05	0.0025	0.4256	0.04	0.002	0.3405
Nd <sub>2</sub> O <sub>3</sub>	0.15	0.0075	1.2618	0.10	0.005	0.8412
Sm <sub>2</sub> O <sub>3</sub>	0.02	0.0010	0.1744	0.02	0.001	0.1744
<b>Total</b>	1.00	0.0500		1.00	0.0500	

### 2.1.1. Monazite synthesis

The complete chemical reaction of the synthesis is mentioned in equation 2.2. Weighed REE oxides (Table 2.1) were dissolved together in 135 ml of concentrated H<sub>3</sub>PO<sub>4</sub>, with 10 ml ultra-pure water added to reduce the viscosity. The solution was continuously magnetic stirred until the oxides were fully dissolved, which took 1.5 to 2 hours. Then, the solution was diluted up to 250 ml with ultrapure water and stirred with a magnetic stirrer. After that, the solution was boiled vigorously on a hotplate for 2 to 2.5 hours. Eventually, hydrated REE-phosphates were precipitated, making the solution cloudy. The precipitation was settled in the bottom of the beaker after keeping the solution still for 2 hours. Next, the suspension was washed by centrifuging the precipitation with ultrapure water at 1500 rpm for 3 minutes, and the clear supernatant was decanted. The centrifuging and decanting were repeated until the supernatant liquid was pH neutral. The centrifuging was used to speed up the neutralising process and to preserve the finest particle size fraction (which is a modification of the process of (Dijkstra et al., 2024), who used a 2 µm filter paper to filter and neutralise the precipitate). The pH-neutralised intermediate product was dried at 60°C for 48 hours in the

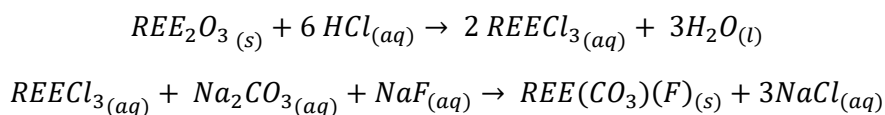
oven. Then, the weight of the sample was measured, and X-ray powder diffraction (XRD) analysis was carried out to confirm the intermediate product as rhabdophane ( $[\text{REE}]\text{PO}_4 \cdot n \text{H}_2\text{O}$ ) (Figure 3.1). After that, rhabdophane was heated in a furnace for 6 hours at 800 °C to dehydrate, followed by a gradual cooling inside the furnace to room temperature while the door of the furnace was opened. The final product was confirmed as monazite by X-ray diffraction (XRD) analysis.



2.2

### 2.1.2. Bastnäsite synthesis

The complete chemical reaction of the synthesis is mentioned in equation 2.3. Weighted REE oxides (Table 2.1) were dissolved together in 20 ml of concentrated HCl having an excess amount (15% more) of HCl than needed (18.25 ml) to ensure that all the lanthanides were dissolved well and availability of at least three chloride ions for every  $\text{Ln}^{3+}$  ion. Then, the solution was diluted up to 75 ml with ultra-pure water and magnetic stirred for 1.5 to 2 hours while heating on a hotplate at 95°C temperature to ensure a complete dissolution of oxides. Meanwhile, 10.006 g of  $\text{Na}_2\text{CO}_3$  (ensuring one  $\text{CO}_3^{2-}$  for every lanthanide, plus an excess to neutralise HCl and make the solution neutral to alkaline) and 2.707 g of NaF (ensuring one F for every lanthanide in fluorobastnäsite, plus a 30% excess to ensure a  $\text{pH} > 10$ ) were dissolved in 100 ml and 50 ml of ultra-pure water, in separate beakers covered with clean watch glasses. All these solutions were magnetic stirred while heating up to 95°C temperature on a hot plate to ensure fully dissolving. Then, the dissolved  $\text{Na}_2\text{CO}_3$  was instantaneously added to the fully dissolved REE chloride solution while magnetic stirring was continued. This triggered precipitation, and the solution instantly became a cloudy viscous suspension. After 30 seconds, the dissolved NaF was added, and the solution was stirred for one more minute. Then, the solution was kept still until the bastnäsite powder was settled. The powder settled within 15 minutes. However, it was noted in the previous trial experiments that adding them slowly or drop-wise or adding solutions with significant temperature differences could also lead to a cloudy solution without suspension. Therefore, it is suggested that all three solutions be at nearly the same temperature prior to mixing to avoid this issue in the future. Additionally, it is better to avoid a time gap of more than one minute between adding NaF and  $\text{Na}_2\text{CO}_3$ , as a longer delay can also lead to a cloudy solution without proper suspension. The remaining fully transparent alkaline supernatant solution was removed by careful decanting. The settled powder was repeatedly washed with ultra-pure water by carefully pouring along the wall of the borosilicate beaker and decanting the supernatant until the pH was below 8. It was found from the previous trial experiments that the centrifuging process used in monazite neutralising was not successful for neutralising bastnäsite as it made a cloudy solution, which did not settle later. The suspension was left to dry at 60°C for 2.5 hours in the oven. An XRD analysis was carried out to confirm the mineral as bastnäsite.



2.3

### 2.1.3. Calcite and Hematite

Laboratory standard calcite and hematite powder were used to create the mineral mixtures. Calcite with >99% purity was purchased from Merck Life Science, Amsterdam, Netherlands. Fine-grained hematite was taken from the chemical store of the Geoscience Laboratory, but the provenance of this material could not be traced. However, XRD analysis clearly identified the mineral as hematite, with the diffractogram revealing no peaks attributable to other mineral phases. The XRD analysis of calcite and hematite used for the study is shown in Appendix 6.

### 2.1.4. XRD analyses

The powder X-ray diffraction (PXRD) analysis was carried out for all mineral powders and intermediate products using a Bruker D2 Phaser instrument (Bruker, 2024c). Since the final products were synthesised as aggregates, they were delicately milled using an agate mortar and pestle to break down the aggregates into powder without causing damage to the material. The powders were placed on a standard Bruker specimen holder of 2.5 cm diameter made of amorphous polymethyl methacrylate (PMMA) (Bruker, 2024b). The sample holder was filled with the powder and levelled using a clean glass plate while gently compacting. A Cu anode with  $K \alpha_1$  0.1540562 nm was used as the X-ray source. The measurements were taken from 6° to 80° two theta range integrating more than 12 scans per sample. The run time was 656.6 seconds per analysis, resulting in a total analysis time of two hours and 30 minutes per sample. The increment, divergence slit, knife and detector slit were adjusted to 0.012°, 0.6 mm, 8 mm, and 8 mm, respectively. Diffrac-EVA software by Bruker (Bruker, 2024a) was used to pre-process data and interpretations.

## 2.2. Phase two - Data acquisition

In this phase, powdered minerals were mixed with different weight percentages, reflecting the natural modal abundances of minerals in carbonatites, followed by reflectance data acquisition using the Analytical Spectral Device (ASD) Fieldspec®3 Spectroradiometer (ASD Inc, 2010) of ITC faculty.

### 2.2.1. Sample preparation

Three mixing methods were tested to find the optimal method for obtaining homogenous mixtures, as it was important to get accurate spectra reflecting desired mineral abundances in the mixture. Three mixtures with two grams of calcite and hematite were prepared: one by shaking the mineral powders in a petri dish, one by mixing in a glass tube and one by mixing in an agate mortar and pestle. For the shaking, a glass tube was rotated and shaken in every direction to reduce the effect of gravity on the mineral grain arrangement. All three mixing procedures took 3 minutes per sample. Then, six spectral measurements were collected from each mineral mixture. The mortar and glass tube methods gave the lowest standard deviation in these repeated spectral measurements (Figure 2.1); tube mixing, and mortar and pestle mixing were therefore combined to create mixtures to avoid making lumps with tube mixing. After finalising the mixing method, another trial mixing was carried out by weighing the trial sample's weight both before and after mixing to determine any weight loss due to transferring from glass tubes to the agate or other causes. The weight loss was found to be less than 0.001g. One hundred glass tubes were washed in an ultrasonic bath for 4 minutes and washed with diluted aqua regia, followed by ultra-pure water washing to ensure clean glass tubes for

mixing. Time was used as the control for mixing, maintaining two-minute tube mixing followed by one-minute mortar and pestle mixing and repeated one-minute tube mixing.

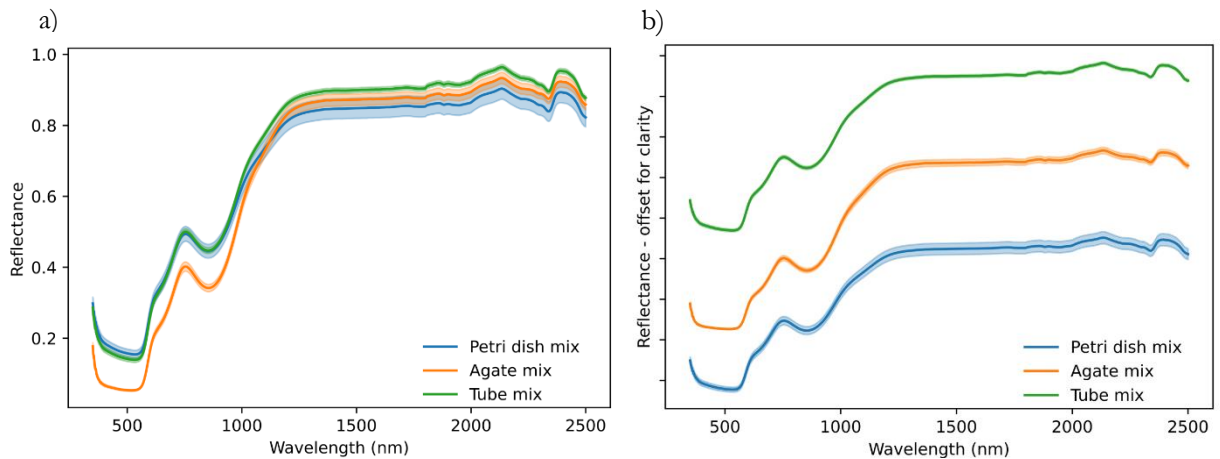


Figure 2.1: Graph showing the standard deviation of six spectral measurements taken to find the optimal mineral mixing method for obtaining a homogenous mixture; blue: petri dish mix, orange: agate mix, green: tube mix, b) the same graph with stacked reflectance values for better visualisation, note the higher standard deviation of six measurements in petri dish mixing compared to the agate and tube mix.

## 2.2.2. Mineral mixtures

A literature study was carried out using geochemical and mineralogical data from Castor (2008b, 2008a) to understand the mineralogy and general abundance of REE oxides, carbonates, and iron oxides in REE-bearing carbonatites, including Mountain Pass and Bayan Obo. The general abundance of REE oxides and iron oxides varies from a few percent to 10-15 wt%, while carbonate percentage is reported as more than 50 wt% in carbonatites. (Castor, 2008b; Le Maitre et al., 2004; Vladykin & Pirajno, 2021). Based on these typical mineral abundances found in carbonatites, the weight percentages for complex mineral mixtures were determined. Altogether, 82 samples were prepared, including 24 complex mixtures using monazite, hematite, calcite, 24 complex mixtures using bastnäsite, hematite, calcite, 29 simple mixtures of two minerals and five pure minerals (synthetic monazite, synthetic bastnäsite, hematite, calcite, and natural monazite of ITC mineral collection) to understand the behaviour of spectra. A cap of 30 wt% was set for the proportion of REE minerals in complex mixtures. This is guided by the fact that the complex mixtures containing more than 20 wt% of REE minerals do not represent natural carbonatites. The weight of each mineral mixture was 800 mg. The ternary diagram in Figure 2.2 shows the mixtures that were made with weight percentage. In this thesis, ‘complex mixtures’ refer to a mixture of three minerals, while ‘simple mixtures’ refer to a mixture of two minerals.

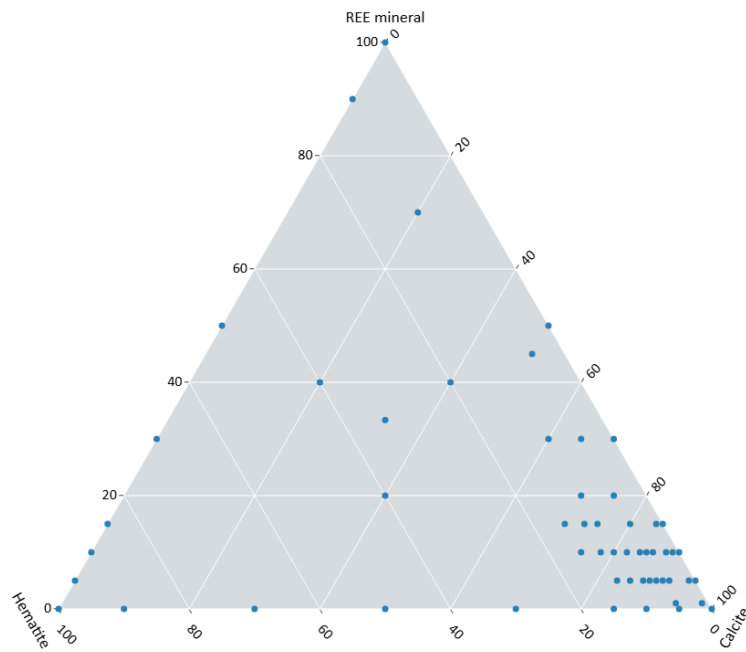


Figure 2.2: Ternary diagram showing the composition of each mineral mixture by weight percentages.

### 2.2.3. Spectral measurements

An Analytical Spectral Device (ASD) Fieldspec®3 Spectroradiometer (ASD Inc, 2010) was used for the VNIR and SWIR reflectance measurements, which covers a wavelength range of 350 to 2500 nm, recording spectral reflectance in 2151 bands. The instrument consists of three detectors: VNIR, SWIR1 and SWIR2. The spectral resolutions of the three sensors are ~3nm FWHM at 700 nm and 10 nm FWHM at 1400 nm and 2100 nm, respectively, for VNIR, SWIR1 and SWIR2. The sampling interval of the instrument is ~1.4 nm for the spectral region 350-1000 nm and 2 nm for the spectral region 1000-2500 nm. The pistol grip with a 25° field of view (full conical angle) was connected to the fiber optic cable, which comprises fifty-seven randomly distributed silica glass fibers, evenly distributing nineteen fibers for each sensor. Artificial illumination was provided during the measurements using a 235W, 230V quartz tungsten halogen lamp (Lowel Lighting, 2024). A 99% reflective Spectralon® standard white reference plate (4 cm diameter) (Labsphere, 2022) was used to normalise the radiance measurements to reflectance values (between zero and one).

The experimental set-up illustrated in Figure 2.3 (see the photograph in Appendix 1) was arranged in a dark room. The pistol grip with fiber optics was fixed directly above the sample holder, maintaining 4.5 cm from the sample to the fiber opening, getting a field of view of ~3.15 cm<sup>2</sup> (diameter of 2 cm). The samples were placed on flat, 4 cm diameter quartz glass plates over a dark background with a flat and near-zero reflectance. The dark background under the glass plates and the surroundings was used to reduce interference from extraneous light. The samples were prepared to cover a circular area of at least 2.5 cm diameter with 1 mm thickness. An illumination angle of 24° was maintained throughout the measurements to ensure a higher diffuse reflection than specular reflection. The instrument was switched on 30 minutes before measurements to stabilise the temperature. Six replicate measurements were taken for each mixture to reduce the error with homogeneity of mixtures and to reduce the effect of optical fibers being aimed at different areas of the sample. White reference measurements were taken after every five samples, ensuring the same point of view on the white reference to maintain consistency throughout the measurement series. Altogether, 492 spectra



were collected for all 82 mixtures in one day, assuming the same laboratory environment and light conditions throughout the measuring. A splice correction with experimental slope correction was performed on measured spectra using the ViewSpec Pro™ software (ASD Inc, 2010) to correct for offsets between the different detectors.

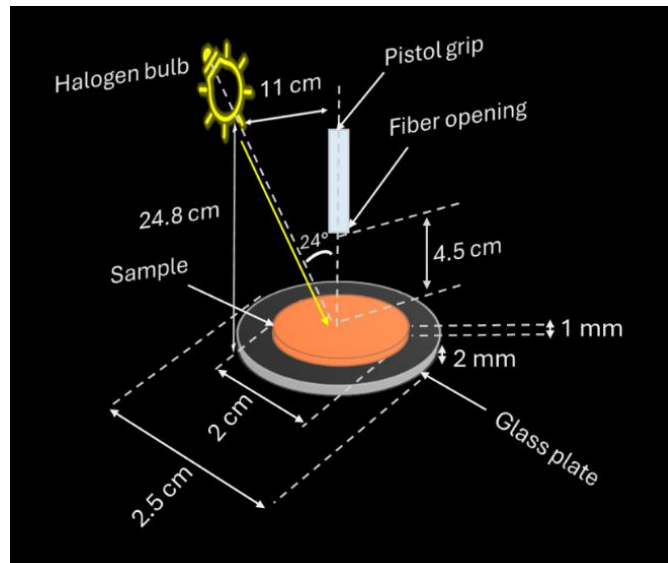


Figure 2.3: Illustration of the set-up used for reflectance spectroscopy measurements on mixed-mineral powders in the laboratory dark room.

### 2.3. Phase three- Spectral data analyses

The splice-corrected spectral measurements were averaged before rescaling by dividing the reflectance values by 1.04; the spectra needed to be rescaled as there were some reflectance measurements in the SWIR range for mixtures with calcite where reflectance values measured above 1.0. This is assumed to be because of the very high reflectance of laboratory-standard pure, white-coloured calcite with respect to the Spectralon® white reference.

The spectral data analysis phase consisted of three stages. In stage 1, the pure minerals of the study (synthetic natural like monazite, synthetic natural like bastnäsite, hematite and calcite) were compared with published spectral libraries. This comparison was done to assess the representativeness of synthetic minerals and the other pure minerals compared to the spectra of naturally occurring minerals. In stage 2, high-resolution spectra of the mixtures were analysed to evaluate and understand the effect of calcite and hematite on REE spectra with varying concentrations of three minerals. Finally, in stage 3, the high-resolution spectra were resampled to hyperspectral airborne/spaceborne sensors and multi-spectral sensors to address the remaining research questions.

#### 2.3.1. Spectral analysis of pure minerals

In this stage, pure mineral spectra from the current study were compared with the published library from Kokaly et al. (2017): spectral library version 7 of the United States Geological Survey (USGS), published spectral library from Percival et al. (2019): The National Mineral Reference Collection (NMC) Digital Spectral (VIS-NIR-SWIR) Library, Part II: REE-Nb-U-Th-bearing minerals by Geological Survey of Canada, and the spectra of natural monazite in ITC mineral collection to assess the representativeness of the synthesised pure minerals of our study to the naturally occurring minerals. Average spectra of the REE

minerals from the published library, which were measured with an ASD Spectrometer, were taken as averaging the spectra of multiple samples captures the natural variability and heterogeneity of lithologies, providing a more comprehensive and realistic representation of the mineral's spectral characteristics for accurate comparison with synthetic mineral spectra. An average of eight monazite spectra (Appendix 2) from Kokaly et al. (2017), an average of six monazite spectra (Appendix 3) from Percival et al. (2019), the spectra of the powdered natural monazite from the ITC collection were compared with synthetic monazite spectra. The spectra of bastnäsite from Kokaly et al. (2017) (Bastnaesite\_REE\_WS320\_ ASDFRbb) averaged spectra (Appendix 5) from Percival et al. (2019) were compared with synthetic bastnäsite spectra. The spectra of hematite (HS45.3\_ ASDFRb) and calcite (GDS304 75-150um ASDFRb) from Kokaly et al. (2017) were compared with hematite and calcite used in the study.

As the final step of comparison, the wavelength position of each REE ion absorption feature in synthetic minerals was compared with recent literature on monazite and bastnäsite by Dijkstra et al. (2024) and Turner et al. (2014, 2016) to understand the origin of the features. Further laboratory-synthesised monazite and bastnäsite spectra were compared with each other to identify and understand possible changes in absorption features between the spectra.

### 2.3.2. Mineral mixture spectral data analysis

The investigation of the spectral behaviour of complex mineral mixtures began with a visual examination of spectra of simple mineral mixtures, including combinations of a REE mineral with either calcite or hematite, as well as calcite-hematite mixtures. Following this, spectra and absorption feature parameters of complex mineral mixtures were both visually and qualitatively analysed. The aim of the absorption feature parameter analysis of these complex mixtures was to identify the features that are statistically significant for detecting REEs in hematite-mixed spectra.

The form of individual absorption features is affected by the overall spectrum shape, known as the background continuum or hull, which is frequently eliminated before further analysis of the absorption parameters. Additionally, the way in which an absorption feature's shoulders are defined has a significant impact on the resulting parameters. When the shoulders are defined as the points where the spectrum contacts its convex hull, the complete depth of the feature is obtained (Hecker et al., 2019). Knowing these facts, a continuum removal was applied to the spectra by calculating the convex hull and removing it by division (Clark & Roush, 1984). This normalisation was done to remove the variations in overall reflectance. The spectral parameters considered in this study, i.e. absorption feature depth and the absorption feature position, are defined in Figure 2.4. The Hyperspectral Python (HypPy) software (Bakker, 2022) was used to extract the local minima (absorption feature position) and the depth of the absorption features between different wavelength ranges in the VNIR and SWIR regions separately. The HypPy software uses a parabolic interpolation of three bands (Figure 2.4), centring the minimum reflectance band in the continuum removed absorption feature to calculate the local minima and the absorption feature position (Van Ruitenbeek et al., 2014). The respective spectral math expression for absorption feature parameter extraction is  $1 - (S[700.0:1200.0].nohull()).localminfit(1)$ , where S is the respective spectrum.

The spectra of complex mineral mixtures and pure end members were compared to identify which REE absorption features remained visible after mixing REE minerals with calcite and hematite. Subsequently, the spectra of complex mixtures containing monazite and bastnäsite were compared. Detailed observations indicated that the absorption features of REEs in bastnäsite mixtures were weaker compared to those in

monazite mixtures. Consequently, only complex mineral mixtures containing monazite were subjected to further qualitative analysis.

The spectral parameters of monazite mineral mixtures were further explored by grouping the averaged spectra for complex mineral mixtures, mixtures containing 5, 10, or 15 wt% monazite, with varying hematite and calcite modal abundances and mixtures containing 5 or 10 wt% hematite, with varying monazite and calcite modal abundances to understand the behaviour of spectral characteristics of mixtures. REE absorption features in the VNIR range were visually analysed considering the continuum removal spectra between 730-760 nm, 760-840 nm, and 700-1200 nm, focusing the absorption feature depths of Nd<sup>3+</sup> features at 742, 805, 872 nm, absorption feature position of 872 nm. The SWIR range absorption features were analysed separately, considering the feature depths of all REE features present in the SWIR region. Considering the observed changes, the absorption feature position and depth of 872 nm feature and feature depths of all absorption features in the SWIR range were decided as the spectral parameters to consider for further quantitative analysis for complex mixtures. Possible relationships between the spectral parameters and modal abundance of monazite were examined using different scenarios. Scenario 1: the change of the spectral parameter with changing monazite modal abundance(%wt), 2: change of spectral parameter with hematite modal abundance(%wt) and 3: change of spectral parameter with modal abundance (%wt).

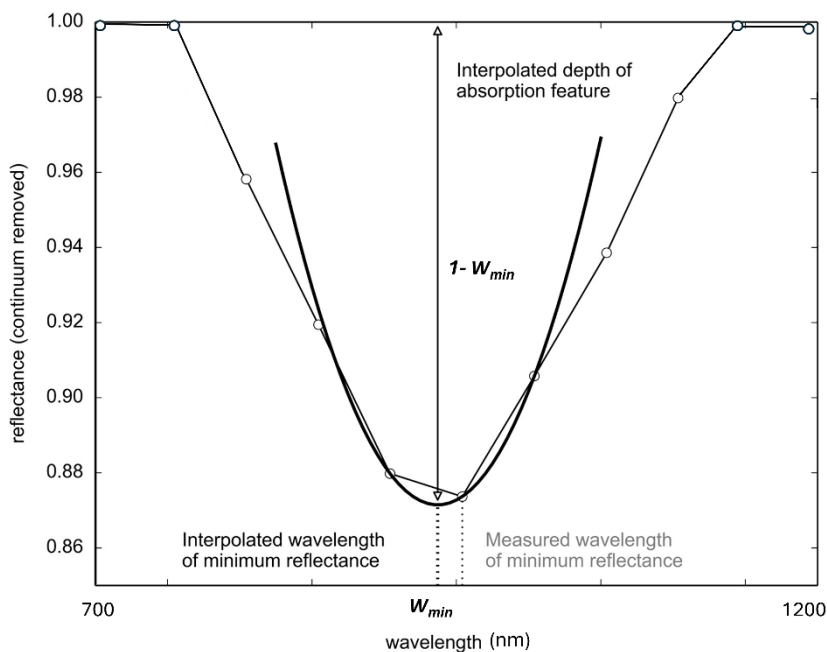


Figure 2.4: A sketch showing the parabolic interpolation method to extract local minima from continuum removed absorption feature by fitting a parabola through three consecutive measurement points. (After Van Ruitenbeek et al., 2014)

After spectral parameter analysis, it was noted that the depth of the Pr feature at 1472 and 1582 nm linearly correlates with increasing monazite in complex mixtures, and the feature is visible even with 10 wt% hematite in 10 wt% monazite samples. Therefore, a band ratio was developed to detect the Pr feature centred around 1472 and 1582 nm, as the Pr feature is the most promising feature in hematite mixed spectra. To reduce the effect of noise, the mean of the spectral range was proposed to create the band ratio. The wavelength ranges of the shoulders of the Pr absorption feature, where hematite or calcite do not have absorption features, were taken as the numerator, and 20-30 nm wavelength range centring absorption feature at 1472 and 1582 nm was taken as the denominator (Figure 2.5).

This ratio for Pr detection in laboratory spectra, henceforth referred to as ‘Praseodymium Ratio (PrR)’, was defined as follows (equation 2.4, in Hyppy bandmath scripting format).

$$\text{Praseodymium Ratio (PrR)} = \frac{[1759:1787].\text{mean}() + [1506:1520].\text{mean}()}{[1555:1580].\text{mean}() + [1456:1470].\text{mean}()}$$

2.4

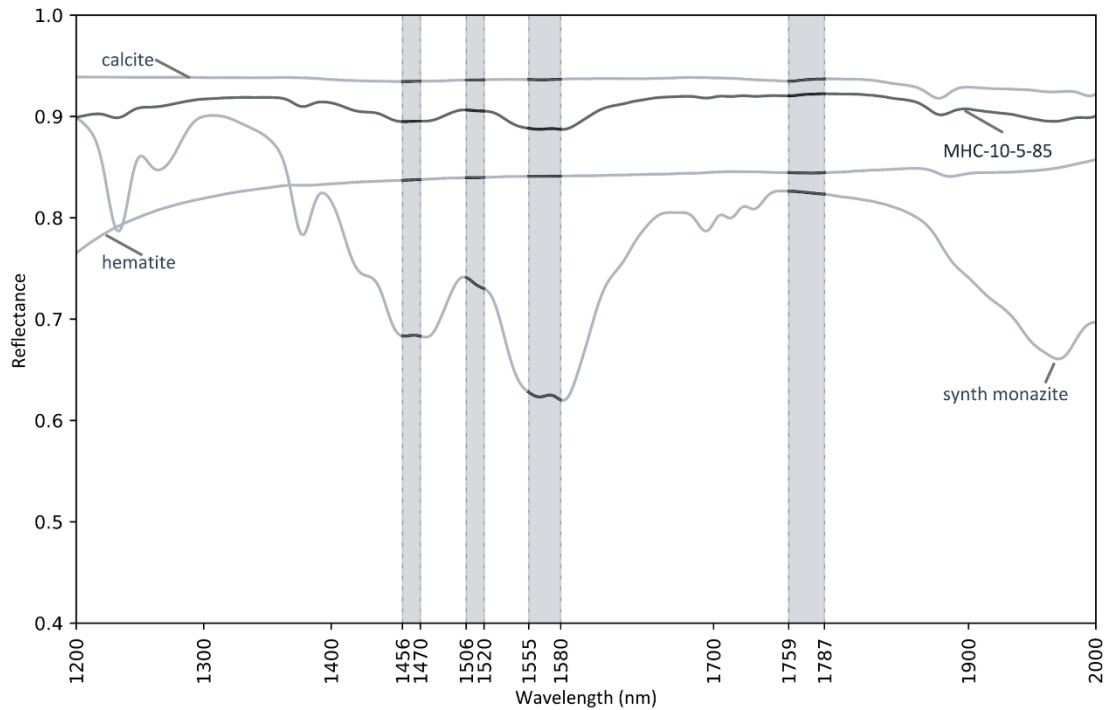


Figure 2.5: The wavelength ranges considered for the diagnostic Praseodymium Ratio(PrR) put forward in this thesis; MHC-10-5-85 is the reflectance spectra of 10 wt% monazite, 5 wt% hematite and 85 wt% calcite powdered mineral mixture, note that mean reflectance value of the wavelength ranges between 1759:1787 and 1759:1787 taken as numerator 1555:1580 and 1456:1470 as denominator centring the Pr absorption feature. Note the absence of absorption features of hematite and calcite spectra for the considered wavelength range.

### 2.3.3. Resampling laboratory spectra to hyperspectral and multispectral sensors

Spectral resampling transforms a high-resolution spectrum to match the spectral characteristics of a specific sensor. This process involves selecting the portion of the high-resolution spectrum within the sensor's target wavelength range and then adjusting the data according to the Spectral Response Function (SRF) of the wavelength range. The adjusted reflectance values are summed and normalized to represent the entire spectral band, resulting in a single reflectance value that simulates the sensor's detection over its defined wavelength range. Four well-known current and planned space and airborne sensors were selected for resampling: AVIRIS hyperspectral airborne sensor, EnMap hyperspectral spaceborne sensor and WorldView3 and Landsat Next multi-spectral sensors.

The Airborne Visible InfraRed Imaging Spectrometer (AVIRIS) is developed/operated by Jet Propulsion Laboratory (JPL), National Aeronautics and Space Administration (NASA) with four spectrometers dividing

total of 224 contiguous spectral bands into four spectrometers - 32 bands for spectrometer A and 64 bands for remaining three spectrometers: B, C, D. The instrument covers wavelength ranges from 380 to 2500 nm with approximately 10 nm spectral bandwidth. The spatial resolution of the instrument varies between 1-4 m to 20 m depending on the altitude of the aircraft (Green et al., 1998). AVIRIS classic sensor specifications were used for resampling as a representative of airborne sensors such as HyMap AVIRIS Next Generation (AVIRIS-NG). However, AVIRIS-NG has a higher resolution in SWIR ( $5 \pm 0.5\text{nm}$ ) than ASD field spec 3.

The Environmental Mapping and Analysis Program (EnMAP) is hyperspectral satellite mission managed by German Space Agency, DLR Bonn acquiring reflectance from the earth at wavelength range from 420 nm to 2450 nm in 246 contiguous spectral bands with  $8.1 \pm 1.0\text{nm}$  spectral bandwidth (FWHM) in VNIR range (420-1000 nm) and  $12.5 \pm 1.5 \text{ nm}$  spectral bandwidth (FWHM) in SWIR range (900-2450 nm). The EnMAP mission is currently in its operational phase, collecting data with a spatial resolution of 30 m (Chabrilat et al., 2022).

Landsat Next multi-spectral satellite mission is planned to launch in late 2030 under the Sustainable Land Imaging (SLI) Program by NASA and USGS. Landsat Next contains a total of 26 super-spectral bands, including eleven bands of Sentinel 2 synergy in the VNIR and SWIR range and three TIR bands of ASTER synergy. Landsat Next is designed to acquire data with 10-20 m spatial resolution in VNIR and SWIR bands and 60 m spatial resolution in the TIR range (U.S. Department of the Interior & U.S. Geological Survey, 2024). Landsat Next, incorporating the combined spectral capabilities of Sentinel-2 and ASTER, serves as a comprehensive representative for most multi-spectral sensors. However, Worldview 3 super spectral high-resolution commercial satellite sensor specification is also considered as it contains three spectral bands between 1500 to 1800 nm atmospheric window. Worldview 3 satellite contains eight VNIR spectral bands with 1.24 m spatial resolution, eight SWIR bands with 3.7 m spatial resolution and 30 m resolution in the CAVIS (Clouds, Aerosols, Vapours, Ice and Snow) bands.

In this study, spectral resampling of ASD high-resolution reflectance spectra to lower spectral resolution was conducted using the ENVI version 6.0 spectral resampling tool (Exelis Visual Information Solutions, Boulder, Colorado). The spectral response functions for the sensors considered in the current study, except for the WorldView-3 sensor, are not included in the predefined spectral response functions in the ENVI resampling tool. Consequently, a Gaussian model was employed, with the mean and standard deviation set to the band wavelengths and FWHM, respectively. This model was used to resample the spectra to match the EnMAP, Landsat Next, and AVIRIS sensors.

After resampling the ASD-acquired laboratory spectra to the sensors mentioned above, the band ratio developed in section 2.3.2 was re-adjusted to see the applicability of the Pr band ratio in remote sensing.

### 3. RESULTS

#### 3.1. Mineral synthesis

The colour of the final product of both monazite and bastnäsite synthesis was off-white and showed as a fine powder. The XRD results of the intermediate product of monazite synthesis (see Figure 3.1) confirmed hydrous REE phosphate (rhabdophane -  $\text{REEPO}_4 \cdot n\text{H}_2\text{O}$ ). The final product after high-temperature heating was confirmed as monazite. The direct precipitation of the bastnäsite synthesis process is also confirmed as bastnäsite with XRD analysis. The XRD patterns of synthetic monazite compared with natural monazite from the ITC mineral collection showed similar XRD patterns for the first 40 degrees (2 theta), while the peaks of natural monazites are more subdued, after 40 degrees (2 theta), as shown in Figure 3.1. The intermediate product of monazite synthesis weighed 11.7 g. The loss on ignition (the transformation from  $(\text{La, Pr, Nd, Sm})\text{PO}_4 \cdot n\text{H}_2\text{O}$  to  $(\text{La, Pr, Nd, Sm})\text{PO}_4$ ) is 0.78 g giving that n value for H<sub>2</sub>O is between 0.7 and 0.8. However, to calculate an accurate n value, thermo gravimetric analysis is more suitable, which we did not carry out in this study. Though the mass expected from monazite and bastnäsite synthesis was 11.75 g and 10.94 g, the final products of synthesis weighed 10.97 g and 10.67 g, respectively, resulting in a yield of 93.3% for monazite and 97.5% for bastnäsite.

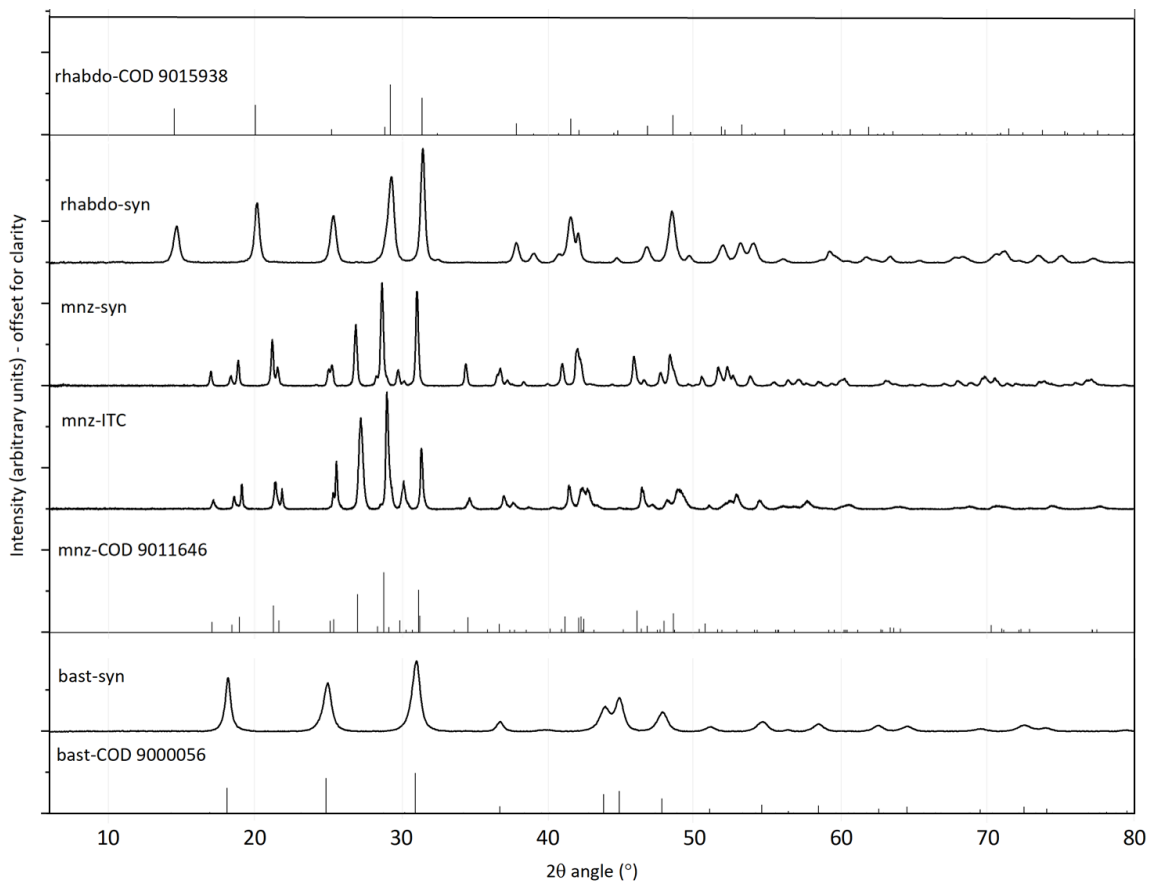
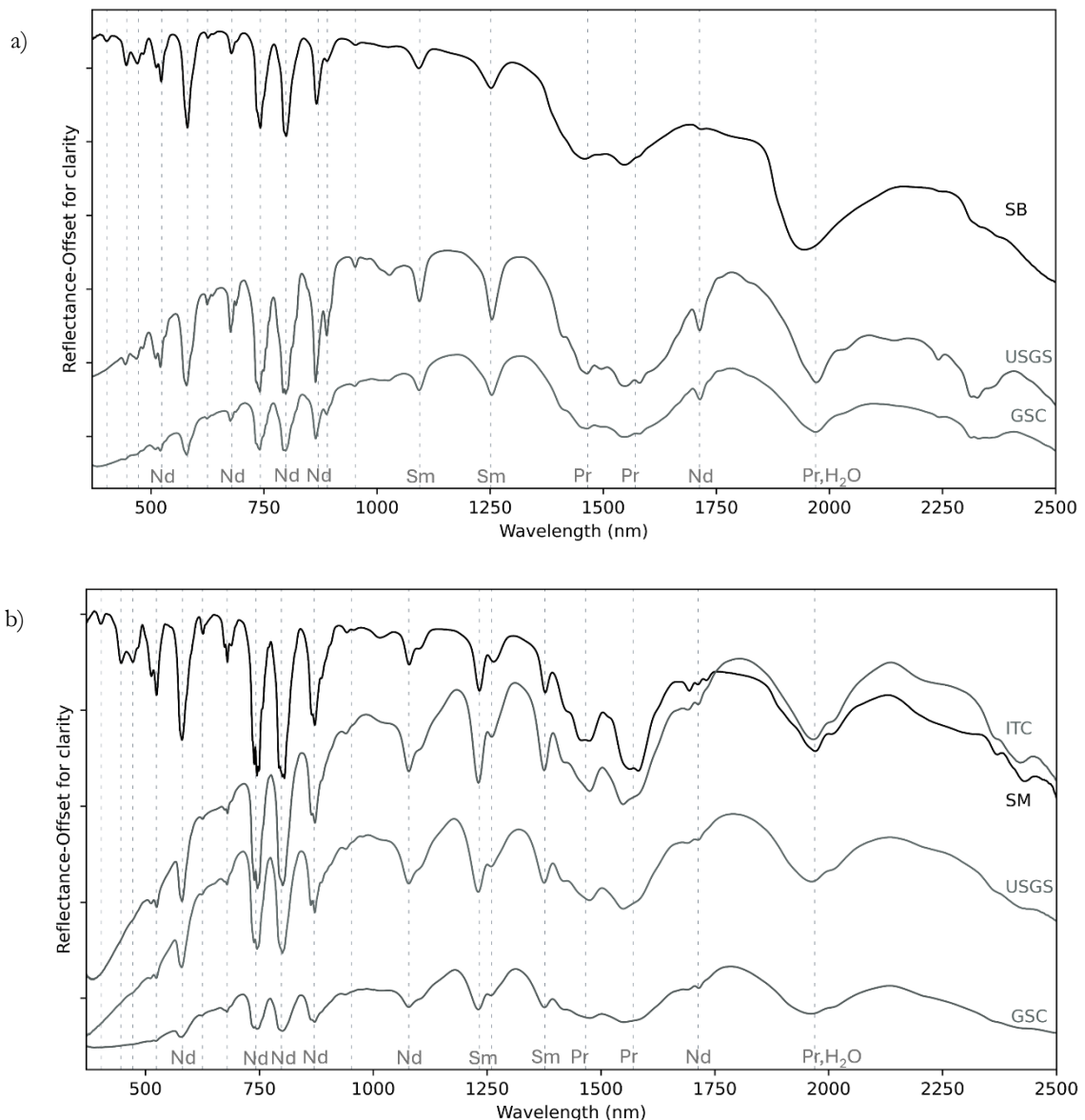


Figure 3.1: Diffractograms of the synthesised materials with comparison to stick diagrams of crystallographic reference data monazite (mnz-syn), synthesised rhabdophane (rhabdo-syn), natural monazite from ITC collection (mnz-ITC). Note the similarity of the peak positions of the synthetic monazite to those in the natural monazite but also the different relative peak intensities and the low-intensities of the peaks at 2 theta angles greater than 40° for the natural monazite. Diffractogram of synthetic bastnäsite with reference data. Note that the peak positions overlap with reference data.

### 3.2. Spectral data analysis of synthesised minerals

#### 3.2.1. Comparison of synthesised minerals with published spectral libraries

The comparison of the synthetic monazite and bastnäsite spectra with the spectra of natural minerals at ITC mineral collection and recently published spectral libraries by Percival et al. (2019) and Kokaly et al. (2017) is shown in Figure 3.2. The spectra of synthetic minerals show a high degree of similarity to those of the natural ones in terms of the wavelength positions and relative depth of the absorption features. The albedos of the off-white-coloured synthetic minerals are higher than the natural minerals spectra. Further, the gradual drop in reflectance from 1000 nm towards the ultraviolet region in natural monazite and bastnäsite is absent in the off-white-coloured synthetic mineral spectra due to the differences in visible light of the brown-coloured natural minerals. However, a gradual albedo drop is observed after 1200 nm towards longer wavelengths in bastnäsite spectra, which is not present in natural bastnäsite spectra. Further, the Pr<sup>3+</sup> absorption feature around 1580 nm in published library spectra is broader and more detailed than the synthesised bastnäsite, while the Pr, H<sub>2</sub>O feature is deeper in synthetic bastnäsite.





*Figure 3.2:* Comparison of reflectance spectra of the synthesised minerals with the spectra of natural minerals from published spectral libraries, USGS: published spectra from Kokaly et al. (2017) (USGS v7 spectral library, GCS: published spectral library from Percival et al. (2019) (The National Mineral Reference Collection (NMC) Digital Spectral (VIS-NIR-SWIR) Library, Part II: REE-Nb-U-Th-bearing minerals by Geological Survey of Canada) ITC: spectra of brown coloured natural monazite powder from ITC mineral collection; a) Comparison of monazite spectra, SM: off white coloured synthetic monazite; b) comparison of bastnäsite spectra, SB: synthetic bastnäsite-off white colour; Note that for both synthetic minerals albedos difference and the gradual drop of visible region in natural minerals and absence of well-defined multiplets in Nd absorption features of synthetic bastnäsite in near-infrared region.

### 3.2.2. Comparison of synthetic bastnäsite and monazite

A comparison of wavelength positions of main absorption features in synthesised monazite and bastnäsite with each other and recently published data on natural monazite and bastnäsite by Turner et al. (2014, 2016) is presented in Table 3.1. According to the comparison, the wavelength positions of synthetic minerals agree well with that of natural mineral data.

In comparing synthetic monazite and bastnäsite, several differences in their spectral features have been observed (see Figure 3.3). Notably, some features in monazite are shifted by 5 to 10 nm towards shorter wavelengths compared to bastnäsite. Additionally, certain features in monazite appear as single absorption peaks rather than having shoulders.

For example, the Nd<sup>3+</sup> feature at 942 nm and the Sm<sup>3+</sup> feature at 1079 nm in monazite are shifted to shorter wavelengths relative to their positions in bastnäsite. In monazite, the Nd<sup>3+</sup> feature at 680 nm, which has shoulders at 673 nm and 689 nm, appears as one distinct feature in bastnäsite at 678 nm with a shoulder at 690 nm with the absence of relative feature at 673 nm. Furthermore, the Sm<sup>3+</sup> features in monazite at 1079 and 1105 nm appear as a single absorption feature at 1093 nm in bastnäsite. Similarly, the Sm<sup>3+</sup> features in monazite at 1233 and 1264 nm also appear as a single feature at 1252 nm in bastnäsite. Additionally, the Nd<sup>3+</sup> feature at 958 nm and the Sm<sup>3+</sup> feature at 1377 nm, present in monazite, is not observed in bastnäsite.

According to Dijkstra et al. (2024), the multiplets of Nd<sup>3+</sup> absorption features occur due to the crystal field splitting effect. Well-defined sharp multiplets of Nd<sup>3+</sup> features between 700 and 850 nm in synthesised monazite are not observed in synthesised bastnäsite. In contrast, these features in monazite are also recognisable in published spectra by Kokaly et al. (2017) and Percival et al. (2019). Similarly, Pr<sup>3+</sup> features in monazite at 1472 nm and 1580 nm exhibit multiplets due to the crystal field, while the corresponding Pr feature in bastnäsite is observed as a broader feature without sharp multiplets.

*Table 3.1:* The comparison of absorption feature positions of synthetic monazite and bastnäsite of the current with recently published data for monazite and bastnäsite from Turner et al. 2014 and 2016

Probable origin	Monazite		Bastnäsite	
	Turner et al. 2014	Synthetic	Synthetic	Turner et al. 2016
Sm <sup>3+</sup>	-	401	401	-
Nd <sup>3+</sup>	-	447	447	-
	-	472	472	-
Nd <sup>3+</sup>	-	513	512	511
	-	524	523	523
	-	-	<b>533 SH, w</b>	533
Nd <sup>3+</sup>	575 SH	575 SH	575 SH	575 SH
	580	580	581	580
Nd <sup>3+</sup>	625	627	627	625



			639	636
<b>Nd<sup>3+</sup></b>	673	<b>673</b>	-	676
	679	<b>680</b>	<b>678</b>	689
	689	<b>689</b>	<b>690 SH</b>	693 SH
<b>Nd<sup>3+</sup></b>	734 SH	734 SH		
	738	738		
	745	745	734 SH	734 SH
	749 SH	749	742	741
	757 SH	757 SH	749 SH	749
	770 SH	771 SH		
<b>Nd<sup>3+</sup></b>	792	793		
	800	801	794	792
	804	805	799	797
	814 SH	814 SH		
	830 SH	830 SH		
<b>Nd<sup>3+</sup></b>	863	865	866	864
	871	872	-	871
	887	887	891	-
	896 SH	896 SH	-	898
	907	906 SH		
<b>Nd<sup>3+</sup></b>	941	<b>942</b>	<b>953</b>	953
	957	<b>958</b>	-	978
<b>Sm<sup>3+</sup></b>	1023	1016	1023 w	1023
	1074	<b>1079</b>	<b>1093</b>	1093
	1105	<b>1105</b>	-	-
<b>Sm<sup>3+</sup></b>	1232	<b>1233</b>	-	1225
	1257	<b>1264</b>	<b>1252</b>	1251
				1314
<b>Sm<sup>3+</sup></b>	1377	<b>1377</b>	-	-
<b>Pr<sup>3+</sup></b>	1452	1455		
	1471	1474	1456	1465
	-	1559	1548	1547
	1578	1581		
<b>Nd<sup>3+</sup></b>	1691	1694		
	1710	1714	1717	1710
	1717	1732		
	1735			
<b>Pr<sup>3+</sup>, Sm<sup>3+</sup>, H<sub>2</sub>O</b>	1968	1970		
<b>Pr<sup>3+</sup>, Sm<sup>3+</sup></b>	2011	2011		
<b>CO<sub>3</sub><sup>2-</sup></b>	-	-	2243 w	2243
<b>REE/OH/PO<sub>4</sub></b>	2368	2367		
	2424	2428		

Note: Bold values indicate major wavelength shifts; SH- shoulder; w-weak feature

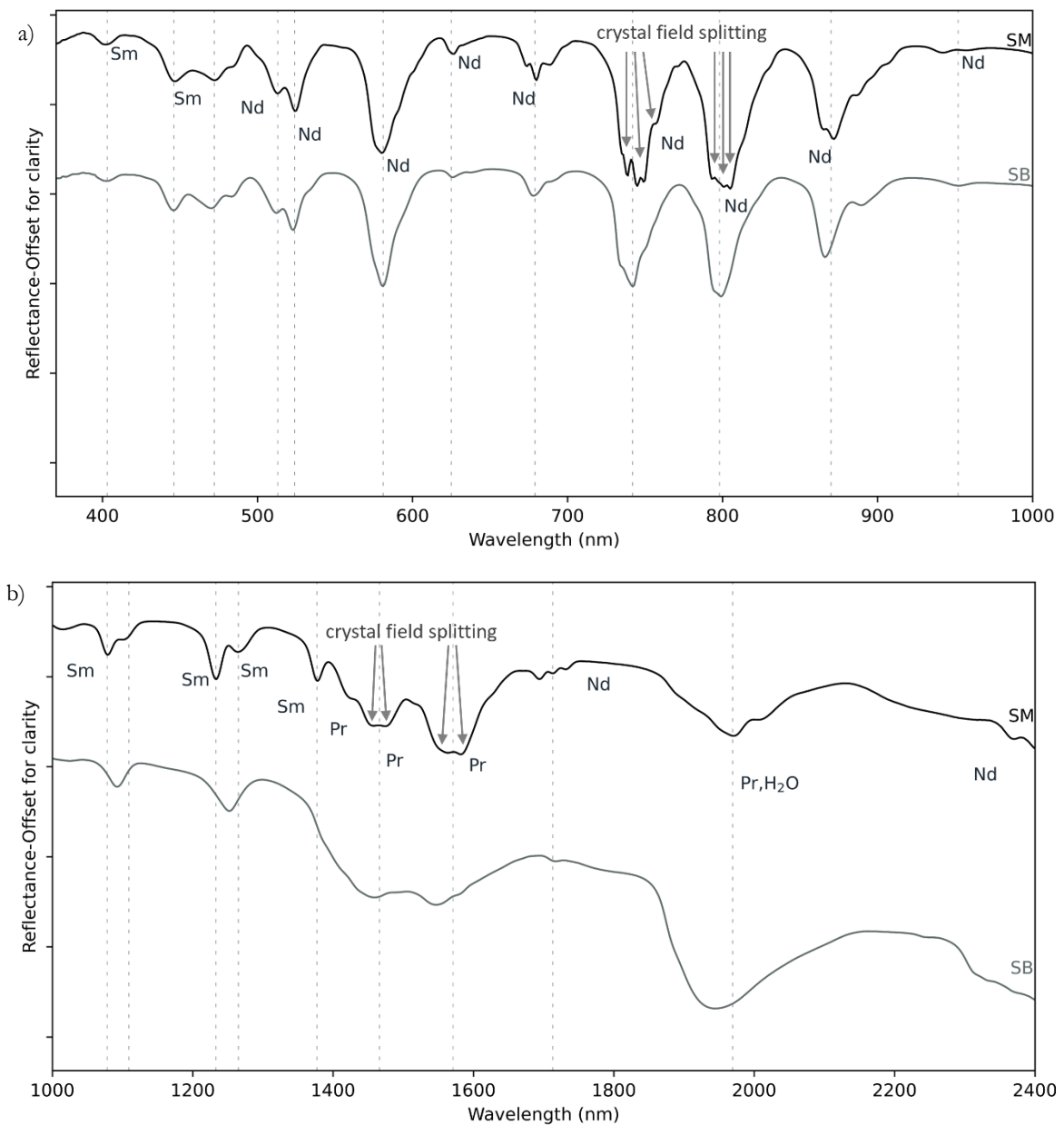


Figure 3.3: Comparison of synthetic monazite and bastnäsite with each other. Dashed lines mark the centres of some prominent absorption features observed in synthetic monazite. a) reflectance spectra comparison of VNIR range. b) reflectance spectra comparison in SWIR region; note the absence of crystal field splitting effect of major Nd and Pr features in bastnäsite compared to monazite and some Nd<sup>3+</sup>, Sm<sup>3+</sup> corresponding absorptions in the synthetic monazite occur at ~5-10 nm shorter wavelengths.

### 3.3. Sub objective one- Understanding the behaviour of spectra of the mineral mixtures.

The VNIR and SWIR reflectance spectra of monazite and bastnäsite mixtures after averaging the six measurements are shown in Figure 3.4. The low standard deviation of the six replicate measurements per sample confirms satisfactory homogeneously mixed samples.

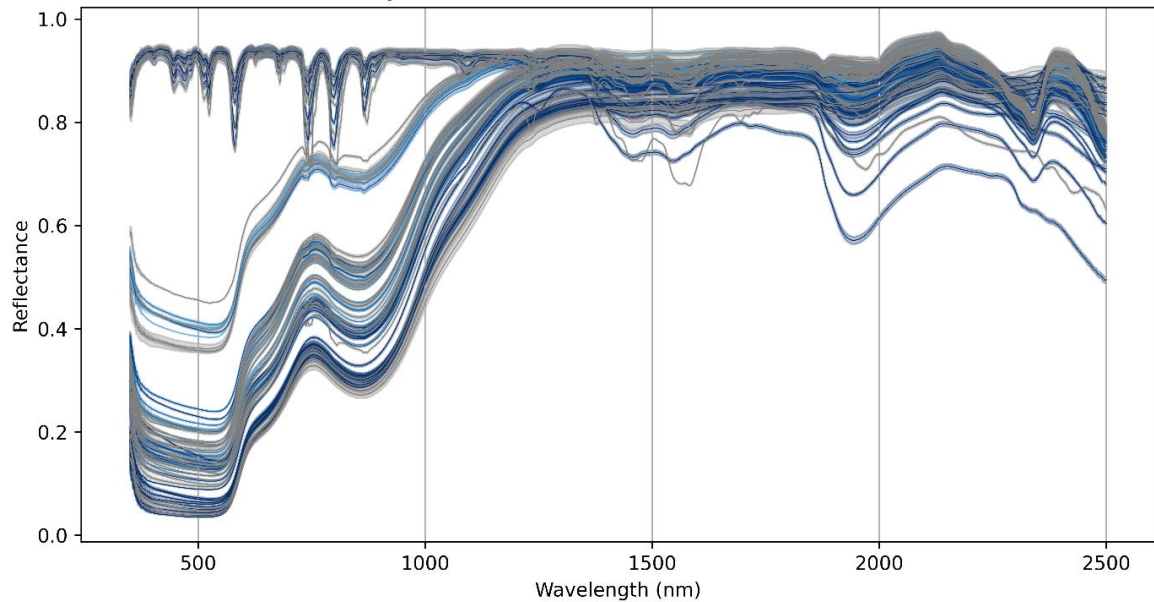


Figure 3.4: Reflectance spectra for monazite or bastnäsite with calcite and hematite, normalised to a maximum reflectance value of 1 with shaded area indicating the standard deviation of the replicates measurements for each sample, in blue: Reflectance spectra of bastnäsite mineral mixtures, in grey: Reflectance spectra of monazite mineral mixtures.

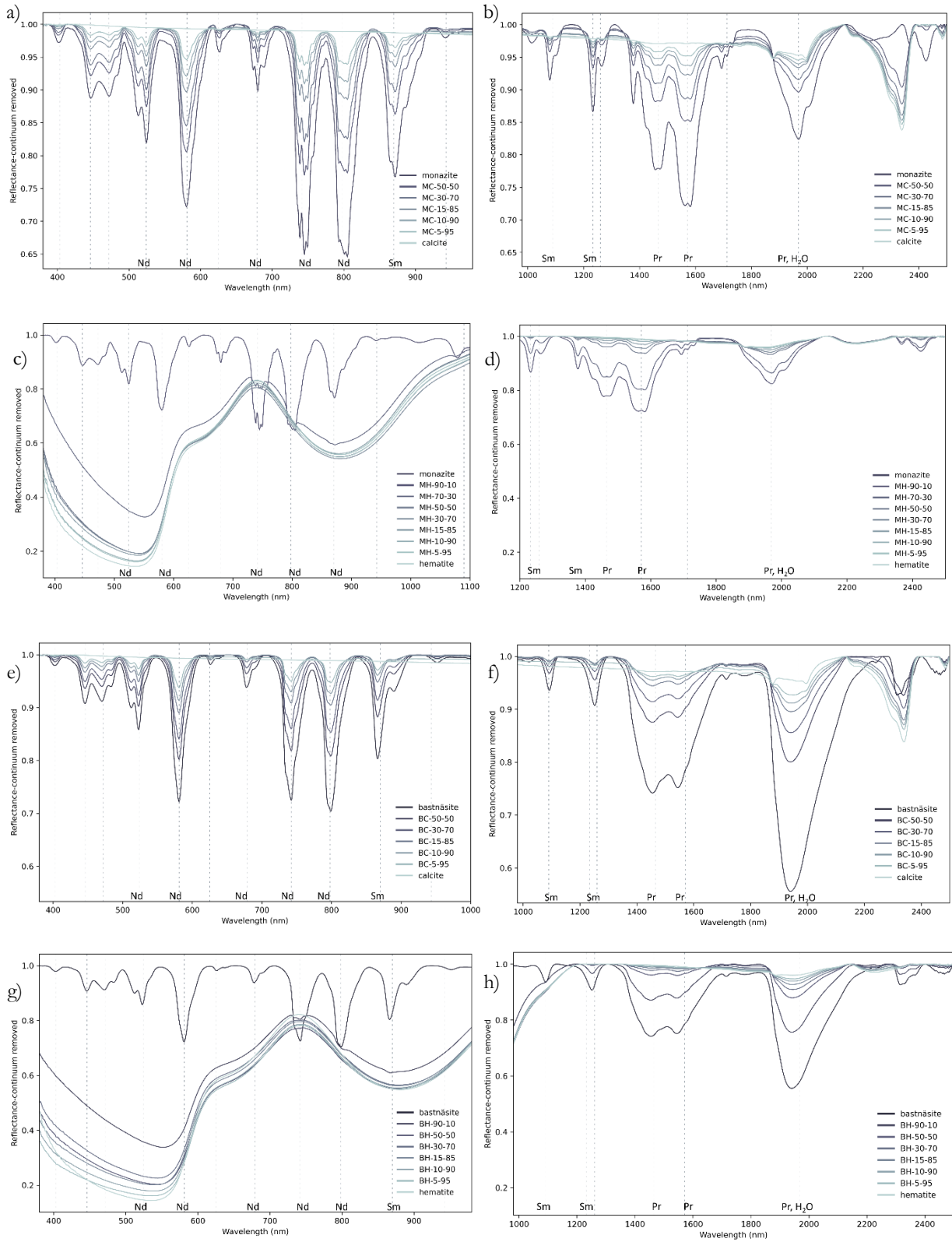
### 3.3.1. Simple mixtures

The absorption feature parameters defined in section 2.3.2, i.e. absorption feature wavelength position between 700-1200 nm in hematite mixed spectra and absorption feature depths across the whole range, were analysed for monazite-calcite, monazite-hematite, and hematite-calcite simple mixtures.

In hematite-calcite mixtures, the wavelength position of the absorption feature between 700 and 1200 nm remains stable despite varying modal abundances, with only minor shifts. However, the changes in the depth of this absorption feature do not change after 50 wt% hematite (Figure 3.5 i-j).

Considering monazite-hematite simple mixtures, in a 95 wt% monazite and 5 wt% hematite mixture,  $\text{Nd}^{3+}$  features at 742, 805, and 872 nm are visible. Similar to hematite-calcite features, significant depth changes are not observed in mixtures with more than 50 wt% hematite in the VNIR range. However, in a 50 wt% monazite and 50 wt% hematite mixture, no REE features are detectable in the VNIR range (Figure 3.5, c-d), though changes in the depth of REE features in the SWIR region remain evident.

For calcite-monazite mixtures, evident changes in feature depth are observed with increasing calcite content in both the VNIR and SWIR ranges. However, some bastnäsite simple mixtures do not behave exactly like monazite mixtures. The VNIR spectra of the bastnäsite mixtures lack the strong features present in monazite-hematite simple mixtures. In contrast, calcite-bastnäsite mixtures exhibit the same gradual changes observed in monazite mixtures (Figure 3.5 g-h).



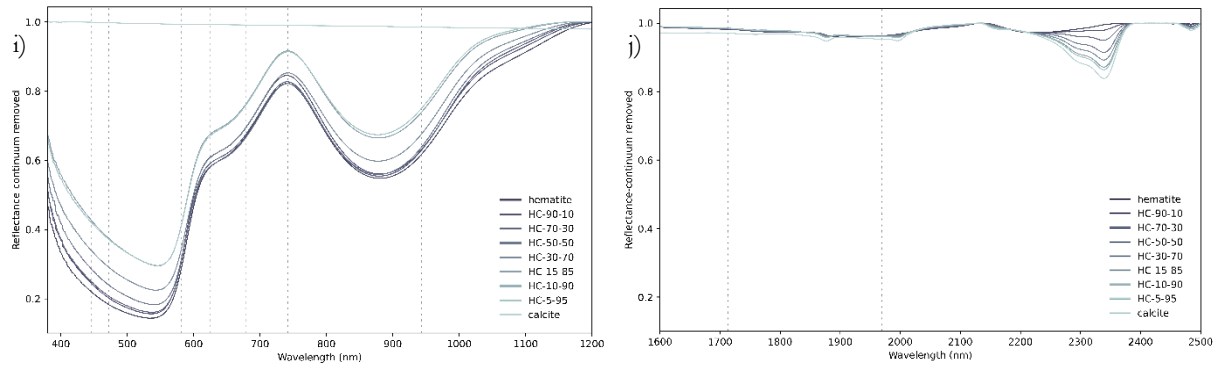


Figure 3.5: The behaviour of reflectance spectra of simple mineral mixtures, dashed lines correspond to the wavelength positions of prominent REE absorption features. Notation: MH-50-50 represents 50 wt% of monazite 50 wt% hematite in the mineral mixture, M-monazite, B- bastnäsité C- calcite, H-hematite. Note the gradual change of depths in VNIR and SWIR for calcite-REE mineral mixtures and in SWIR hematite-REE mineral mixture. a) calcite-monazite mixture in VNIR. b) calcite-monazite mixture in SWIR. c) hematite-monazite mixture in VNIR. d) hematite-monazite mixture in SWIR. e) bastnäsité-calcite simple mixtures in VNIR. f) bastnäsité-calcite simple mixtures in VNIR. g) bastnäsité-hematite simple mixtures in VNIR, h) bastnäsité-hematite simple mixtures in SWIR. i) calcite-hematite mixtures in VNIR. j) calcite-hematite mixtures in SWIR.

### 3.3.2. Complex mixtures

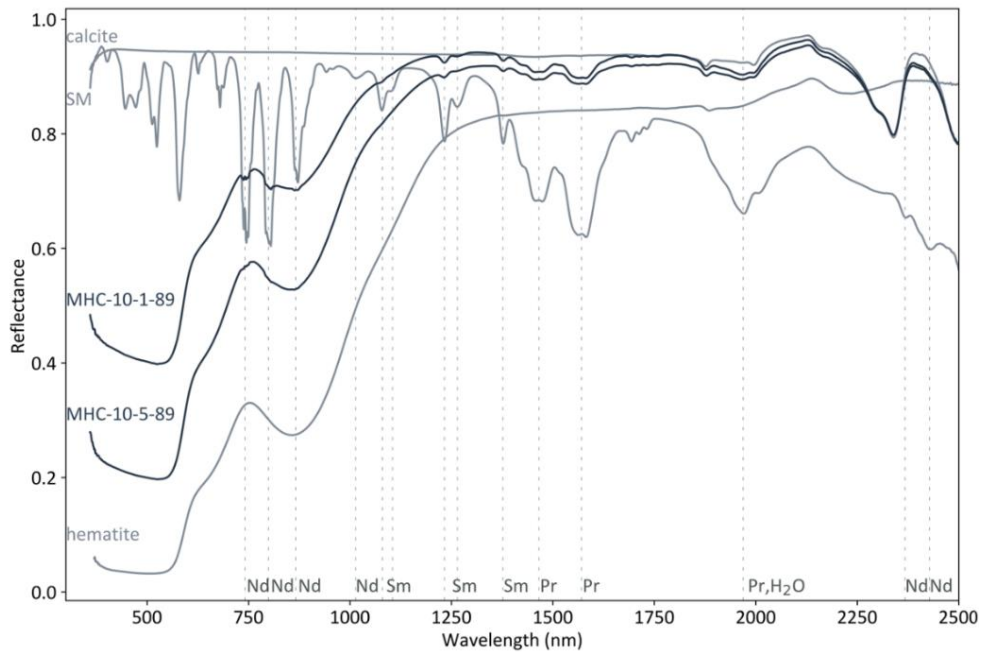


Figure 3.6: comparison of the spectra of 10 wt% monazite complex mixture with its end members highlighting the REE features still preserved in the spectra, notation MHC-10-1-89 represents 10 wt% of monazite 1 wt% hematite 89 wt% of calcite indicating the modal abundance of the mineral mixture, M-monazite, C- calcite, H-hematite, SM-synthetic monazite; note the REE ion absorption features in VNIR are either diluted or disappeared while Sm, Pr features are still preserved in the spectra of complex mixtures, dashed lines mark the centre of the absorption features

Figure 3.6 shows an example of a complex mineral mixture of monazite with varying hematite and calcite modal abundances. The overall shapes of the reflectance spectra of complex mixtures follow the shape of hematite in the VNIR range, even in the case of a mixture with only 1 wt% of hematite. The  $\text{Sm}^{3+}$  feature at 401 nm and  $\text{Nd}^{3+}$  features at 472, 524, and 580 nm disappear even with 1 wt% of hematite in complex mineral mixtures of monazite calcite and hematite. However,  $\text{Nd}^{3+}$  features at 745, 805, and 872 nm are still

visible in spectra of complex mineral mixtures with a high degree of changes in depth. A very weak  $\text{Sm}^{3+}$  feature at 1079 nm is present in samples with high monazite abundance.

Figure 3.7 illustrates the comparison of REE mineral-hematite-calcite mineral mixtures with each other. In mixtures containing 10 wt% bastnäsite, even adding 1 wt% hematite  $\text{Sm}^{3+}$  feature at 401,  $\text{Nd}^{3+}$  features at 472, 524, and 580 nm disappear, which is also observed in monazite mixtures. Compared to monazite mixtures,  $\text{Nd}^{3+}$  and  $\text{Sm}$  absorptions in bastnäsite mixtures are less distinct (see Figure 3.7). The  $\text{Pr}$  feature is diluted but visible in 10 wt% monazite complex mixtures with varying hematite and calcite percentages, while it becomes flat even with 5 wt% hematite in a 10 wt% bastnäsite mixture. Notably, the  $\text{Pr-H}_2\text{O}$  feature is still visible with reduced depth in bastnäsite mixtures but is undetectable in monazite mixtures. Given the sharp features in monazite mixtures, further qualitative analyses were conducted on monazite mixtures.

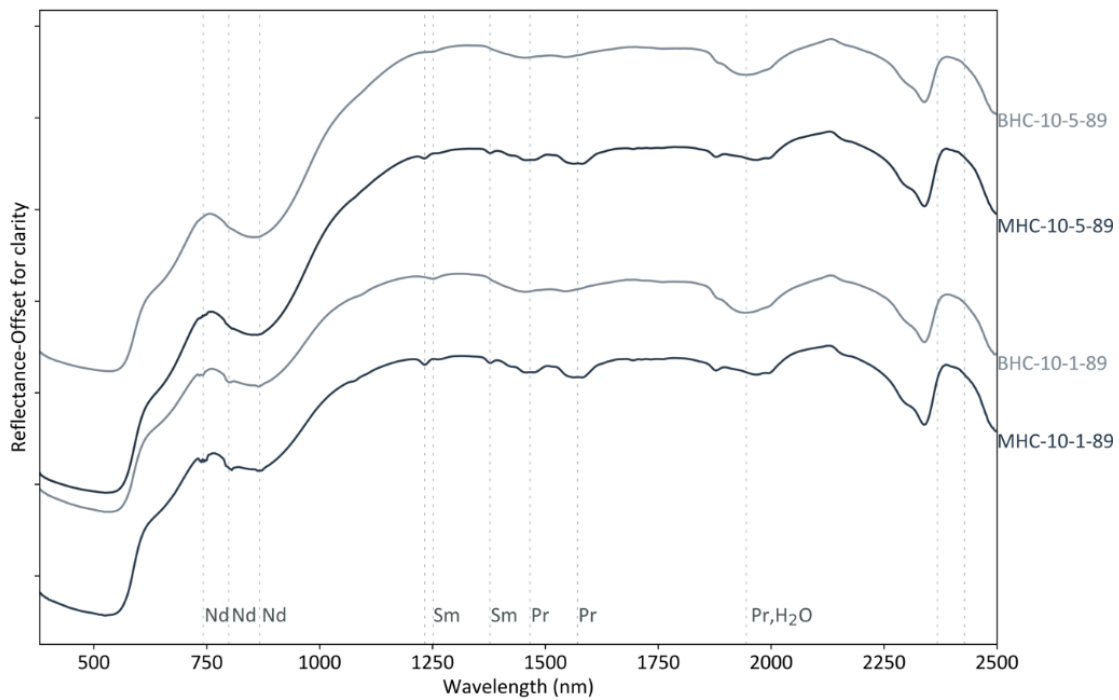


Figure 3.7: Comparison of monazite and bastnäsite complex mixtures, in grey: bastnäsite complex mixtures, in black: monazite complex mixtures, notation: MHC-10-1-89 representing 10 wt% monazites, 1 wt% hematite and 89 wt% calcite, M-monazite, C- calcite, H-hematite, B-bastnäsite; note that with the similar weight percentages preserved REE absorption features are sharper in monazite mixtures than that of bastnäsite, dashed lines mark the centre of the absorption features.

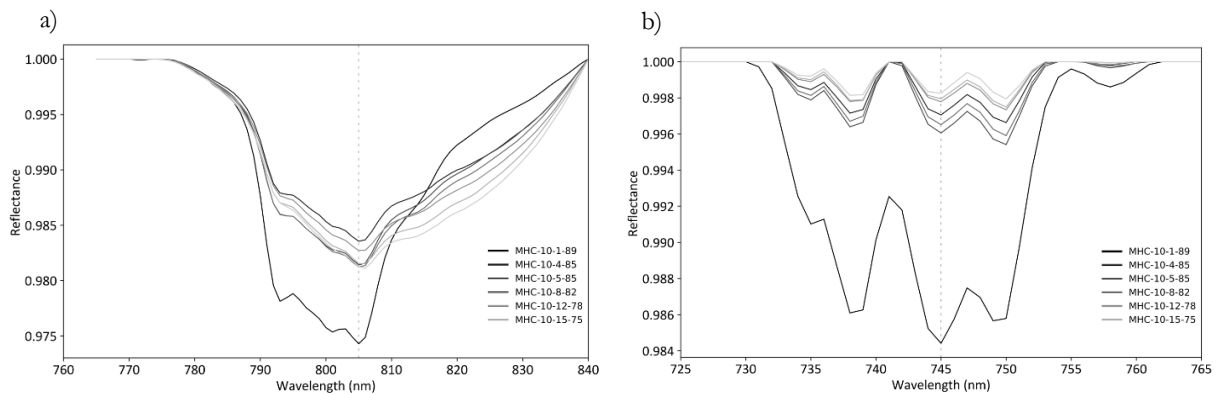


Figure 3.8: Figures showing REE features in VNIR range; notation: MHC-10-1-89 representing 10 wt% monazite, 1 wt% hematite and 89 wt% calcite, M-monazite, C- calcite, H-hematite; left: continuum removed spectra between 760-840 nm highlighting  $\text{Nd}^{3+}$  feature depths in complex mixtures; right: continuum removed spectra between 730-760 nm highlighting  $\text{Nd}^{3+}$  feature depths in complex mixtures, note that the depth changes are below 0.1% of reflectance values and the significant depth change and smoothing of features after 4% hematite

The behaviour of Nd features in monazite complex mixtures between 730-760 nm and 760-840 nm ranges are illustrated in Figure 3.8. The change in depth is less than 0.1% of reflectance; however, when hematite exceeds 4%, the depth change becomes negligible. Similar observations were made for the 805 nm multiplets. Due to these minimal reflectance changes, using these features as diagnostic indicators for hematite mixed REE spectra is considered unreliable.

A detailed qualitative analysis of the feature depth and position of 872 nm  $\text{Nd}^{3+}$  features in monazite complex mixtures is shown in Figure 3.9. The absorption feature depth changes and absorption feature position change with changing hematite do not show a relationship. Therefore, using VNIR range absorption features as diagnostic features for hematite mixed spectra is unreliable.

In the SWIR range, the depth of absorption features in complex mixtures exhibits a clear relationship with varying mineral abundances reflecting the behaviour of spectra of simple mixtures in the SWIR region (See Figure 3.10). Statistical analyses to understand the behaviour of the newly defined band ratio (PrR) behaviour for monazite mixtures (equation 2.4; Figure 2.5) with varying mineral abundances are shown in Figure 3.10.

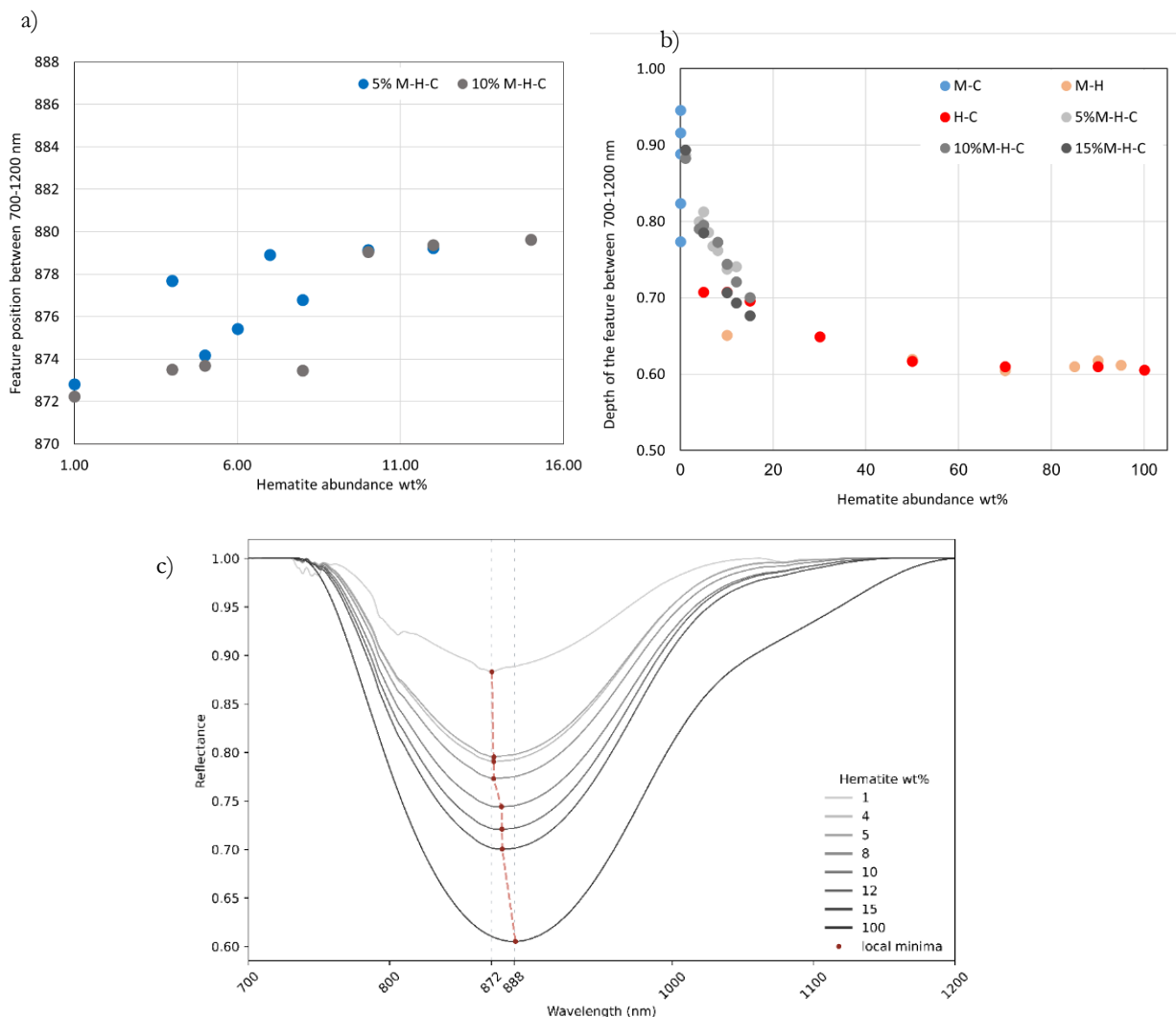




Figure 3.9: Scatterplots showing the changes of absorption parameters centred between 700-1200 nm; a) feature position change with increasing hematite, dark blue-10 wt% monazite complex mixtures, grey- complex mixtures containing 10 wt% monazite, blue – complex mixtures containing 5 wt% monazite, note that the changes do not show a relationship with hematite. b) feature depth changes in mixtures, black: hematite-monazite-calcite complex mixtures with 15% monazite, dark grey: hematite-monazite-calcite complex mixtures with 10% monazite, light: hematite-monazite-calcite complex mixtures with 5% monazite, blue: monazite calcite simple mixtures, red: hematite calcite simple mixtures, yellow: hematite monazite simple mixtures, note that with high changes of hematite the feature depth does not change while hematite percentage below 15 depth is changing with increasing hematite. c) figure showing the wavelength position change in 10 wt% monazite complex mixtures

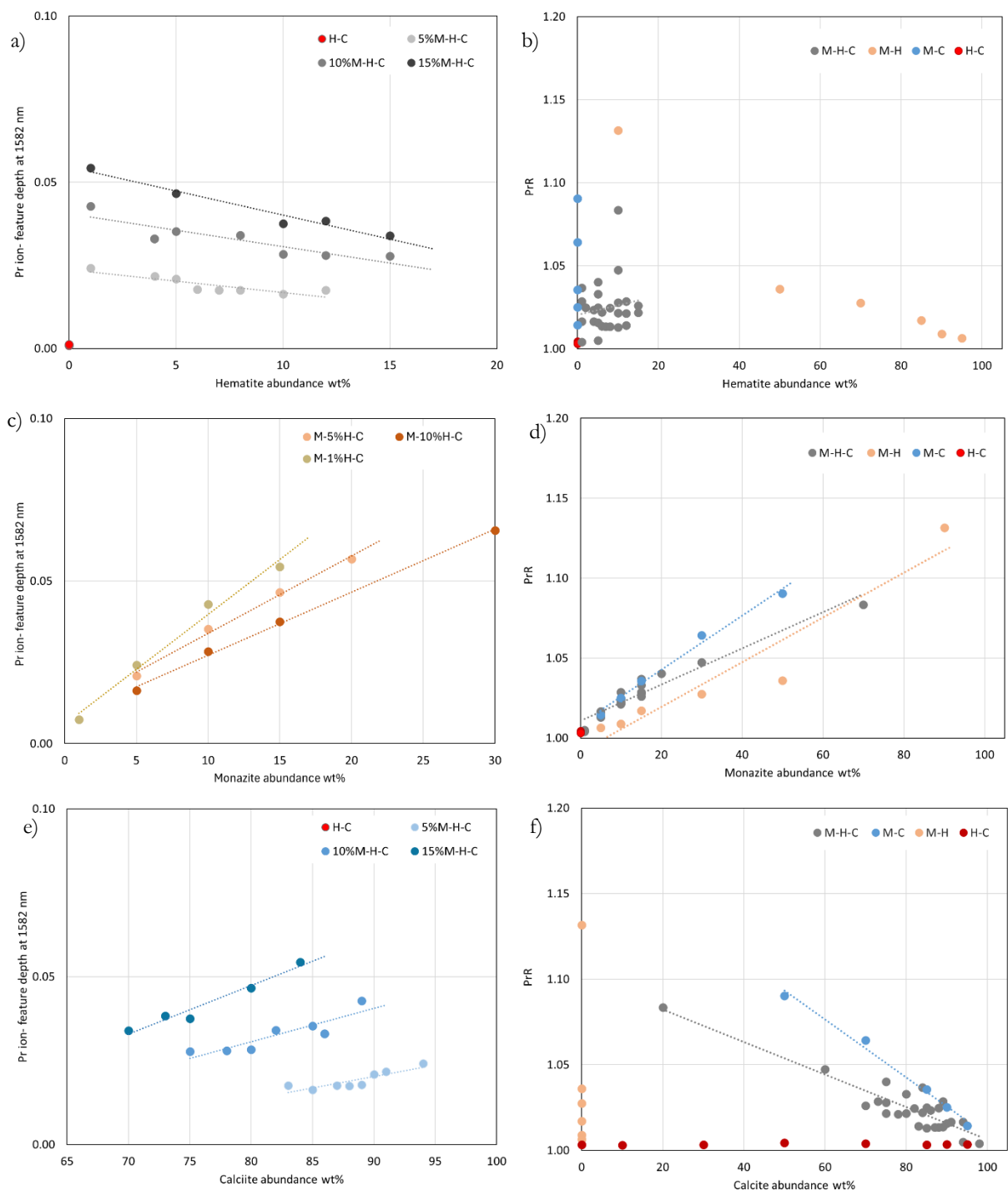


Figure 3.10: a) Scatter plot showing the relationship of the Pr feature depth and hematite percentage in monazite 5 wt%, 10wt% 15wt% complex mixtures. Note that hematite calcite mixtures do not have a feature in the considered



wavelength position. b) Scatterplots show the relationship of the newly defined PrR with hematite abundance in complex and simple mixtures. c) Scatter plot showing the relationship of the Pr feature depth and monazite percentage in hematite 5 wt%, 10wt% 15wt% complex mixtures. d) scatter plot showing the relationship of the PrR with increasing monazite percentage in different mixtures. e) Scatter plot showing the relationship of the Pr feature depth and calcite percentage in monazite 5 wt%, 10wt% 15wt% complex mixtures. f) Scatter plot showing the variation of the PrR with increasing calcite percentage in different mixtures. Labelling: 5%M-H-C- represent 5 wt% monazite mixture with varying calcite and hematite abundances, M-monazite, C-calcite, H- hematite

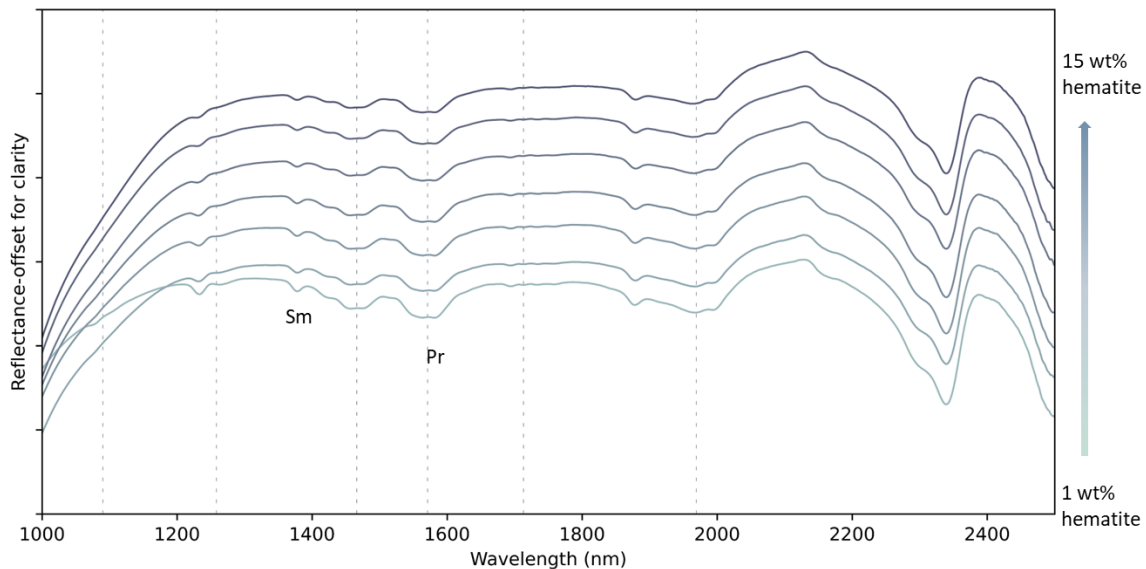


Figure 3.11: Reflectance spectra of 10% monazite complex mixtures with varying hematite abundance. Light grey: 1wt% hematite in 10% wt monazite complex mixture, dark grey 15 wt% hematite in 10 wt% monazite complex mixture

### 3.4. Sub objective two – Detecting REEs with hyperspectral sensors

Laboratory resampled spectra for hyperspectral airborne (AVIRIS) and hyperspectral spaceborne (EnMap) sensors are shown in Figure 3.12. In the resampled spectra for the AVIRIS sensor, Nd-related absorption features between 700 and 800 nm are still visible in 1% wt hematite present 10 wt% monazite complex mixtures, but their depth is significantly reduced, appearing as minor wiggles. Despite this, the Pr features in the SWIR domain remain visible (see Figure 3.12), similar to those in high-resolution laboratory spectra. These observations are consistent with the data resampled to the instrument specifications of the EnMAP sensor, where the Pr feature is also clearly distinct in the resampled spectra (Figure 3.12). The absorption feature behaviour of the Pr feature in SWIR remains recognisable, suggesting that the Pr band ratio can detect the presence of Pr in mineral mixtures using hyperspectral sensors.

Therefore, the PrR defined in section 2.3.2 (equation 2.4; Figure 2.5) can be re-adjusted for AVIRIS hyperspectral airborne and EnMap hyperspectral spaceborne sensors avoiding atmospheric absorption (equations 3.1 and 3.2). The PrR<sub>AVIRIS</sub> with hematite abundance is attached in Appendix 15.

$$Praseodymium\ Ratio\ (PrR)_{AVIRIS} = \frac{[B122:B123].mean() + [B137:B139].mean()}{[B127:B129].mean()}$$

3.1

$$Praseodymium\ Ratio\ (PrR)_{EnMap} = \frac{[B140:B141].mean() + [B154:B156].mean()}{[B145:B147].mean()}$$

3.2

### 3.5. Sub objective three – Detecting REEs with multispectral sensors

Figure 3.13 shows the laboratory-derived spectrum resampled to the instrument specifications of the multispectral (super spectral) sensors, WordView-3 and Landsat Next. It can be seen in this figure that the WordView-3 SWIR2 band can detect the Pr feature around 1580 nm, and hematite does not affect this band similarly to hyperspectral sensors. The band ratio proposed earlier for detecting Pr in high-resolution spectra (equation 2.4; Figure 2.5) can be modified for the multispectral WordView-3 sensor, for instance, by taking a band ratio of SWIR3/ SWIR2. Although the depth change is not very significant, it is evident in continuum-removed spectra. (Figure 3.14)

However, based on the laboratory resampled spectra for Landsat Next sensor specifications, it seems unlikely to detect REE absorption features in hematite-mixed environments with designed sensor specifications.

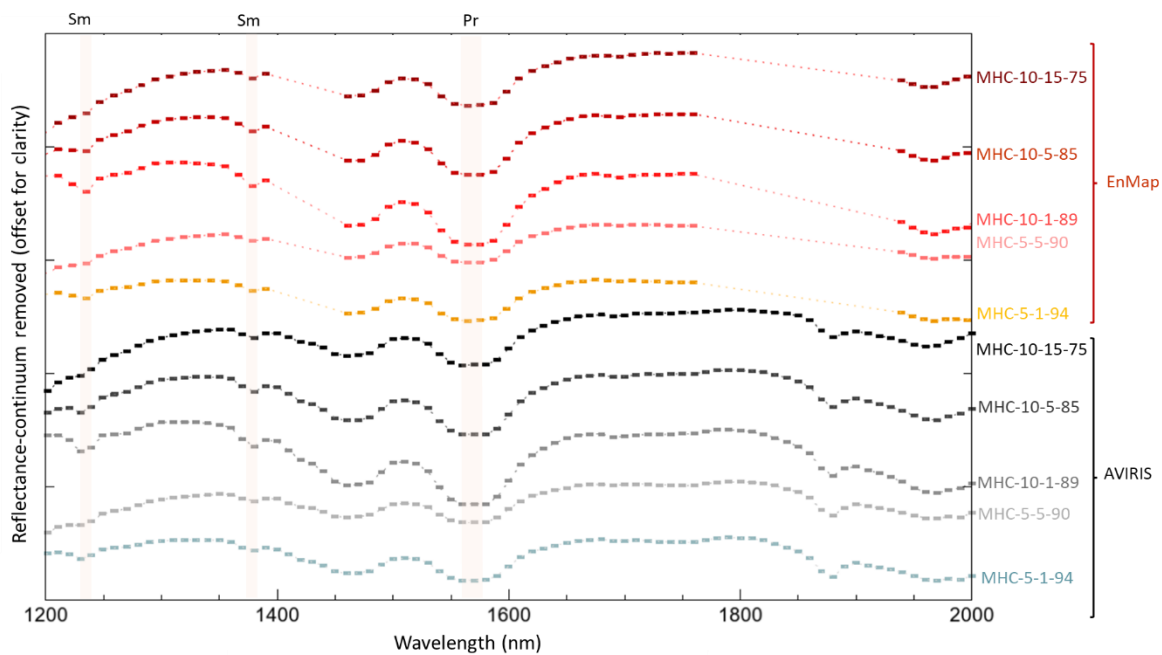


Figure 3.12: Laboratory resampled spectra for AVIRIS and EnMap hyperspectral sensors to assess the capability of discriminating Pr feature from 10 wt% monazite, varying calcite and hematite spectra. Note that the broad Pr feature centred at 1572 nm is well preserved in both the sensors.

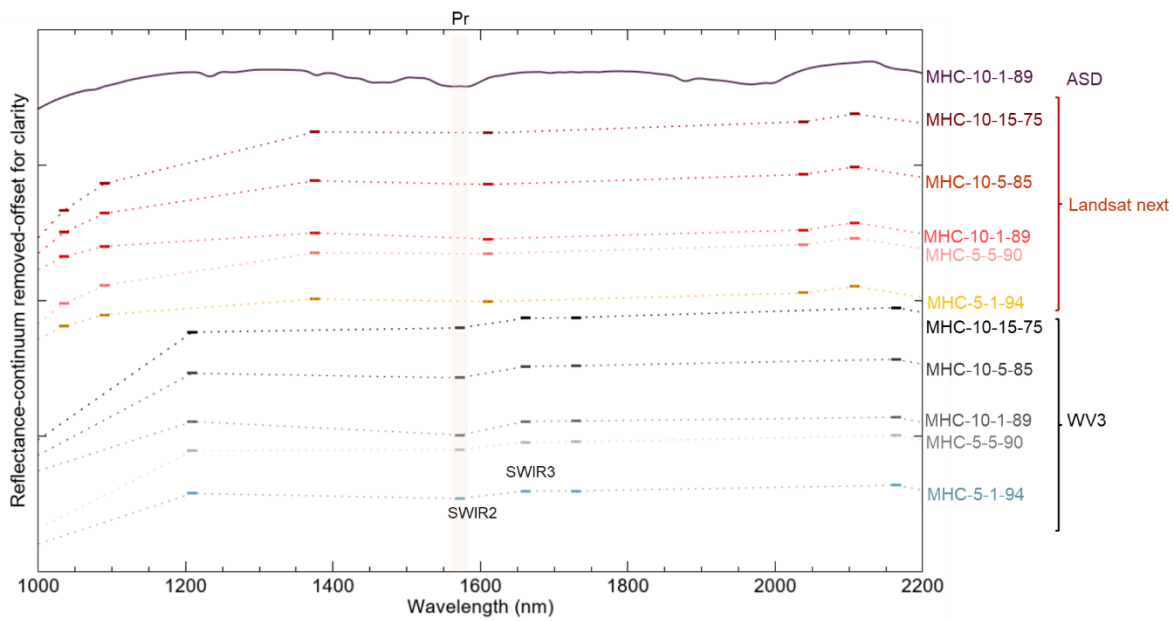


Figure 3.13: Laboratory resampled spectra for multispectral sensors, WV3- Worldview 3 super spectral sensor, LSN-Landsat Next super spectral sensor spectra to assess the capability of discriminating Pr feature from 10 wt% monazite, varying calcite and hematite spectra. Note that the broad Pr feature centred at 1580 nm is preserved in the resampled spectra of the WorldView 3 sensor.

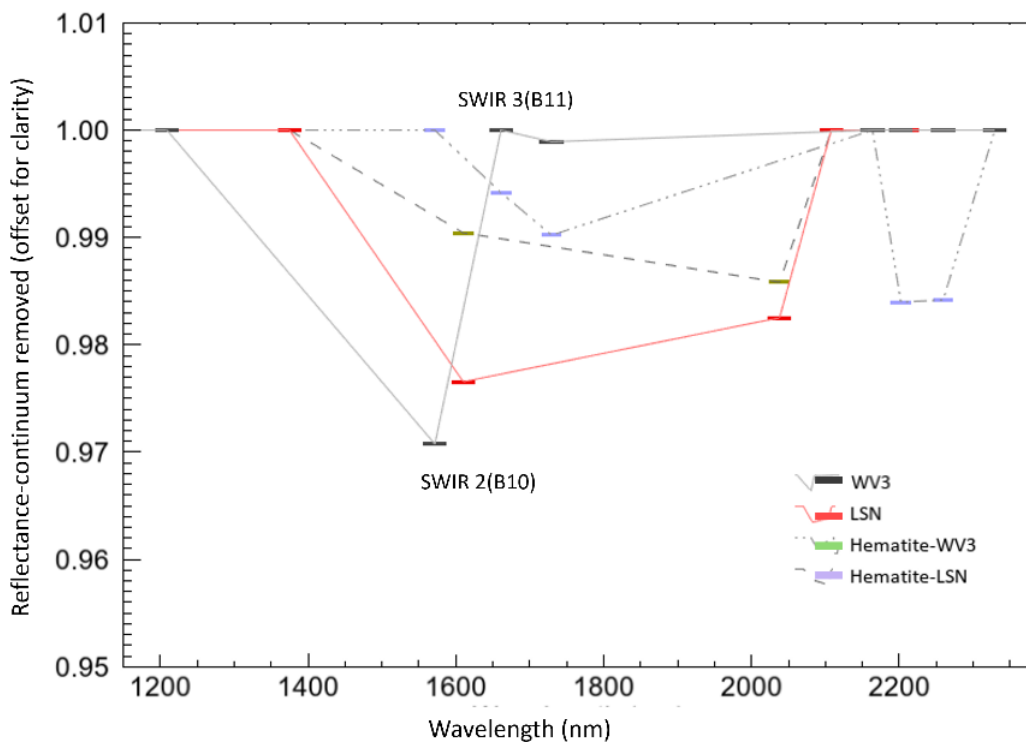


Figure 3.14: Laboratory resampled spectra for WorldView 3 and Landsat Next multispectral sensors to assess the capability of discriminating Pr feature from 10 wt% monazite, 5 wt% hematite 85 wt% calcite sample; note that broad Pr feature centred at 1580 is detectable in WorldView 3 sensor. WV3-WorldView 3, LSN-Landsat Next. Note that the band centred at 1600 nm in the Landsat Next sensor has gradual drops from both adjacent bands for both monazite mixed spectra and hematite spectra.

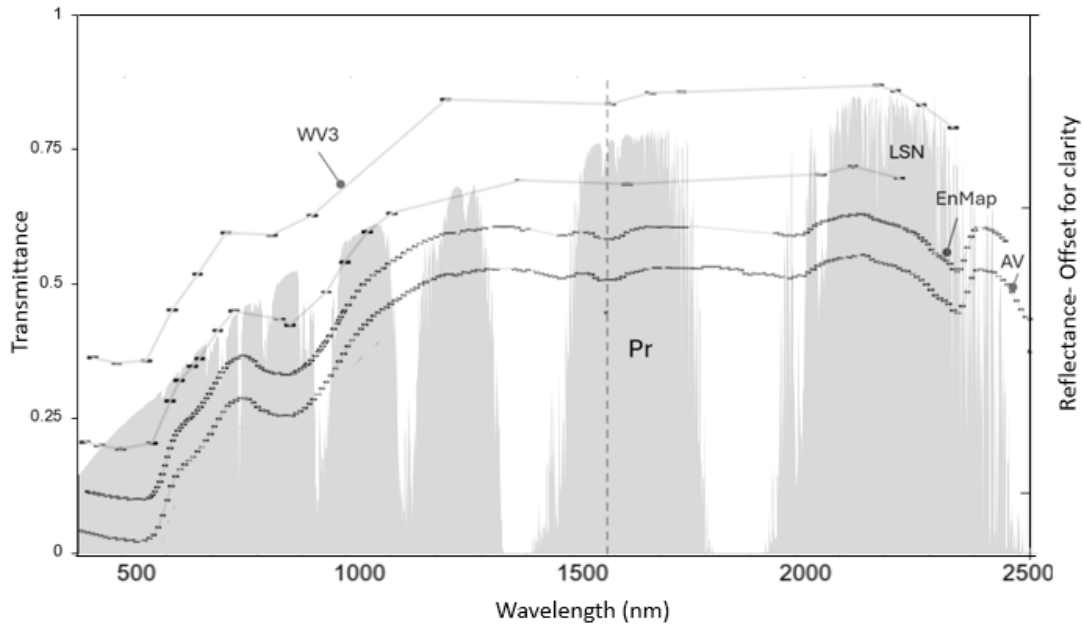


Figure 3.15: Comparison of resampled spectra with atmospheric absorption bands of the VNIR and SWIR range. Note that the Pr feature falls within the atmospheric window. WV3-WorldView 3, LSN-Landsat Next, AV- AVIRIS.

## 4. DISCUSSION

### 4.1. Mineral synthesis

The XRD results of synthesised minerals confirm monazite and bastnäsite (Figure 3.1). The diffractograms agree well with the general monazite and bastnäsite data from crystallographic libraries. The comparison of absorption features of the synthesised materials with the single REE spectra published by Dijkstra et al. (2024) confirms the presence of La, Nd, Sm, and Pr in the synthesised products. The reflectance spectra of synthesised minerals are very similar to published library spectra of natural REE minerals, further indicating the presence of REE in the products. Therefore, the synthesised final product can be considered successful in terms of the desired REE in the mineral.

Questions remain about the exact molar proportions of the REE in the synthesised products. The yield of both synthetic products is more than 90%. By definition, if the yield of a synthesised product reaches 100%, the REE proportions in the bulk product must be identical to the REE proportions in the starting solution. However, the yield of the synthesis of monazite was 93%, and bastnäsite was 97%. Various factors, e.g. measurement errors, the loss of minor amounts of the samples when changing the crucibles, incomplete solution of the REE oxides, and weight loss during the neutralising process by centrifuging, may affect the calculated final yield. However, with these limitations and more than 90% yields, it is safe to assume that fractionation during the synthesis was very limited. Conducting a chemical analysis to determine the concentration of each REE in the synthetic product is needed for the accurate and precise determination of the REE proportions in the product, but this was beyond the scope of the research project, and confirmation of all REEs used for the synthesis inside the final product is satisfactory to conduct current research.

### 4.2. Mineral mixture preparation and ASD measurements

The mineral mixing method involved combined tube and agate mixing methods as described in section 2.2.1, intending to produce an optimal, homogeneous mineral mixture. Glass tubes, which were used, could introduce minor uncertainties in the powder composition due to the interaction between the glass surface and mineral powders during mixing causing some minerals to be preferentially retained in the tubes. Some powder displacement may also occur between glass tubes and agate mortar transfers. Despite these potential sources of error, the total weight loss during mixing is estimated to be less than 0.01%, which is negligible, and it was assumed that it does not affect the composition of the mineral mixture.

The mineral mixtures for this study were prepared to reflect their natural abundance closely. Although natural carbonatites are complex in mineralogy, our study focused primarily on hematite, REE minerals, and other relevant minerals. Other minerals, such as calcite, dolomite, siderite, and barite, were collectively represented by calcite to simplify the representation and enhance understanding. While a comprehensive study of the entire range of the ternary diagram could provide detailed insights into the behaviour of mineral mixtures with hematite (e.g., determining if a polynomial fit is appropriate), this approach was not taken in this study as it would not accurately represent natural conditions. Thus, our focus remained on detecting REEs within these simplified mineral mixtures reflecting their natural abundance.

ASD measurements were conducted in a dark room to prevent light contamination, ensuring that the primary reflections from the samples were due to diffuse reflection. The samples were placed on a flat circular glass plate and gently pressed with another glass plate to flatten them. The samples were rotated

before each measurement to ensure complete coverage of the circular area and to mitigate the effects of fibers being oriented differently within the sample. This method and taking multiple replicates appear effective, as indicated by the minimal standard deviation observed. Ideally, a homogeneous, evenly spread sample should result in no standard deviation in the mean spectra. However, slight variations in reflectance values were observed across six replicates, though these were insignificant (Figure 2.1, Figure 3.4). These variations likely stem from the sample not being uniformly flat throughout the circular area, indicating morphological inconsistencies and incomplete homogeneous mixing. The grain size of the mineral powders was not defined for all the minerals used in the study, which may influence the measurements. The absorption of light by a particle depends on its composition and size. Smaller particles have a higher surface area to volume ratio, leading to increased scattering and reduced absorption, resulting in higher reflectance as more light is scattered back from the material. Later explanation could be a possible reason for the observed very high reflectance of calcite spectra, which in some cases was higher than that of the Spectralon® white standard used.

### 4.3. Spectral data analyses

The spectral feature parameter analysis was conducted using the HypPy software (Bakker, 2022). As described in Section 2.3.2, the software employs a parabolic interpolation of three points around the minimum band to calculate the local minima. This method's advantage lies in its ability to create a spectral subset, allowing for the observation of very small features such as the Nd multiplets at 742 nm. If continuum removal were applied to the entire range, these small features might not be discernible. By specifying a spectral subset, subtle changes in features can be closely observed. This method facilitates feature extraction across all wavelength ranges and was chosen for its consistency. HypPy software also offers an option for broad feature fittings (`(S[700.0:1200.0].nohull()).localminfit(1,broad=True)`), which uses more than three points for parabolic interpolation. This approach is more suitable for broad features, such as those between 700-1200 nm, which were not examined in this study.

The ENVI resampling tool was used for the resampling process. Since ENVI does not have a built-in response function for the sensor considered, except for the WorldView-3 sensor, a Gaussian model was employed. The absence of a specific SRF for each sensor may potentially reduce accuracy, as the SRF is unique to each sensor.

### 4.4. The spectra of synthetic monazite and bastnäsite

The spectral comparison of synthetic monazite vs natural monazite in the ITC mineral collection and published spectra revealed that the absorption features occur at the same wavelength positions (Figure 3.2). However, the gradual drop with decreasing wavelength in reflectance in the VNIR range starting around 1000 nm in natural monazite is not present in synthetic minerals. This gradual drop in natural, brown-coloured monazite may be caused by the presence of Ce<sup>4+</sup> Dijkstra et al., (2024). The synthetic monazite does not include Ce, and the product's colour is off-white instead of brown. Therefore, the gradual drop in reflectance is not observed in the spectra of synthetic monazite. With the absence of this gradual drop in the synthetic minerals, the features due to the trivalent Nd ion at 401, 447 and 472 nm are visible in synthetic material but not in natural monazite. However, the absence of the drop due to Ce<sup>4+</sup> does not have a material effect on the conclusions of the present study of hematite-bearing mineral mixtures, as the Nd<sup>3+</sup> related features at 401, 447 and 472 nm are disappearing nonetheless, even with 1 wt% of hematite. Similarly, in published spectra for natural bastnäsite, a gradual drop in reflectance is observed between 350 and 700 nm

with decreasing wavelengths. Though there is a drop, 447 and 472 nm  $\text{Nd}^{3+}$  features are still visible in the published spectra of natural bastnäsite, while only 401 nm  $\text{Nd}^{3+}$  features are missing (Figure 3.2). When comparing the general albedo of SWIR regions, synthetic monazites exhibit a trend similar to natural monazites.

However, this is not the case with bastnäsite. In synthetic bastnäsite, a gradual decrease in albedo is observed towards the longer wavelengths, starting around 1000 nm. This decline is believed to be caused by the influence of the deep-water Pr,  $\text{H}_2\text{O}$  feature. Additionally, due to the reflectance values being different in the shoulder of the Pr feature in bastnäsite, the continuum-removed features become shallower. The continuum also follows the overall shape of the spectrum (Hecker et al., 2019), and when it is removed, the shoulder at the longer wavelength comes up, making the feature appear less deep (Figure 3.7). However, the Pr features centred around 1472 nm and 1580 nm are broader and exhibit more splitting in the published library spectra, distinguishing them from the synthetic bastnäsite spectra. Further, the absorption feature positions reported in recently published data from Turner et al. (2014 and 2016) overlap with our synthetic minerals' absorption feature wavelength positions (Table 3.1). Therefore, the synthesized REE minerals in the current study effectively represent natural monazite and bastnäsite for reflectance studies, as their feature positions are nearly resembling.

As reported in Table 3.1 and Figure 3.3, synthetic bastnäsite and monazite exhibit few differences in the positions and depths of their REE-related absorption features. In the bastnäsite spectra, the  $\text{Nd}^{3+}$  features at 673, 680, and 942 nm, and the  $\text{Sm}^{3+}$  features at 1079, 1233 nm are shifted 5-20 nm towards longer wavelengths, while the  $\text{Sm}^{3+}$  features at 1105, 1379 nm, completely disappear, compared to the monazite spectra. The Pr- $\text{H}_2\text{O}$  feature observed around 1972 nm in monazite has moved almost 20 nm towards a shorter wavelength in bastnäsite, making a broader and deeper absorption feature around 1946 nm. These differences in absorption features between monazite and bastnäsite are also commonly observed in the published spectral data mentioned in Table 3.1. Therefore, they are likely related to the mineral structure, specifically the ligands, their bonds, and their coordination, and are unlikely to be an indirect effect of the synthesis process. The wavelength position of absorption features depends on the nature of the ligand bonding. A shift towards longer wavelengths, indicating lower energy of the absorption feature, intensifies with increased covalent bonding of the anion ligands and the "cloud expanding" effect (Dijkstra et al., 2024).

The bastnäsite does not exhibit the strong multiplets in absorption features as observed in monazite, although the positions of main  $\text{Nd}^{3+}$  features in the VNIR range (745, 805, 872) overlap in both minerals (Figure 3.3). This absence of clear multiplets is also seen in the  $\text{Pr}^{3+}$  features in the SWIR domain in synthetic bastnäsite, which is present in natural mineral spectra from Kokaly et al. (2017). The influence of ligands and their coordination on the energy levels of the electrons within the shielded 4f subshells of trivalent lanthanides is the cause of the splitting of absorption features into narrow multiplets. These multiplets correspond to the crystal field splitting levels, highlighting the impact of the surrounding environment on the electronic structure of the REE ions (Dijkstra et al., 2024). Although both monazite and bastnäsite have oxygen as the main ligand, the spectra suggest that other ligands (phosphorus in monazite and fluorine in bastnäsite) and/or the coordination of these ligands also influence the splitting and shifting of wavelength positions, as discussed in Dijkstra et al. (2024) and Turner et al. (2016). However, further analysis of the underlying causes is beyond the scope of the current study.



#### 4.4.1. Origin of Pr<sup>3+</sup> feature

Pr (atomic number 59) with electron configuration of [Xe]4f<sup>3</sup> 6s<sup>2</sup> forms Pr<sup>3+</sup> ion, losing the electrons first from the 6s orbital and then from the 4f orbital, turning into the electron configuration of [Xe]4f<sup>2</sup>. Intra configurational excitation of electrons to energy levels within the same 4f subshell probably explains the absorption features in the VNIR and SWIR range (Carnall et al., 1978; Dieke et al., 1968; Dijkstra et al., 2024; Turner et al., 2014, 2016). The two electrons in the 4f subshell can have different spins and be in different orbitals, and these combinations and their coupling create different energy levels. Electrons can be excited from their ground energy state into these higher energy levels by the absorption of a photon with the corresponding energy. For instance, the absorptions caused by the Pr<sup>3+</sup> ion in the SWIR domain result from the elevation from the ground state to the so-called 3F state. In the 3F state, both electrons have the same spin and are in different orbitals, as schematically shown in Figure 4.1. Due to the coupling of spin and orbit, the 3F level is split into three different levels: 3F<sub>2</sub>, 3F<sub>3</sub> and 3F<sub>4</sub>. These correspond to the absorptions seen at ~1950, ~1550 and ~1450 nm, respectively (e.g., Carnall et al., (1978)). These spin-orbit coupling transitions are largely independent of the ligands because they occur relatively deep within the ion in the 4f subshell. However, this is not the case with the crystal field splitting effect. Crystal field splitting occurs due to the interaction of electrons with the ligands and leads to further splitting of the energy levels and, thus, of the absorption features. This effect can be clearly observed in the appearance of multiplets within the main absorption features, indicated with arrows in Figure 4.1.

In bastnäsite, the same broad absorption features due to spin-orbit coupling effects can be seen in the SWIR domain (Figure 3.3). However, in contrast, the multiplets attributed to crystal-field splitting cannot be seen in the bastnäsite as in the monazite. The issue could be due to a greater disorder in the crystal structure of the synthetic bastnäsite, which causes the features to broaden so that the narrow crystal-field-effect multiplets are no longer visible as well (they all merge). However, we did not conduct advanced chemical or crystallographic studies to further investigate the chemical and crystallographic structure of the synthesized minerals, as this is beyond the scope of the current study. These analyses could be considered for future research.

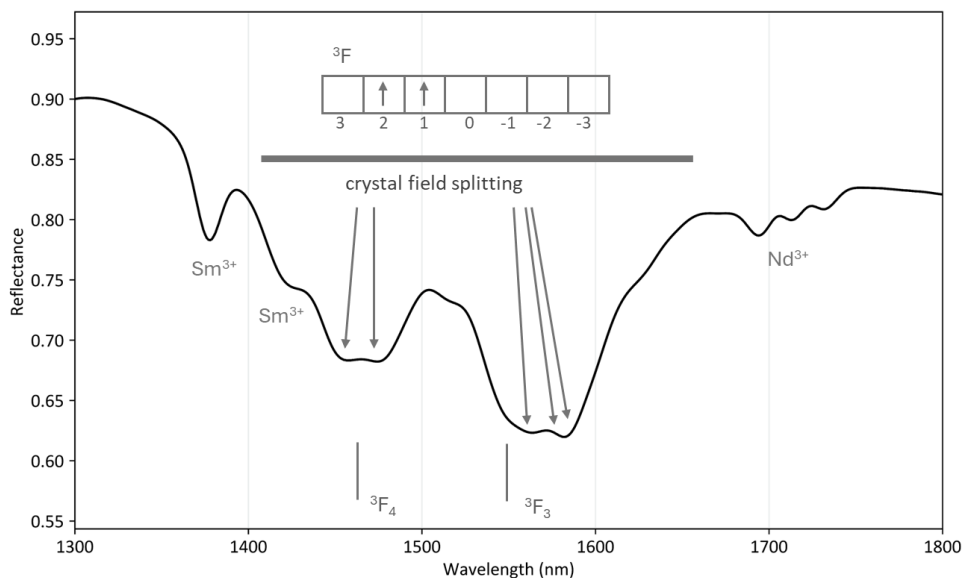


Figure 4.1: Absorption feature of Pr<sup>3+</sup> in synthetic monazite, annotating the spin-orbit coupling levels of 4f<sup>2</sup> electrons in the ion and further splitting of the absorption feature due to crystal field effect. Note that the absorption features at 1370 and 1420 nm are due to Sm<sup>3+</sup>, and the ones near 1700 nm result from Nd<sup>3+</sup>.



## 4.5. Sub objective one - Understanding the behaviour of spectra of the mineral mixtures

This section discusses the behaviour of the high-resolution reflectance spectra observed in powdered mineral mixtures, which reflect the behaviour of light in simple and complex powdered mineral mixtures.

### 4.5.1. Understanding of reflectance spectra of simple mineral mixtures

Understanding the spectral behaviour of simple mineral mixtures containing a REE mineral with either calcite or hematite is a starting point for understanding complex mineral mixtures.

In calcite-monazite mixtures, the absorption feature depth of REE features decreases with increasing calcite abundance, indicating a strong negative (near-) linear correlation between REE ion absorption feature depth and calcite abundance (Figure 3.5). This linear correlation is observed in all absorption features across the range from 350 nm to 2400 nm in the electromagnetic spectrum. The original spectrum of the calcite and monazite do not have high albedo differences, though the reflectance of calcite is comparatively higher than monazite in the whole range, and it does not have any major absorption features until 2300 nm. The high reflective flat spectra dilute comparatively low albedo REE ion absorption features of monazite by decreasing the depth of absorption features in the VNIR and SWIR range (see Figure 3.5), suggesting a linear addition of the individual spectra. Therefore, the spectra of the mixture behave almost linearly, with the addition of calcite only diluting the (monazite) feature depths. Further, the strong carbonate absorption feature at 2334 nm is still clearly visible even with 10% of calcite.

In the case of hematite-monazite simple mixtures, the overall shape of the spectra follows the shape of the hematite spectrum as strong absorption characteristics of hematite dominate the overall spectral signature, causing significant deviations from linear additive behaviour supporting the statement by Mustard & Pieters 1989. The REE ion absorption features of the mixtures behave differently in the VNIR and SWIR regions. In the VNIR range, Nd<sup>3+</sup> absorption features at 401, 472, 524, and 580 nm disappear even in 90% monazite mixtures (Figure 3.5). These features present as very shallow features in the original monazite spectrum can become completely obscured when there is a significant difference in albedo. The strong REE ion absorption features at 742, 805, and 872 nm are still visible in high monazite samples (90 wt%) with reduced depths. The presence of hematite in a mixture results in disproportionately reduced reflectance, making the mixture appear darker and more similar to hematite's spectrum. Therefore, the features in VNIR either disappear or depth is reduced due to the non-linear mixing of the spectra. Similar observations and non-linear behaviour of hematite mixed spectra reported by Mustard and Pieters (1989) support the latter explanation. However, the REE ion-related absorption feature depths in the SWIR range show a moderate positive correlation with increasing monazite.

In the case of hematite and calcite simple mixtures (see Figure 3.5 i,j), the broad absorption feature of hematite around 800 nm does not show a linear relationship with calcite or hematite, whilst, after 50% of hematite, the feature depth does not change. The wavelength position of the absorption feature between 700 and 1200 nm remains stable despite varying modal abundances, with only minor shifts likely due to interpolation errors.

### 4.5.2. Understanding the reflectance spectra of complex mixtures

In high-resolution spectra of complex mixtures, some REE ion absorption features disappear, and some are preserved while the spectra follow the shape of hematite spectra in the VNIR range even with 1% hematite

in the mixture. Even though the Nd<sup>3+</sup> multiplets at 745, 805 and 872 nm are still preserved in hematite mixed spectra, they do not show a linear relationship with the mineral abundance of the mixture. When low albedo hematite is part of a mixture, its strong absorption can dominate the overall spectral signature, making the reflectance spectrum appear darker and more similar to the low albedo mineral. Further, light interacts multiple times within the material, causing light to be absorbed more each time it scatters, leading to an overall lower reflectance. This would be a good example for testing the intimate mixing model, as described by (Hapke, 2012). In the mixtures, low albedo minerals absorb a large fraction of the incident radiation. Continuum removal between 730-760 nm and 760-840 nm highlights these features (see Figure 3.8, Appendix 11). The depth changes of these features are less than 0.1%, making them unsuitable for use as diagnostic features for REE detection in hematite mixed spectra, as the introduction of noise would make identification difficult. Additionally, the relationship between depth changes and mineral abundance is likely polynomial rather than linear, further complicating their use as diagnostic features.

As shown in Figure 3.9, the absorption feature position between 700 and 1200 nm in monazite complex mixtures shifts towards shorter wavelengths with increasing hematite. However, there is no linear correlation between this shift and the percentages of hematite or monazite. This feature movement is associated with the appearance of the Nd<sup>3+</sup> feature at 872 nm in hematite mixed spectra. When the depth of the 872 nm Nd<sup>3+</sup> feature becomes zero due to the mixing of calcite and hematite, the feature is no longer detected, and the general absorption feature position for hematite is observed. This movement in the spectra appears to be a result of interpolation during the feature extraction process. One possible reason for this error could be the broader feature between 700 and 1200 nm. The interpolation method uses only 3 points for the parabolic fitting. When the feature is broader, errors could have occurred.

In mixtures with high monazite content (>15 wt%) and low hematite content, the Nd feature at 872 nm is visible. However, it is important to note that this condition may not accurately represent natural settings, as the general abundance of monazite in carbonatites is typically below 30 wt%.

Overall, it appears that the electronic transition features of Nd<sup>3+</sup> are sufficiently strong to maintain these features in the other minerals' mixed spectra, even when low albedo samples contribute to lower reflectance. High albedo minerals contribute to an increase in reflectance but to a lesser extent than the impact of low albedo minerals like hematite Mustard & Pieters, (1989). Consequently, in a monazite-calcite-hematite mineral mixture, low albedo hematite in the VNIR range significantly affects the overall spectra by reducing reflectance values. In the VNIR range, high albedo hematite and low albedo calcite pull the absorption features towards their respective ends, causing REE absorption features to disappear. It seems that a small amount of monazite does not significantly affect this scenario. Even with 1% hematite in a 10% monazite complex mixture, the REE ion features disappear and the depth changes. In contrast, in the SWIR range, calcite increases the brightness.

#### **4.5.3. Pr<sup>3+</sup> as a promising feature for detecting REEs in hematite mixed spectra.**

The REE features in the SWIR wavelength region are well preserved compared to those in the VNIR. The Pr feature at 1438 nm especially has a detectable depth change (1% reflectance). Because of the linear relationship between the depth of the Pr feature with increasing monazite and decreasing calcite contents, the Pr feature makes a good candidate for detecting REEs in the mixtures. However, this is not the case with bastnäsite mixtures. As shown in Figure 3.7, the Pr feature in bastnäsite mixtures is shallower and broader than the monazite mixtures. As mentioned in section 4.4, the albedo difference between the two shoulders of the Pr feature could be the reason for the shallower depth observed in the bastnäsite mixed

spectra. The addition of highly reflective calcite (reflectance values close to 1) appears to be causing the spectrum to rise and making the feature appear shallower. Due to these changes, using the Pr feature to detect REE features in bastnäsite mixtures in this study is questionable as the feature is shallow and close to the noise levels. The synthesized product may also influence these results, as the gradual drop is not evident in natural spectra. Performing the same analysis with improved synthesized bastnäsite might alter these findings.

The mean reflectance value of a wavelength range is considered when defining the band ratio. The reason for considering a range of wavelength is to reduce the effect of the noise introduced to the spectra. When a mean value of wavelength range is taken, the noise is normalised, and the effect is reduced. The defined ratio “PrR” for Pr detection in monazite mixed spectra shows a strong positive linear correlation with increasing monazite, while it does not correlate with hematite (see Figure 3.10). This proves the applicability of PrR in hematite-rich environments. However, the PrR shows a moderate negative correlation with increasing calcite, which could be a disadvantage in detecting environments with very low monazite and high calcite content.

#### **4.6. Sub objective two: Resampling spectra for hyperspectral sensors**

When laboratory-derived spectra are resampled to match the resolution of hyperspectral airborne and spaceborne sensors, they exhibit the same spectral behaviour as the original laboratory spectra. However, REE ion absorption features in the VNIR region are not visible in the resampled spectra, likely due to the comparatively lower resolution of these sensors (Figure 3.12). This makes detecting REE ion absorption features in the VNIR more challenging than in the SWIR. Despite the low concentration of Pr in the mineral, the Pr feature remains visible in the SWIR, making it a good candidate as a proxy for REE minerals. With the results of the current study, it can be assumed that hyperspectral airborne sensors, such as HyMap and PRISMA, and the higher resolution next mission of the AVIRIS project, AVIRIS NG, may also demonstrate greater capabilities for detecting REE features in the SWIR region. EnMap resampled spectra also exhibit the Pr feature, clearly suggesting that the EnMap is also feasible for detecting the Pr feature as a proxy for other LREEs regardless of the low spatial resolution.

#### **4.7. Sub objective three: Resampling spectra for multi-spectral sensors**

When resampling the hematite-mixed laboratory spectra to Landsat Next sensor specifications, it appears that Landsat Next is unlikely to detect REE features in the VNIR (

*Figure 3.13*). Landsat Next does not have band positions, and the spectral resolution is suitable for detecting REEs in the VNIR range when the spectra are mixed with hematite.

Landsat Next is designed to have several bands in the SWIR region with bandwidths of 20, 30, and 90 nm. The Pr feature centred at 1580 nm is detected by the band centred at 1610 nm, which has a bandwidth of

90 nm. Assuming the spectral resolution function follows a Gaussian distribution centred on the wavelength, with sensitivity highest at the centre and decreasing towards the edges, the Pr features at 1570 and 1580 nm fall within the less sensitive edges of the bandwidth (at 1565 nm). But the right edge exhibits high reflectance. When the whole values are summed to give one reflectance value as output in the centre wavelength, edges are normalized, and the feature at the centre of the bandwidth is not strongly pronounced. Although slight changes in reflectance values between bands 17 and 18 are observed, these changes are also common to hematite and calcite spectra (Figure 3.14). Therefore, it appears that Landsat Next band 18 in the SWIR region also does not effectively detect the Pr feature due to its comparatively wider bandwidth and position of centre wavelength.

Given that Landsat Next sensor specifications include synergies with the Sentinel-2 satellite, it seems Sentinel-2 also lacks the capability to detect the Pr feature in the SWIR range. The SWIR 1 band of the designed Landsat Next sensor, which has a wavelength range of 1565-1655 nm with FWHM of 100 nm, is Sentinel -2 synergy.

Considering the laboratory resampled spectra to the WorldView 3 sensor, it is observed that the SWIR 2 band centring at 1570 nm with the bandwidth of 40 nm at FWHM can detect the Pr feature. Although the feature is shallow, it is still clearly present in the laboratory-resampled spectra. The modified band ratio would probably show a positive correlation with increasing monazite and no correlation with hematite (see Appendix 14, Appendix 15) as it does not show a significant reflectance value difference between SWIR 3 and SWIR 2 in hematite resampled spectra (see Figure 3.14). Nevertheless, in real-world conditions, this may not be the case due to the presence of noise. Even though Worldview 3 appears to be a promising sensor for detecting REEs, a high-resolution band with a bandwidth of less than 20 nm and a centring at 1570 nm would probably improve the detection.

In summary, considering the atmospheric absorption and the bandwidth positions, it seems a future sensor with a band centred at 1570 nm with a bandwidth maximum of 20 nm would improve detecting REEs with multispectral sensors. Further, adjacent bands centred around 1700 nm would probably improve the reflectance level change. However, spatial resolution also plays a role in detecting minerals there, and high spatial resolution would also improve the results.

#### **4.8. Limitations of the study**

This study is based on the simplest mineral combination that represents carbonatites despite the presence of many other minerals in nature. In this study, calcite represents all the other possible minerals, such as dolomite, Fe-Mg-bearing dolomites, and barite. Therefore, the influence of other mineral spectra is not accounted for in the findings of this study. The broad absorption feature from 1000 nm towards 1500 nm due to the presence of Fe<sup>2+</sup> ion in Fe-bearing minerals such as siderite or Fe-Mg bearing dolomites can possibly mask out the Pr absorption feature (Figure 4.2) at 1572, 1580 nm. However, it is important to note that the minerals chosen for this study are the most abundant REE minerals in carbonatites, and the effect of hematite has been a well-noted problem by scientists.

However, this study does not consider spatial resolution, which is a significant factor because high spatial resolution improves the ability to detect subtle mineralogical variations and boundaries between different geological units, which is essential for accurate classification and mapping. Further, higher spatial resolution is crucial when mapping carbonatite dykes as these dykes may not be large enough to be captured by low spatial resolution sensors.

Findings regarding hyperspectral and multispectral sensors are mostly based on 10% monazite complex mineral mixtures. Most high-grade REE deposits contain more than 10% REE oxide (e.g., Mountain Pass). However, these results might not be relevant for low-grade REE deposits where the concentration of REE oxides is below 5 wt%. Nevertheless, even with 5% monazite detection, it depends on the abundance of hematite and calcite.

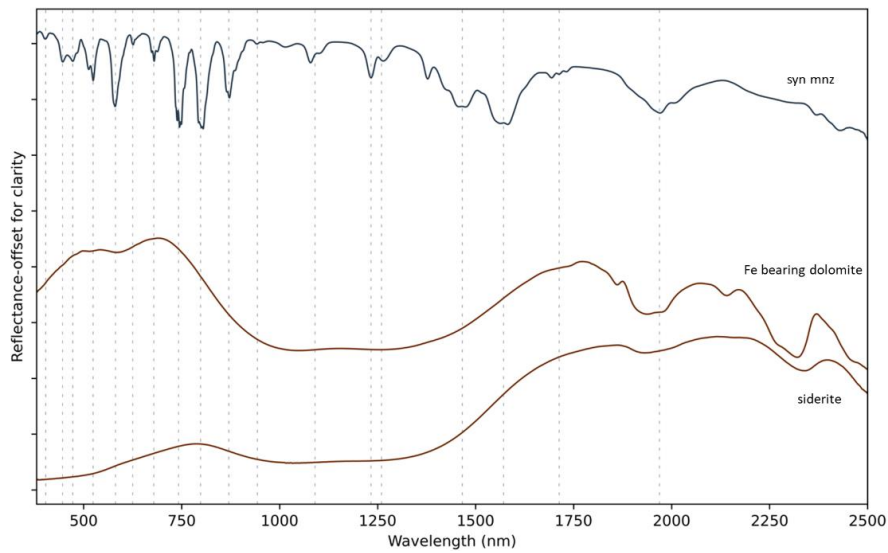


Figure 4.2: Figure showing the reflectance spectra of siderite and Fe-bearing dolomite from (Kokaly et al., 2017) with comparison synthetic monazite, note that broad absorption features of Ferrous ion and the possibility of affecting the broad feature to the REE features in SWIR region.

## 5. CONCLUSIONS

The current study indicates that laboratory-synthesized REE minerals are effective representatives for reflectance spectroscopic studies as they provide fundamental insights into absorption features. Basic mineral mixtures also serve as reliable representatives for studying specific geological environments, making it easier to understand the fundamental theories and processes involved within the simplest models.

This study indicates that due to the high albedo difference between hematite and synthetic monazite, VNIR range absorption features behave non-linearly with mineral abundances, while SWIR region REE absorption features behave linearly. Therefore, the use of absorption features in the SWIR region enhances the detectability of REEs regardless of the hematite percentage. The newly defined PrR using high-resolution spectra for discriminating the Pr<sup>3+</sup> feature can detect REEs in hematite mixed mineral mixtures as the PrR is positively linear with increasing monazite and has no correlation between hematite abundance in the mixtures. The PrR shows potential for use in proximal sensing, although further research, including image analysis, is necessary to confirm its applicability. In monazite, while Nd and Ce are the most abundant REEs, the Pr content is sufficient to create a distinct absorption feature. This suggests that, even if Nd absorption features are not visible in the VNIR range, the Pr feature can be used to detect REEs, serving as a proxy for other light REEs.

The current study suggests that current hyperspectral airborne and spaceborne sensors have the capability of detecting Pr feature centring at 1580 nm. This feature falls within the atmospheric window; therefore, hyperspectral satellites like EnMap would also be able to detect this feature (Figure 3.15).

The laboratory-resampled spectra for multispectral remote sensors reveal the potential of the WorldView 3 sensor in detecting the Pr feature in monazite mixtures. The SWIR 2 band centred at 1570 nm (40 nm bandwidth at FWHM) of WorldView 3 has the capability to detect the feature even though the feature is shallow. However, our results suggest that the planned super spectral mission Landsat Next sensor seems to lack the capability to detect REEs due to the absence of bands with at least 20 nm bandwidth centred around 1570 nm. Even though there are few bands in SWIR, one of them is centred at 1610 nm, and the width of the band is 100 nm at FWHM. Therefore, it alters the Pr feature.

This study does not include Fe-bearing minerals such as siderite, so the findings won't be applicable to environments containing these minerals as the broad absorption feature of Fe<sup>2+</sup> can affect the Pr feature (Figure 4.2). In such cases, it would be better to use carbonate and phosphate features as proxies to identify potential areas for carbonatites. In the case of using proxies for carbonatites, Landsat Next may act as a reliable sensor, as it has TIR bands (ASTER synergies) where it can detect phosphate absorption features. As mentioned by Rowan and Mars 2003, potential geological environments for carbonatites can be identified with broad Fe<sup>3+</sup> feature at VNIR, CO<sub>3</sub><sup>2-</sup> feature at 2334 nm and phosphate features as this combination is unique for carbonatitic environments.

In summary, according to the study of reflectance spectra of synthetic mineral mixtures, Pr can serve as a new proxy for detecting other LREEs in hematite mixed carbonatites, regardless of the disappearance of REE ion absorption features in VNIR due to hematite. Further, this feature can be detected by hyperspectral remote sensors and World View 3 multispectral sensors. A band centring at 1570 nm with a bandwidth of

20 nm at FWHM with adjacent bands around 1700 nm would be the requirement for future sensors to detect the Pr feature.

## 5.1. Recommendations

The synthesis of bastnäsite can potentially be improved through a heating process. It is essential to verify the phase of each rare earth element (REE) within the bastnäsite to confirm the structure of the synthesized material. Also, redoing the research for bastnäsite mixtures after finalising the bastnäsite synthesis would improve the usability of the findings in any hematite mixed carbonatite environments with the presence of the most dominant REE minerals.

The next step of the spectral study would be checking the findings for artificially added noise spectra as a pre-step before applying it to real-world applications. Also, following the previous work, with artificially added noise, finding detection limits for Pr would be possible. Further, validating the findings of this study with natural rock samples using the newly defined band ratio to assess real-world applicability in proximal sensing would be another approach. Further, mapping REEs bearing carbonatites in a known area using recommended sensors would be another step to validate the findings.

Further research on Fe-bearing mineral mixtures is suggested as minerals like siderite Fe-Mg dolomite are also present in natural carbonatites; the effect of those minerals would also alter the results of this study.

Generally, for future studies on remote sensing, based on the suggested bands for future sensors from the current study, additional bands could be explored to assess the potential for detecting REE features. By assigning assumed FWHM values and centre wavelengths to a Gaussian model, the detection capabilities of these features can be evaluated. This approach would provide a comprehensive understanding of how to optimally place bands in future sensor designs.





## LIST OF REFERENCES

---

- Abaka-Wood, G. B., Zanin, M., Addai-Mensah, J., & Skinner, W. (2019). Recovery of rare earth elements minerals from iron oxide–silicate rich tailings – Part 1: Magnetic separation. *Minerals Engineering*, *136*, 50–61. <https://doi.org/10.1016/j.mineng.2019.02.026>
- Anenburg, M., Broom-Fendley, S., & Chen, W. (2021). Formation of Rare Earth Deposits in Carbonatites. *Elements*, *17*(5), 327–332. <https://doi.org/10.2138/GSELEMENTS.17.5.327>
- Bakker, W. H. (2022). *Hyperspectral python (HypPy)*. <http://hyppy.is-great.org/?i=1>
- Balaram, V. (2019). Rare earth elements: A review of applications, occurrence, exploration, analysis, recycling, and environmental impact. *Geoscience Frontiers*, *10*(4), 1285–1303. <https://doi.org/10.1016/j.gsf.2018.12.005>
- Binnemans, K., Jones, P. T., Müller, T., & Yurramendi, L. (2018). Rare Earths and the Balance Problem: How to Deal with Changing Markets? In *Journal of Sustainable Metallurgy* (Vol. 4, Issue 1, pp. 126–146). Springer Science and Business Media Deutschland GmbH. <https://doi.org/10.1007/s40831-018-0162-8>
- Boesche, N. K., Rogass, C., Lubitz, C., Brell, M., Herrmann, S., Mielke, C., Tonn, S., Appelt, O., Altenberger, U., & Kaufmann, H. (2015). Hyperspectral REE (rare earth element) mapping of outcrops—applications for neodymium detection. *Remote Sensing*, *7*(5), 5160–5186. <https://doi.org/10.3390/rs70505160>
- Booyesen, R., Zimmermann, R., Lorenz, S., Gloaguen, R., Nex, P. A. M., Andreani, L., & Möckel, R. (2019). Towards multiscale and multisource remote sensing mineral exploration using RPAS: A case study in the Lofdal Carbonatite-Hosted REE Deposit, Namibia. *Remote Sensing*, *11*(21). <https://doi.org/10.3390/rs11212500>
- Bruker. (2024a). *Diffraction-EVA*. <https://www.bruker.com/en/products-and-solutions/diffractometers-and-x-ray-microscopes/x-ray-diffractometers/diffrac-suite-software/diffrac-eva.html>
- Bruker. (2024b). *Spec Sheet XRD 18 Specimen Holders for X-ray Diffraction*. <https://my.bruker.com/acton/attachment/2655/f-0e60/1/-/-/-/-/>
- Bruker. (2024c). *X-Ray Diffractometer - 2D Phaser*. <https://www.bruker.com/en/products-and-solutions/diffractometers-and-x-ray-microscopes/x-ray-diffractometers/d2-phaser.html>
- Carnall, W. T., Crosswhite, H., & Crosswhite, H. M. (1978). Energy level structure and transition probabilities in the spectra of the trivalent lanthanides in LaF<sub>3</sub> (No. ANL-78-XX-95). . *Argonne National Lab, Argonne, IL (United States)*.
- Castor, S. B. (2008a). Rare earth deposits of North America. *Resource Geology*, *58*(4), 337–347. <https://doi.org/10.1111/j.1751-3928.2008.00068.x>
- Castor, S. B. (2008b). The Mountain Pass rare-earth carbonatite and associated ultrapotassic rocks, California. *Canadian Mineralogist*, *46*(4), 779–806. <https://doi.org/10.3749/canmin.46.4.779>
- Cen, P., Bian, X., Liu, Z., Gu, M., Wu, W., & Li, B. (2021). Extraction of rare earths from bastnaesite concentrates: A critical review and perspective for the future. In *Minerals Engineering* (Vol. 171). Elsevier Ltd. <https://doi.org/10.1016/j.mineng.2021.107081>

- Chabrilat, S., Guanter, L., Kaufmann, H., Foerster, S., Beamish, A., Brosinsky, A., Wulf, H., Asadzadeh, S., Bochow, M., Bohn N., Boesche, N., Bracher, A., Brell, M., Buddenbaum, C. D., Fischer, S., Hank, T., Heiden, U., Heim, B., Heldens, W., ... Segl, K. (2022). *EnMAP Science Plan. EnMAP Technical Report*. <https://doi.org/http://doi.org/10.48440/enmap.2022.001>
- Chen, W., Honghui, H., Bai, T., & Jiang, S. (2017). Geochemistry of monazite within carbonatite related REE deposits. In *Resources* (Vol. 6, Issue 4). MDPI AG. <https://doi.org/10.3390/resources6040051>
- Clark, R. N., King, T. V. V., Klejwa, M., Swayze, G. A., & Vergo, N. (1990). High spectral resolution reflectance spectroscopy of minerals. *Journal of Geophysical Research*, 95(B8). <https://doi.org/10.1029/jb095ib08p12653>
- Clark, R. N., & Roush, T. L. (1984). Reflectance spectroscopy: quantitative analysis techniques for remote sensing applications. *Journal of Geophysical Research*, 89(B7), 6329–6340. <https://doi.org/10.1029/JB089iB07p06329>
- Dieke, G. H., Crosswhite, H., & Crosswhite H. M. (1968). Spectra and energy levels of the rare earth ions in crystals. . *Wiley Interscience, New York*, 193.
- Dijkstra, A. H., Bakker, W. H., Deon, F., Marcatelli, C., Plokker, M. P., & Hintzen, H. T. (2024). Identification of rare earth elements in synthetic and natural monazite and xenotime by visible-to-shortwave infrared reflectance spectroscopy. *Physics and Chemistry of Minerals*, 51(2). <https://doi.org/10.1007/s00269-024-01284-7>
- Gadea, O. C. A., & Khan, S. D. (2023). Detection of Bastnäsite-Rich Veins in Rare Earth Element Ores Through Hyperspectral Imaging. *IEEE Geoscience and Remote Sensing Letters*, 20. <https://doi.org/10.1109/LGRS.2023.3249624>
- Gislev, M., & Grohol, M. (2018). *Report on Critical Raw Materials and the Circular Economy*. <https://doi.org/10.2873/331561>
- Green, R. O., Eastwood, M. L., Sarture, C. M., Chrien, T. G., Aronsson, M., Chippendale, B. J., Faust, J. A., Pavri, B. E., Chovit, C. J., Solis, M., Olah, M. R., & Williams, O. (1998). Imaging Spectroscopy and the Airborne Visible/Infrared Imaging Spectrometer (AVIRIS). *Remote Sensing of Environment*, 65(3), 227–248. <http://makalu.jpl.nasa.gov/AVIRIS.html>
- Hapke, B. (2012). *THEORY OF REFLECTANCE AND EMITTANCE SPECTROSCOPY* (2nd ed.). Cambridge University Press The Edinburgh Building, Cambridge CB2 8RU, UK.
- Harmer, R. E., & Nex, P. A. M. (2016). Rare earth deposits of Africa. *Episodes*, 39(2), 381–406. <https://doi.org/10.18814/epiugs/2016/v39i2/95784>
- Hecker, C., Van Ruitenbeek, F. J. A., Van Der Werff, H. M. A., Bakker, W. H., Hewson, R. D., & Van Der Meer, F. D. (2019). Spectral absorption feature analysis for finding ore: A tutorial on using the method in geological remote sensing. *IEEE Geoscience and Remote Sensing Magazine*, 7(2), 51–71. <https://doi.org/10.1109/MGRS.2019.2899193>
- Jordens, A., Cheng, Y. P., & Waters, K. E. (2013). A review of the beneficiation of rare earth element bearing minerals. In *Minerals Engineering* (Vol. 41, pp. 97–114). Elsevier Ltd. <https://doi.org/10.1016/j.mineng.2012.10.017>

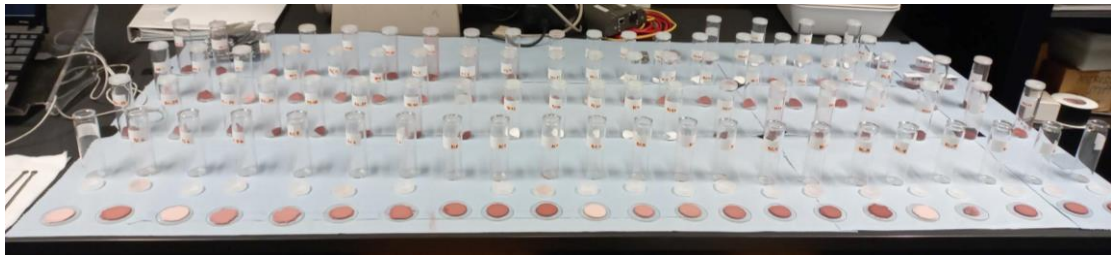
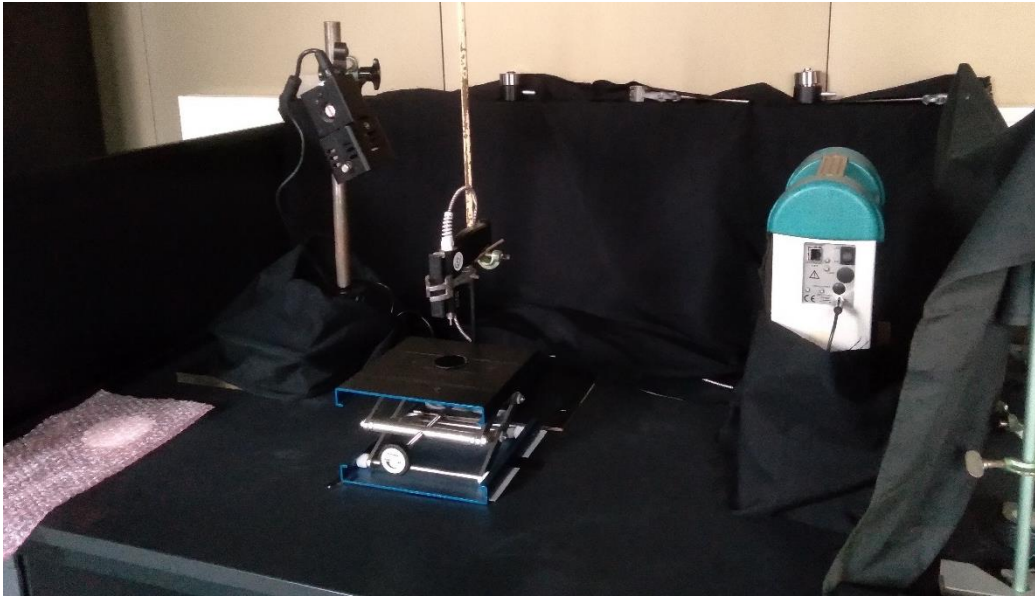
- Kokaly, R. F., Clark, R. N., Swayze, G. A., Livo, K. E., Hoefen, T. M., Pearson, N. C., Wise, R. A., Benzel, W. M., Lowers, H. A., Driscoll, R. L., Klein, A. J., & Kokaly, R. F. (2017). USGS Spectral Library Version 7 (splib07a). *Geological Survey Data Series 1035*, 61. <https://doi.org/https://doi.org/10.3133/ds1035>
- Mustard, J. F., & Pieters, C. M. (1989). Photometric phase functions of common geologic minerals and applications to quantitative analysis of mineral mixture reflectance spectra. *Journal of Geophysical Research*, *94*(B10). <https://doi.org/10.1029/jb094ib10p13619>
- Neave, D. A., Black, M., Riley, T. R., Gibson, S. A., Ferrier, G., Wall, F., & Broom-Fendley, S. (2016). On the Feasibility of Imaging Carbonatite-Hosted Rare Earth Element Deposits Using Remote Sensing\*. *Economic Geology*, *111*, 641–665. <http://econgeol.geoscienceworld.org/>.
- Oliveira, D., & Inverno, C. (2014). Classification of rare earth deposit and occurrence types: what's new? Classificação de depósitos e ocorrências de terras raras: uma nova perspectiva. In *Especial* (Vol. 101). <http://www.lneg.pt/iedt/unidades/16/paginas/26/30/185>
- Percival, J. B., Abraham, A. C., Laudadio, A. B., & Sinclair, C. D. (2019). *The National Mineral Reference Collection (NMC) digital spectral (VIS-NIR-SWIR) library, part II: REE-Nb-U-Th-bearing minerals*. <https://doi.org/10.4095/315690>
- Rowan, L. C., Kingston, M. J., & Crowley, J. K. (1986a). Spectral reflectance of carbonatites and related alkalic igneous rocks: selected samples from four North American localities. *Economic Geology*, *81*(4), 857–871. <http://pubs.er.usgs.gov/publication/70015649>
- Rowan, L. C., Kingston, M. J., & Crowley, J. K. (1986b). Spectral Reflectance of Carbonatites and Related Alkalic Igneous Rocks: Selected Samples from Four North American Localities. In *Economic Geology* (Vol. 81).
- Rowan, L. C., & Mars, J. C. (2003). Lithologic mapping in the Mountain Pass, California area using Advanced Spaceborne Thermal Emission and Reflection Radiometer (ASTER) data. *Remote Sensing of Environment*, *84*, 350–366. [www.elsevier.com/locate/rse](http://www.elsevier.com/locate/rse)
- Simandl, G. J., & Paradis, S. (2018). Carbonatites: related ore deposits, resources, footprint, and exploration methods. In *Applied Earth Science: Transactions of the Institute of Mining and Metallurgy* (Vol. 127, Issue 4, pp. 123–152). Taylor and Francis Ltd. <https://doi.org/10.1080/25726838.2018.1516935>
- Tan, W., Qin, X., Liu, J., Michalski, J., He, H., Yao, Y., Yang, M., Huang, J., Lin, X., Zhang, C., & Liang, X. (2021). Visible/near infrared reflectance (VNIR) spectral features of ion-exchangeable Rare earth elements hosted by clay minerals: Potential use for exploration of regolith-hosted REE deposits. *Applied Clay Science*, *215*. <https://doi.org/10.1016/j.clay.2021.106320>
- Turner, D. J., Rivard, B., & Groat, L. A. (2014). Visible and short-wave infrared reflectance spectroscopy of REE fluorocarbonates. *American Mineralogist*, *99*(7), 1335–1346. <https://doi.org/10.2138/am.2014.4674>
- Turner, D. J., Rivard, B., & Groat, L. A. (2016). Visible and short-wave infrared reflectance spectroscopy of REE phosphate minerals. *American Mineralogist*, *101*(10), 2264–2278. <https://doi.org/10.2138/am-2016-5692>
- U.S. Department of the Interior, & U.S. Geological Survey. (2024). *Landsat Next Satellites offer improved data to Earth science*. <https://doi.org/10.3133/fs20243005>

- Van Ruitenbeek, F. J. A., Bakker, W. H., Van Der Werff, H. M. A., Zegers, T. E., Oosthoek, J. H. P., Omer, Z. A., Marsh, S. H., & Van Der Meer, F. D. (2014). Mapping the wavelength position of deepest absorption features to explore mineral diversity in hyperspectral images. *Planetary and Space Science*, *101*, 108–117. <https://doi.org/10.1016/j.pss.2014.06.009>
- Verplanck, P. L. (2017). The Role of Fluids in the Formation of Rare Earth Element Deposits. *Procedia Earth and Planetary Science*, *17*, 758–761. <https://doi.org/10.1016/j.proeps.2017.01.014>
- White, W. B. (1967). Diffuse-Reflectance Spectra of Rare-Earth Oxides. *Appl. Spectrosc.*, *21*(3), 167–171. <https://opg.optica.org/as/abstract.cfm?URI=as-21-3-167>
- Woolley, A. R., & Kempe, D. R. C. (1989). Carbonatites: Nomenclature, Average Chemical Composition. *In Carbonatites: Genesis and Evolution*, 1–14.
- Yang, Y.-H., Wu, F.-Y., Li, Y., Yang, J.-H., Xie, L.-W., Liu, Y., Zhang, Y.-B., & Huang, C. (2014). In situ U-Pb dating of bastnaesite by LA-ICP-MS. *Journal of Analytical Atomic Spectrometry*, *29*(6), 1017–1023. <https://doi.org/10.1039/c4ja00001c>
- Zimmermann, R., Brandmeier, M., Andreani, L., Mhopjeni, K., & Gloaguen, R. (2016). Remote sensing exploration of Nb-Ta-LREE-enriched carbonatite (Epembe/Namibia). *Remote Sensing*, *8*(8). <https://doi.org/10.3390/rs8080620>

## Appendix

---

Appendix 1: Photograph of the measurement set-up and the samples



Appendix 2: Table showing the description of the spectra used to get the averaged natural monazite spectra from Kokaly et al. (2017)

<b>Kokaly et al. (2017) – USGS v7 – Monazite spectra</b>		
Spectra Name	Sample description	Locality
Monazite HS255.1B_ASDFRbb	Powder	Miguel County, New Mexico-
Monazite HS255.2B_ASDFRbb	Powder	originally in Hunt and Salisbury
Monazite HS255.3B_ASDFRbb	Powder	collection
Monazite HS255.4B_ASDFRbb	Powder	
Monazite_REE_GDS947_Calif_ASDFRbb	Powder	Ione, California
Monazite_REE_GDS957_NewMex_ASDFRbb	Powder	from Petaca district, New Mexico
Monazite_REE_WS385_crystal_ASDFRbb	Crystal	Elk mountain
Monazite_REE_GDS955_Iceland_ASDFRbb	Crystal	Iceland, Setesdal, Norway

Appendix 3: Table showing the description of the spectra used to get the averaged natural monazite spectra from Percival et al. (2019)

<b>Percival et al. (2019) - GSC</b>		
Spectra Name	Sample description	Locality
<b>NMC007965</b>	Massive, coarse-grained, reddish-brown	Villeneuve Twp., Papineau Co., Quebec, Canada
<b>NMC007979</b>	Crystal fragments, reddish-brown	Villeneuve Twp., Papineau Co., Quebec Canada
<b>NMC012239</b>	Crystal, euhedral, prismatic, reddish-brown	Region de Fort Dauphin, Madagascar
<b>NMC012844</b>	Crystals, reddish-brown	Fort Dauphin, Madagascar
<b>NMC018954</b>	Unconsolidated: crystal fragments, brown	Servos Twp., Sudbury Dist., Ontario, Canada
<b>NMC018958</b>	Crystal fragment, brown-red	South Platte, Colorado, USA

Appendix 4: Table showing the description of the spectra used to get the averaged natural bastnäsite spectra from Kokaly et al. (2017)

---

**Kokaly et al. (2017) – USGS v7 – Bastnäsite spectra**

Spectra Name	Sample description	Locality
Monazite_REE_GDS955_Iveland_ASDFRbb	Crystal	Iveland, Setesdal, Norway

Appendix 5: Table showing the description of the spectra used to get the averaged natural bastnäsite spectra from Percival et al. (2019)

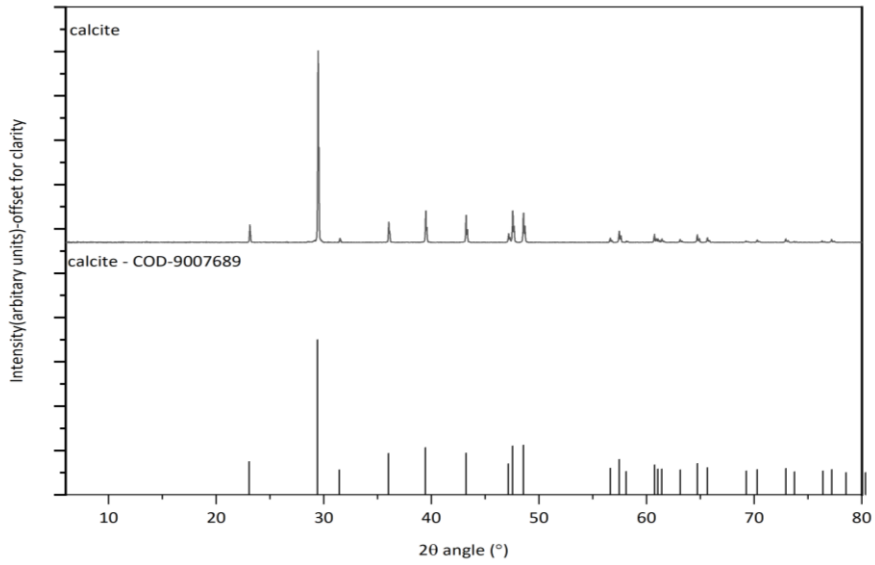
---

**Percival et al. (2019) – GSC – Bastnäsite spectra**

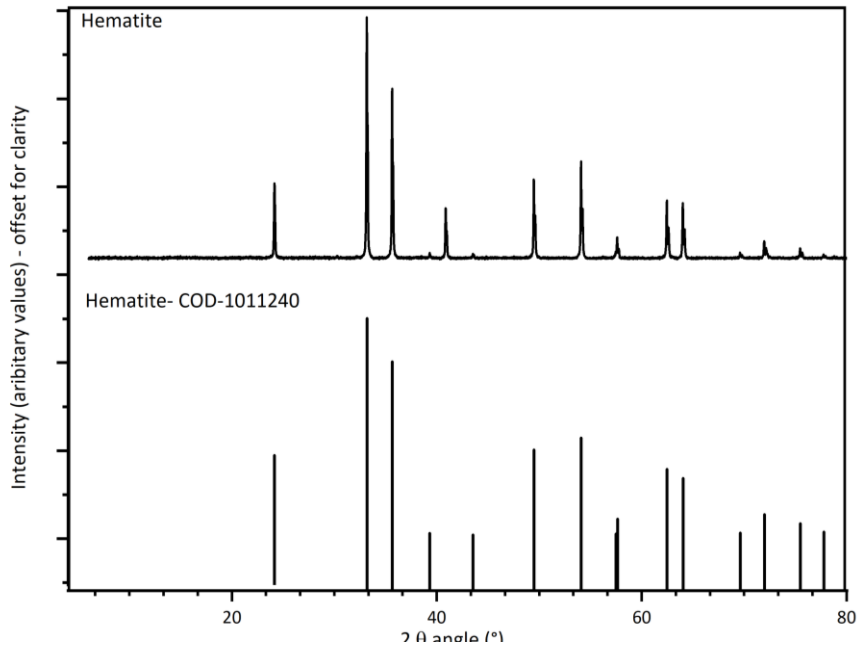
Spectra Name	Sample description	Locality
<b>NMC017454 Bastnäsite</b>	Crystal fragments, tabular, dark reddish-brown	St. Peter's Dome, El Paso Co., Colorado, USA
<b>NMC017455 Bastnäsite</b>	Crystals	St. Peter's Dome, El Paso Co., Colorado, USA
<b>NMC017457 Bastnäsite</b>	Massive, distinct cleavage, wax-yellow, brown	Ambositra, Madagascar (Malagasy Republic)
<b>NMC017458(a) Bastnäsite</b>	Massive, distinct cleavage, wax-yellow	Diandakatany, Madagascar
<b>NMC017458(b) Bastnäsite</b>	Massive, distinct cleavage, wax-yellow,	Diandakatany, Madagascar
<b>NMC065959 Bastnäsite-(Ce)</b>	Unconsolidated: pink powder	Mountain Pass Mine, San Bernardino Co., California, USA

---

Appendix 6: Diffractogram of calcite powder. Note that peaks are overlapping with reference data.

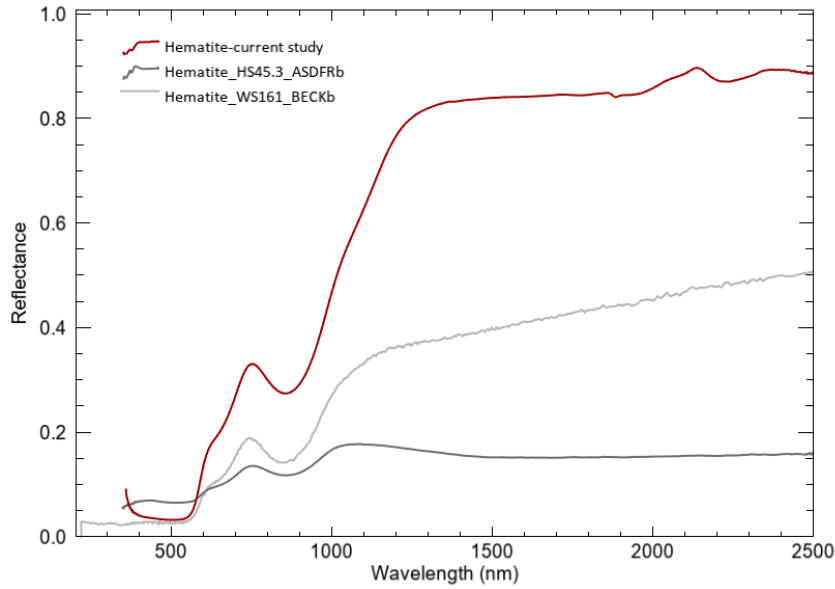


Appendix 7: Diffractogram of hematite powder that has been used in the study

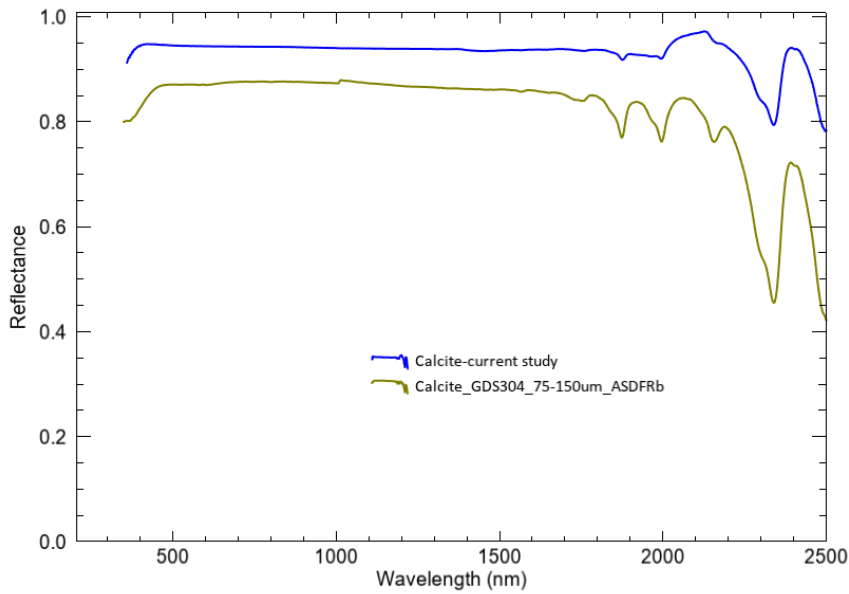




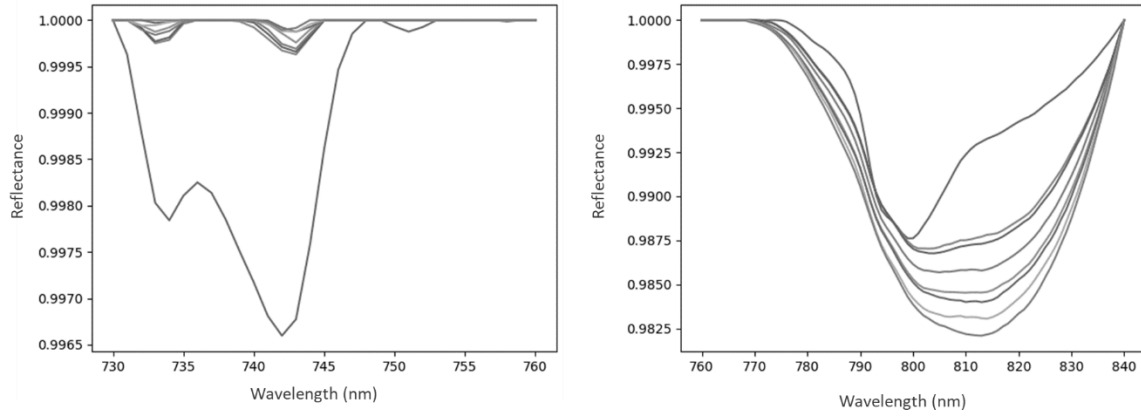
Appendix 8: Comparison of the spectra of calcite that has been used in the current study with hematite spectra of Kokaly et al. (2017)



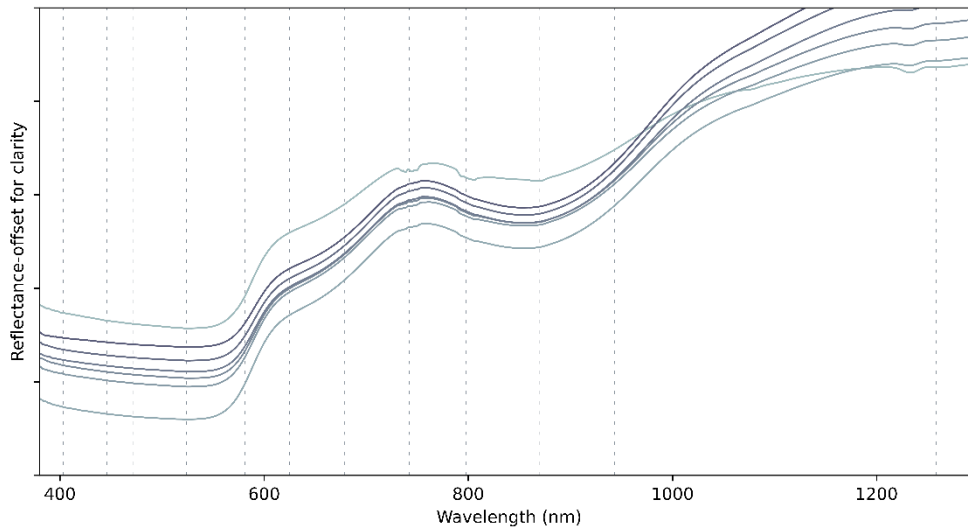
Appendix 9: Comparison of the spectra of calcite that has been used in the current study with hematite spectra of Kokaly et al. (2017)



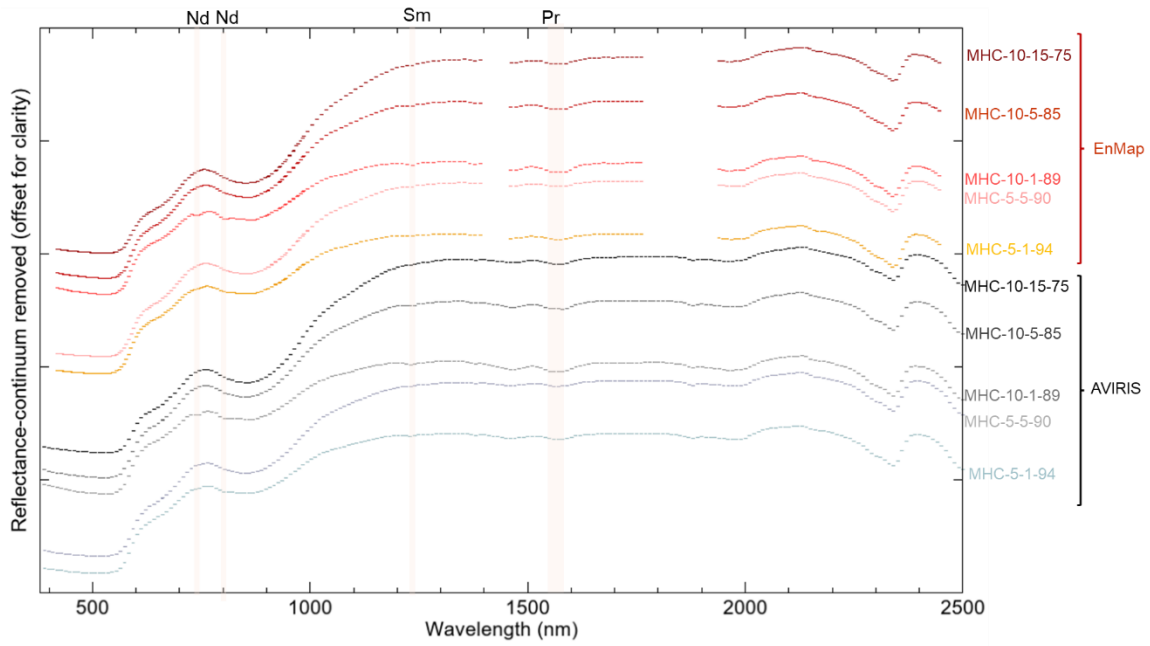
Appendix 10: Nd<sup>3+</sup> multiplet behaviour of bastnäsite 10% complex mixtures; note that the multiplets are not sharp compared to monazite mixtures



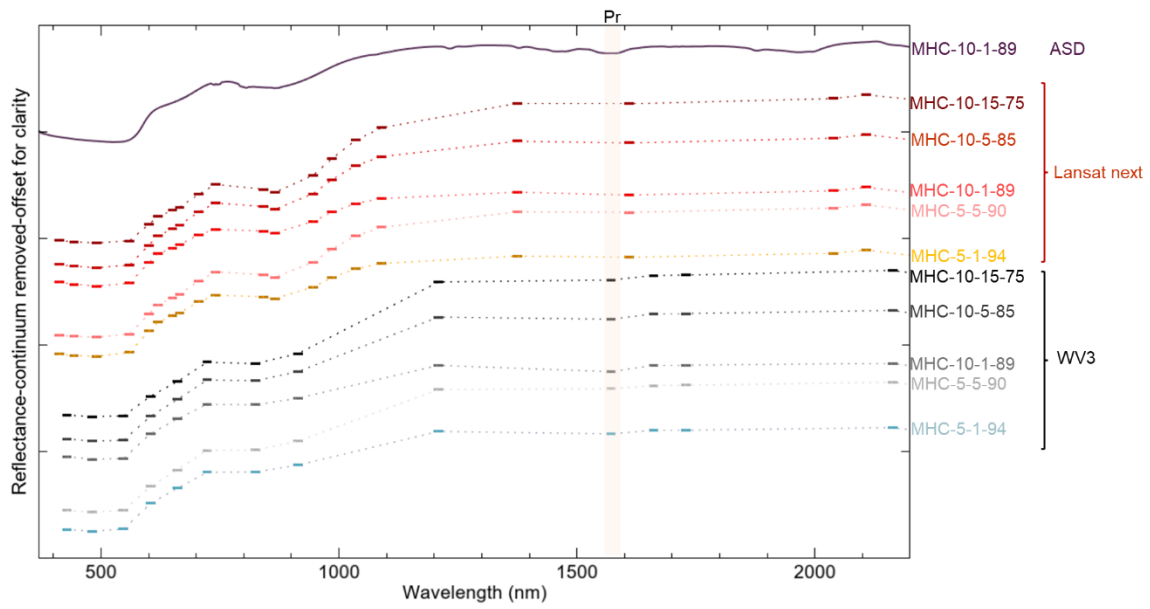
Appendix 11: Behaviour of the spectra of 10% monazite complex mixtures in VNIR range



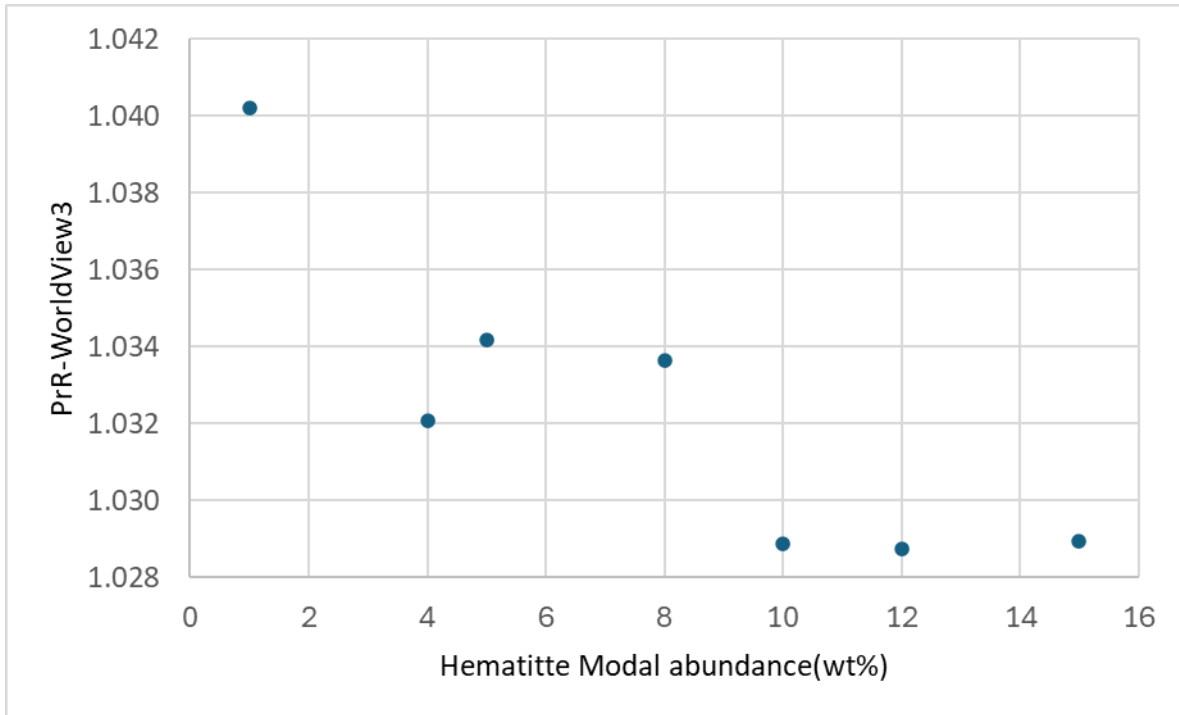
Appendix 12: Laboratory resampled spectra of 10% monazite mixtures for hyperspectral sensors



Appendix 13: Laboratory resampled spectra of 10% monazite mixtures for multispectral sensors



Appendix 14: Scatter plot showing the re-adjusted band ratio vs hematite percentage resampled spectra for WorldView 3 sensor



Appendix 15: Scatter plot showing the re-adjusted band ratio vs hematite percentage resampled spectra for AVIRIS sensor

